Title
Catalytic site requirements for conversion of oxygenates on Zinc-exchanged BEA zeolites

Author
Lin, Eric Tung Hua

Publication Date
2022

Peer reviewed|Thesis/dissertation

UNIVERSITY OF CALIFORNIA

Los Angeles

Catalytic site requirements for conversion of oxygenates on Zinc-exchanged BEA zeolites

A dissertation submitted in partial satisfaction of the

requirements for degree of Doctor of Philosophy

in Chemical Engineering

by

Eric Tung Hua Lin

2022

ABSTRACT OF THE DISSERTATION

Catalytic site requirements for the conversion of oxygenates on Zinc-exchanged BEA zeolites

by

Eric Tung Hua Lin
Doctor of Philosophy in Chemical Engineering
University of California, Los Angeles, 2022
Professor Dante Simonetti, Chair

This work focuses on exploring the site identity of ion exchanged Zn sites in BEA zeolites and their role in the conversion of biomass-derived oxygenates. Careful preparation of ion exchanged Zn in BEA (Zn-BEA) allowed for the generation of different catalytic sites within the pores of the zeolite. Depending on the preparation method, Zn species have been suggested to exist as extra-pore large ZnO clusters, isolated Zn^{2+} ions at the cation-exchange site, $Zn(OH)^{+}$ ions exchanged to one aluminum sites, binuclear $[Zn\text{-}O\text{-}Zn]^{2+}$ clusters formed from the coupling of neighboring $Zn(OH)^{+}$ species, and Zn^{2+} exchanged to two aluminum sites.

In order to probe the oxidation state and local structure of the Zn, *in situ* Zn K-edge x-ray absorption spectroscopy was conducted at SLAC National Accelerator Laboratory. Spectra were taken of Zn-BEA before and after the temperature treatment process. The increase in Zn absorption edge energies in these catalysts compared to Zn standards suggests increased oxidation of Zn sites. The features at the absorption edge change during the temperature treatment, splitting from a single peak into two peaks. The lasting changes at the white line suggests the coordination sphere of Zn sites changes significantly during the activation process.

Analysis of the EXAFS region was conducted to examine the local structure of Zn in the catalysts. Fitting was carried out simultaneously through the samples, effectively constraining fits

with shared parameters to allow for more reliable models. There was a lack of Zn-Zn and Zn-Si contributions in the first and second coordination shell, which indicates that Zn atoms were exchanged into isolated exchange positions without the formation of a significant amount of Zn clusters. *In situ* thermal treatment of Zn-BEA caused the number of oxygen neighbors to decrease in the first coordination shell. This supports the theory that as-prepared samples of Zn-BEA have water coordinated to Zn sites within the pores of the zeolite and the temperature treatment process dehydrates the catalyst. There was a strong correlation between oxygen bond distance and Zn concentration, suggesting that Zn has an increasingly strong interaction with framework oxygen as the degree of ion exchange decreases. Changes in bond distance as more Zn is introduced to the pores can be explained shifts in the preferential ion exchange positions for Zn. As Zn replaces Brønsted acid sites during the ion exchange process, the lowest energy exchange locations may shift between the four-, five-, and six-member rings.

Brønsted and Lewis acid site density was measured by *in situ* titration during acid catalyzed isopropanol dehydration using probe molecules of pyridine and 2,6-di-*tert*-butylpyridine. By measuring the acid site densities, Zn-BEA has been shown to lose Brønsted acid sites during the temperature treatment process. Changes in the calculated Lewis acid site concentrations can suggest the presence of shifts in preferred site structures as Zn concentration increases. The chemical compositions of the catalysts were determined by inductively coupled plasma – optical emission spectrometry. This catalyst characterization was combined with the activity of Zn-BEA for methanol dehydration to determine the reactivity of different Zn sites. The conversion of butyraldehyde over a range of Zn loadings on Zn-BEA was also conducted to probe how the local structure of Zn sites influence the rates and selectivity of the various pathways in reactions of butyraldehyde.

The dissertation of Eric Tung Hua Lin is approved.

Louis Bouchard

Vasilios Manousiouthakis

Philippe Sautet

Dante Simonetti, Committee Chair

University of California, Los Angeles

2022

Table of Contents

List of Figures

List of Tables

ACKNOWLEDGEMENTS

This work was the result of the energy and support of many people without whom none of this would have been possible. To my advisor, Professor Dante Simonetti, thank you for giving me the opportunity to pursue this degree. Your continued support and guidance during my time at UCLA has been critical to my growth as a researcher. You have my gratitude for mentoring me through with all mistakes and missteps that I've made in and out of the lab. To my committee members, Professor Louis Bouchard, Professor Philippe Sautet, and Professor Vasilios Manousiouthakis, thank you for your time and guidance. Your constructive questions and suggestions have been influential in shaping the outcome of this work. Thank you to my fellow group members and collaborators for their assistance and support during this endeavor. I would also like to thank and acknowledge the following individuals who worked with me and contributed directly to this work: Anas Al-Aqeeli, Steven Bustillos, Luke Minardi, Simon Bare, and Adam Hoffman. Lastly, I would like to thank the few undergraduates that I have mentored or worked with: Ksenia Afonicheva, Ionne Arakelyan, and Richa Ghosh for all their hard work. To all my former and current Simonetti group members: Byron, Steven, Anas, Marios, JC, Aziz, Sara, and Faisal, thank you for being there and keeping the office exciting.

Words cannot express my appreciation for my friends and family for their support during this period of time in my life. I would like to thank my parents for their continued support and belief in me. I would not have been able to come as far as I have without them motivating me to work hard. Thank you to my friends: Ana, Jasmine, Daryl, Andrea, Adrian, Roxanne, Abdullah, Edward, Dot, Joseph, Melly, Garry, and Tony for all their support. Lastly, I would like to thank my partner Chris and his family for being so caring and supportive. For anyone who was unnamed, you have my thanks and apologies. This work would not have been possible without any of you.

VITA

2013 – 2017	B.S Chemical Engineering University of California, Riverside Riverside, CA
2017 – 2022	PhD Candidate University of California, Los Angeles Los Angeles, CA
2018 – 2022	Teaching Fellow University of California, Los Angeles Los Angeles, CA

PUBLICATIONS

Eric Lin, Anas Al-Aqeeli, Adam Hoffman, Simon Bare, and Dante Simonetti, *Nature of active sites in Zn-modified H-BEA zeolites and its role in conversion of oxygenates*, In preparation.

Eric Lin*, John Matsubu*, Kyle Gunther, Krassimir Bozhilov, Yibo Jiang, and Phillip Christopher, (2016, April), *Critical role of interfacial effects on the reactivity of semiconductor-cocatalyst junctions for photocatalytic oxygen evolution from water*, Catalysis Science & Technology. *these authors contributed equally to this work

Chapter 1 Introduction

1.1 Motivation

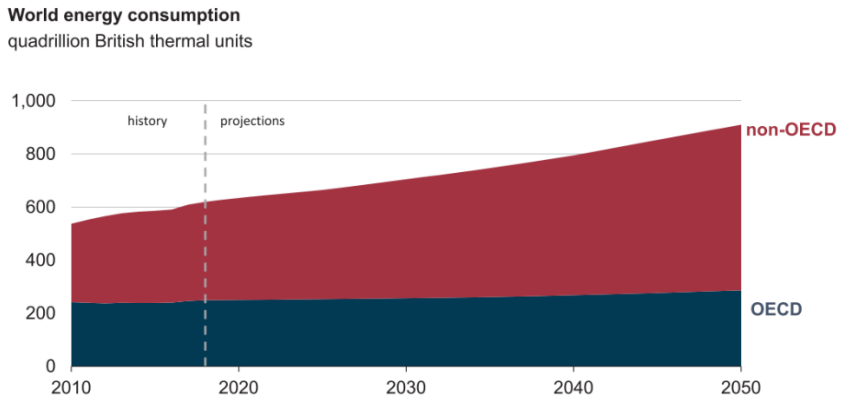

Figure 1. World energy consumption (in quadrillion BTU) from 2010 projected to 2050.[1]

Energy is a vital resource for economic development and human well-being.[2] Reliance on energy has become so pervasive throughout society that modern life would not be possible without easy access to cheap, reliable energy resources. Ever since the Organisation for Economic Co-operation and Development (OECD) formed the International Energy Agency (IEA) in 1977, the IEA has tracked the global production, trade, and consumption of energy. Analysis of this data suggests that energy demand is closely tied to a nation's economic growth when measured by their gross domestic product.[2,3] Increasing productivity in developing economies lifts billions of people from low income to middle class and drives increases in energy demand due to higher living standards. Global energy demand has thus increased year after year with projections of world energy consumption rising nearly 50% between 2018 and 2050.[1] To meet this demand, the rate of fossil fuel consumption will increase and thus, speed up the depletion of fossil fuel reserves.

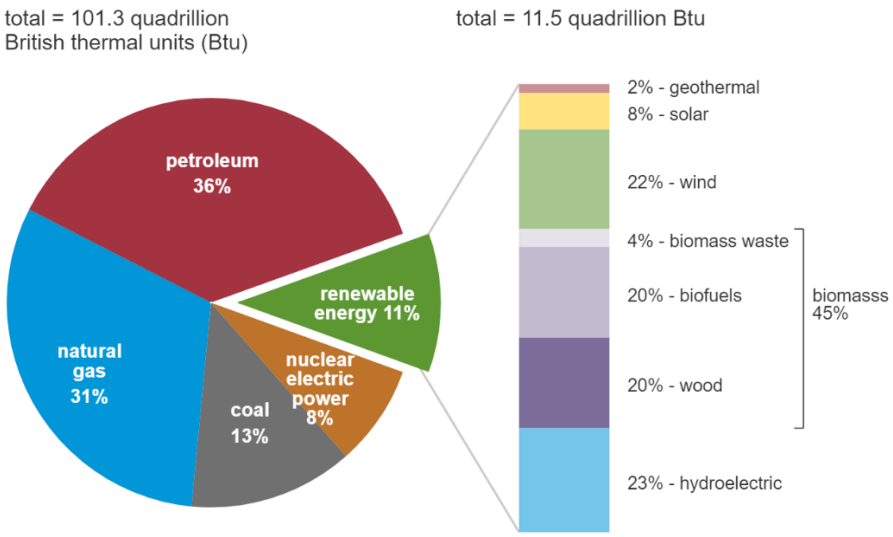

Figure 2. U.S. primary energy consumption sorted by energy source, 2019.[4]

Breaking down the US energy consumption into its various sources shows that petroleum and natural gas makes up 67% of the total, at 68 quadrillion Btu, and provides 97% of the transportation sector's energy consumption.[4] The reliance of society on non-renewable carbon-based energy sources causes the accumulation of carbon dioxide in the atmosphere by pushing the rate of anthropogenic emission above the rate of natural sequestration processes to the tune of nearly 5.5 billion metric tons of CO_2 a year.[5-6] This continued increase in the atmospheric concentration of carbon dioxide is expected to lead to changes in the climate.[7–10] Increasing concern over the environment coupled with current energy security issues drive the need for society to diversify its energy portfolio.[1,11] While it is expected that renewable, non-carbon-based energy sources will play an integral role in future energy infrastructure, the transition to these energy sources will have to occur over several decades. Therefore, it is necessary to develop a multi-pronged approach to supplement current energy technologies. Towards this goal, it is logical to investigate strategies to improve efficiency and sustainability of carbon-based energy technologies.

1.2 Current Hydrocarbon Upgrading Technology

Natural gas and biomass represent attractive options to supplement petroleum as future energy feedstocks for transportation fuels and chemical precursors. However, processes are needed to upgrade natural gas and biomass due to their respective short hydrocarbon chain lengths (C_1-C_5) of alkanes and high oxygen content that limit their use as energy sources. Conversion of natural gas to methanol followed by Brønsted acid-catalyzed C_1-homologation reactions is one of the predominant technologies for natural gas conversion to useful energy resources.[12,13] Similarly, biomass can be upgraded via biological routes to short chain oxygenated intermediates followed by acid-catalyzed C-C bond formation and hydrodeoxygenation reactions.[14,15] These technologies have the disadvantages of producing wide ranges of products over a broad molecular weight distribution as well as requiring external hydrogen sources to strip oxygen atoms from the oxygenates.[16,17] Previous work in concurrent conversion of natural gas with biomass has focused on using activation of C-H bonds in methane to supply the hydrogen needed for deoxygenation from biomass-derived compounds.[18,19] While methane has the highest H-to-C ratio of all hydrocarbons, an argument can be made for utilizing larger hydrocarbons. C-H bonds in methane are much stronger than the C-H, C-C, and C-O bonds found in larger hydrocarbons and biomass-derived molecules. Thus, utilization of methane as a source of hydrogen faces inherent thermodynamic and kinetic limitations. As a result, co-reactants and products of methane upgrading are more selectively converted in reactions with the temperature required to activate C-H bonds in methane.[18] Technologies that can facilitate hydrogen transfer in co-fed reactants need to be better understood and developing fundamental insight into modifying zeolites with metals for acid-catalyzed reactions is key to deploying future gas conversion technologies.

1.3 Acid-catalyzed Carbocation Chemistry

Acids and bases can be broken into three major classifications: Arrhenius, Brønsted-Lowry, and Lewis. The Arrhenius theory of acids and bases is centered around the dissolution of species to form H^+ and OH^+ ions in aqueous solutions. While this theory explains how these compounds react with each other, it fails to explain how non-hydroxide containing species can form basic solutions. To resolve this issue, Brønsted-Lowry definition of acids and bases focuses on the transfer of protons. Brønsted acids are species that are capable of donating protons while Brønsted bases accept protons, opening the possibility of classifying non-aqueous solutions as acids or bases. In the Brønsted-Lowry system, acids and bases reversibly react in pairs to form conjugate acids and bases. The strength of the conjugate acids and bases vary inversely with the strength of the original acids and bases, which is determined by the degree of dissociation in aqueous solutions. An example of a Brønsted-Lowry reaction is the hydrolysis of ammonia where NH_3 acts as the Brønsted base and water acts as the Brønsted acid. The parallel to Brønsted-Lowry acids and bases is the Lewis system. In the Lewis theory of acids and bases, Lewis acids act as electron-pair acceptors while Lewis bases act as electron-pair donors. These reactions occur with one of the atoms in the bond providing both bonding electrons to form coordinate covalent bonds. An example would be a reaction of ammonia and silver ions, where the ammonia acts as a Lewis base and Ag acts as a Lewis acid.

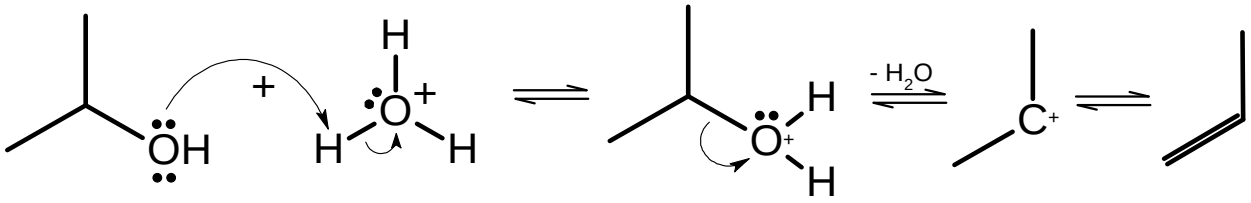

Figure 3. Example of the acid-base proton transfer reaction of an acid catalyzed isopropanol dehydration with a Brønsted acid.

Acid and base catalyzed reactions have similar mechanisms with the participating acid or base catalyst regenerating after the reaction. An example of this can be found in **Figure 3**, a Brønsted acid catalyzed isopropanol dehydration with H_3O^+ shown as a Brønsted acid. The secondary hydroxyl oxygen is protonated to form an alkyloxonium ion which then leaves to form a carbocation intermediate. Finally, the H_2O molecule abstracts a proton from the carbenium ion to form an alkene and regenerates the H_3O.

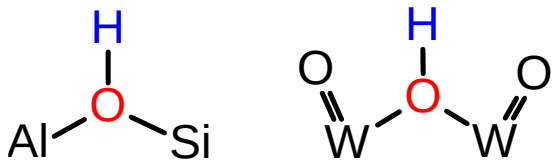

Figure 4. Examples of solid acid framework structures showing the acid and conjugate base on zeolites (left) and POMs (right).

Solid acids typically used in heterogeneous catalysis can consist of transition metal oxides, zeolites, silico-aluminophosphates, polyoxometalates (POMs), and more. While the strength of solvent-based acids can be determined from the acid dissociation constant or the Hammett acidity function gathered experimentally through titration methods, determination of the acidity of solid acids is more complex.[20] Solid acids encompass a variety of sites differing in acid strength and nature.[21] These acid sites thus contribute to solid acid mechanisms differing from the homogeneous solution-phase mechanisms. More importantly, the conditions imposed by the solid acid environment on the reactions also play a role. In the case of zeolites, the catalytic reaction process starts off with the diffusion of reactant through the zeolite micropores to reach an active site. Then, the reactant is adsorbed onto the active site followed by chemical reaction to give the adsorbed product. The product is desorbed and diffused back out the zeolite micropores. A scheme of this mechanism can be found in **Figure 5**. Each of these steps impose effects on the catalytic process as well as provide strategies to control product selectivity.[22] These steps in conjunction with the

steric constraints due to crystal structure cause differences in the stable intermediate products formed during reaction.

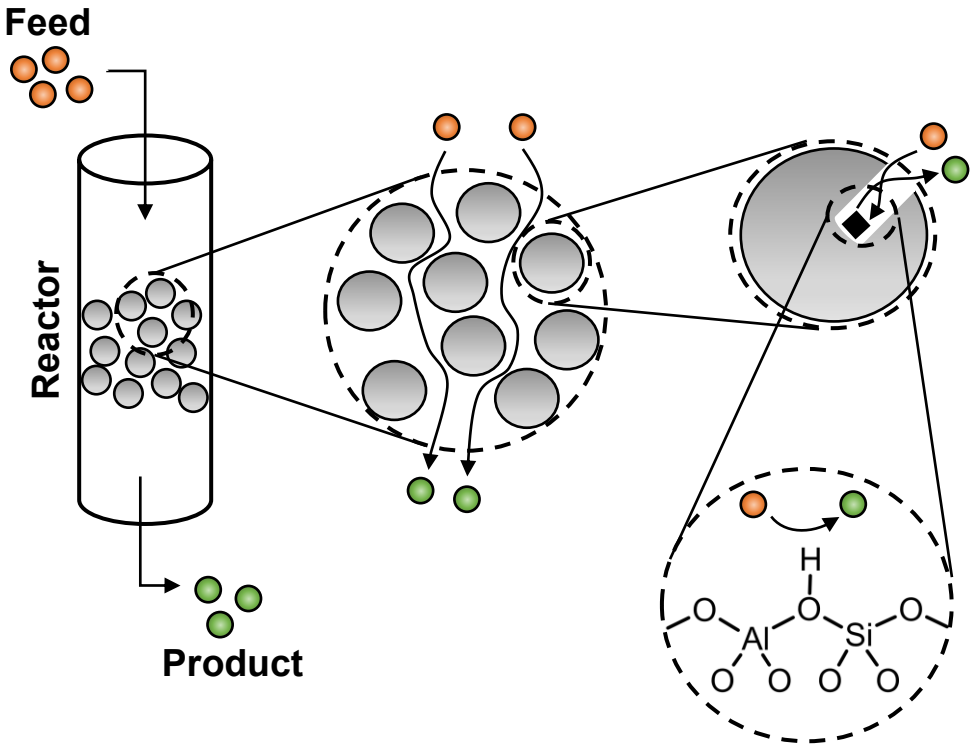

Figure 5. Scheme of reactants diffusing through catalyst layers into the zeolite micropores to an active site. Adsorption onto the active site occurs followed by a reaction to form the product and desorption and diffusion back out the micropore.

Carbocations are common reactive intermediates in organic reactions, identified by their positively charged carbon atom. They can be divided into two main categories based on the valence of the carbon, carbenium ions for trivalent carbons and carbonium for pentavalent carbons. The equilibrium state for a carbocation adsorbed onto liquid superacid is a solvated carbenium ion while the lowest energy equilibrium state when adsorbed onto a solid acid is an alkoxide formed by a covalent bond between the carbocation and the oxygen atom of the acid.[23–25] However, the active species for solid acids remains to be tertiary carbenium ions as examined in dehydrogenation of isobutane on POMs despite its relatively higher energy state.[26] Adsorption of isobutane occurs via the formation of a π-bond between isobutane and surface site followed by donation of a proton

to the secondary carbon of the isobutane adsorbate to produce a carbenium ion. This carbenium ion acts as the transition state between π-bound alkyl and alkoxide states. Studies have shown this to apply to not only alkene adsorption but also isomerization, cracking, oligomerization, dehydrogenation, β-scission, and hydride transfer on zeolites.[26–29] Since the stability of carbenium ions controls the selectivity for these hydrocarbon conversion processes, understanding the mechanisms behind the transition from these adsorbed intermediates to alkoxides is important to designing solid acids to produce targeted species.[30]

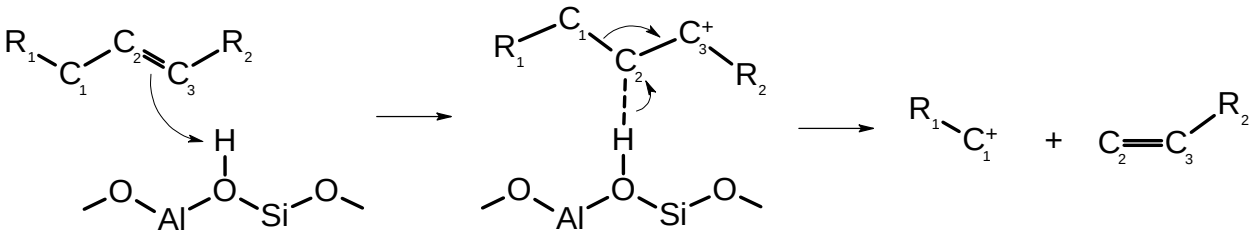

Figure 6. Mechanism of β-scission of an olefin over a solid acid to form an olefin and a carbenium ion.

Hydrocarbon conversion processes over solid acids involve interactions not only with acid sites but also the transition state ions formed during the reactions. Carbenium ion mechanisms of cracking alkanes and alkenes over zeolites have been well researched.[31,32] Olefin cracking over Brønsted acid sites begins with the protonation of the C=C bond to form a trivalent carbenium ion. This ion undergoes subsequent β-scission to form a smaller olefin and carbenium ions. β-scission is the cleavage of the β position C-C bond from the trivalent positively charged carbon atom in the carbenium ion. This mechanism can be seen in **Figure 6**. Paraffin cracking by solid acids can proceed through monomolecular and bimolecular mechanisms. The bimolecular mechanism begins with the formation of a trivalent carbenium ion through a few possibilities: (i) protonation of alkenes present as feed impurities, (ii) formation of alkenes through thermal cracking, (iii) hydride abstraction of the paraffin by a Lewis acid, and (iv) protonation of alkanes by strong

Brønsted acid sites to form pentavalent carbonium ions which collapse to form carbenium ions.[32] This carbenium ion can act as chain carriers that further abstract a hydride from another alkane to form another alkane and carbenium ion. These carbenium ions undergo the same mechanism as mentioned earlier in olefin cracking – the ion undergoes β-scission to form an olefin and a smaller carbenium ion. While this bimolecular cracking mechanism is well studied, the formation of the initial carbenium ion needed for this mechanism can occur through any of the four pathways listed. The last option leads to the monomolecular mechanism which involves the formation of a pentavalent carbonium ion through the protonation of alkane by the acid. This protolytic cracking (Haag-Dessau) has been shown to cause the carbonium ion to collapse to form H_2 and carbenium ions or alkanes and carbenium ions.[33,34]

1.4 Zeolites

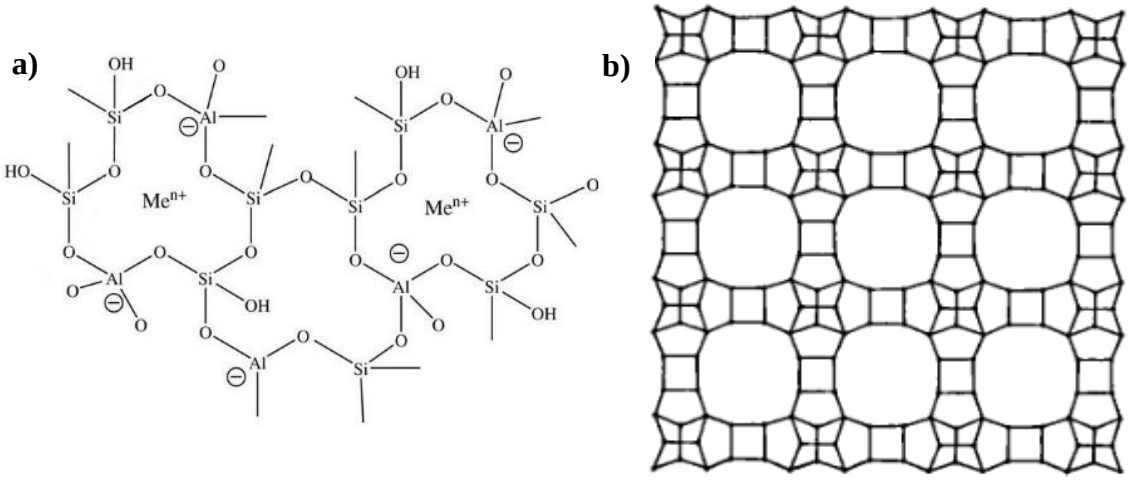

Figure 7. a) A two-dimensional representation of the framework structure of zeolites. Me^{n+} signify extra-framework cations.[35] **b)** Representation of the framework structure of BEA zeolite viewed along [100], showing the formation of pores by the aluminosilicate structure.[36]

Zeolites are both commonly found in nature, typically in cavities of volcanic lava flows, and synthesized in the laboratory with over 245 zeolite frameworks identified.[37,38] Zeolites have shown to be highly versatile materials used for a wide range of industrial processes such as

catalysis, gas separation, and ion exchange.[38] Utilization of zeolites in catalysis has increased dramatically in the past few decades with their use in cracking (fluid catalytic cracking and hydro-cracking), alkylation, isomerization, and hydrocarbon synthesis (methanol-to-hydrocarbons being a noticeable recent commercialized process).[39] Zeolites used in the fluid catalytic cracking process (primarily USY zeolite) constitute more than 95% of zeolite catalyst consumption with over 240 thousand metric tons of zeolites consumed per year.[39]

Advantages of using zeolites lay in their crystalline microporous structure formed by tetrahedral SiO_4 and AlO_4 seen in **Figure 7a**. In catalytic processes, control over the selectivity of products is necessary and can be achieved by limiting the size and shape of the species involved in the process. As seen in **Figure 7b**, this is accomplished in zeolites through the uniform pores formed by the highly ordered aluminosilicate structure - functioning as a molecular sieve that only allow molecules under a certain size to pass.[40] Zeolites are able to discriminate between alkanes with differing carbon number and degrees of branching. It has been shown on BEA that this stems from an increase in enthalpy of adsorption as carbon number increases.[41] This can be explained an increase in dispersion interactions to stabilize adsorbate and the pore walls, causing confinement of the adsorbate in zeolite pores to strongly contribute to the enthalpy of adsorption. These studies on n-alkanes have also been conducted on small alcohols on BEA and MOR, demonstrating that dispersion forces from interactions between adsorbate and zeolite lattice increases linearly with carbon number.[42]

A key characteristic of zeolites is their ability to undergo cation exchange with the acid sites present in the framework.[40,43–45] Substitution of Si^{4+} with Al^{3+} in the zeolite framework creates a net negative charge. A Brønsted acid site (BAS) is formed when the charge balancing of the framework SiO_4^{4-} and AlO_4^{5-} is provided by a proton (H^+), Alternatively, the negative charge can

be balanced by cationic species such as Cu, Zn, Ga, and Co to form Lewis acid sites (LAS). This charge balancing occurs on the framework oxygen, forming bridged hydroxyl groups Si-O(H)-Al in the case of BAS and Si-O(Me^+)-Al for LAS. Extra-framework aluminum (EFAL) can also exist in zeolites as Lewis acid sites.[46,47] Steaming of the zeolite during reactions or as a post-synthesis procedure causes dealumination of the framework by hydrolysis of the Si-O-Al bonds and formation of EFAL.[48] EFAL can be 4- and 6-fold coordinated to oxygen and play a role in stabilizing the lattice by exchanging with the Brønsted acid sites. This causes the steaming process to effectively remove two Brønsted acid sites, one from dealumination and one from the EFAL occupying an ion exchange position.[48] Brønsted acids function as proton donors while Lewis acids function as electron pair acceptors to form coordinate covalent bonds. The acidity of the Brønsted acid hydroxyl group can be attributed to the threefold coordination of the framework O atom and the wider bond angle imposed by the zeolite crystal structure on the Si-O-Al.

1.5 Usage of Metal Species in Zeolite Modification

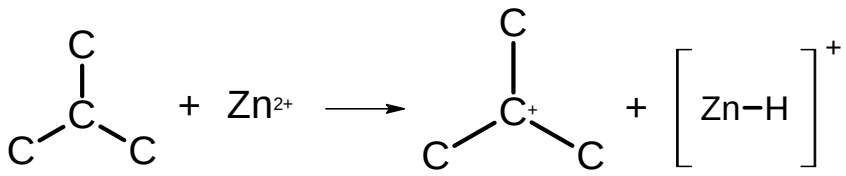

Figure 8. Example of a metal cation acting as a hydride acceptor from alkanes.

Modification of acidic zeolite catalysts with cationic metal species (Ga, Cu, Zn, and Co) has been utilized for activating alkanes for subsequent acid-catalyzed cyclization, isomerization, and desulfurization reactions.[49–57] These metal cations act as Lewis acid sites and the mechanism of activating alkanes has been proposed to be the abstraction of hydride ions from the alkanes by the metal sites to give transient $[M\text{-}H]^+$ species as seen in **Figure 8**.[58] This has been shown in propane dehydrogenation over Ga_2O_3-H-ZSM-5 where the intrinsic activity for propane dehydrogenation was much higher than that of Ga_2O_3.[59] This study established that

dehydrogenation of propane occurs through a bifunctional mechanism with the formation of a gallium alkoxide intermediate that exchanges with a neighboring Brønsted acid proton to form a carbenium ion and molecular hydrogen. This mechanism is assumed to be faster than formation of carbenium ions through hydride abstraction over H-ZSM-5, leading to increases in selectivity for propene upon the addition of Ga. Specifically, the work on Zn metals in zeolites has shown that Zn sites facilitate alkane dehydrogenation to increase hydrodesulfurization rates during thiophene desulfurization reactions.[54,57] In addition, these studies demonstrate that desulfurization-derived species interact with hydrogen-rich intermediates to form aromatic molecules that desorb from the catalysts to prevent the coking of the catalysts. Zn-H-ZSM-5 has been shown to participate in both alkane dehydrogenation and C-C bond cleavage, with studies proposing a mechanism for C-C cleavage similar to that of dehydrogenation and can be found in **Figure 9**.[58]

Doping Zn or Ga onto H-ZSM-5 has shown to enhance the rate of alkane dehydrogenation by 25 to 50-fold.[60] While Zn sites have been shown to perform alkane dehydrogenation in these hydrodesulfurization and dehydrocyclization reactions, they have not yet been studied in conjunction with oxygenate conversion cycles. Thus, investigating if Zn sites can facilitate direct hydrogen transfer from a co-fed alkane to oxygenate intermediates is logical.

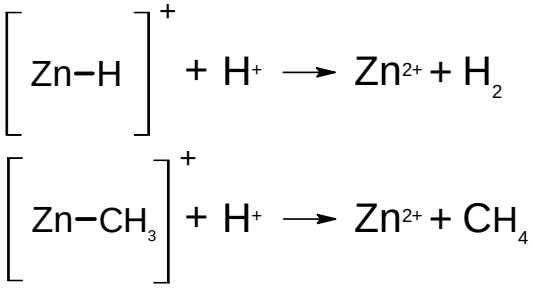

Figure 9. Recombination of metal intermediates with nearby Brønsted acid protons to form molecular hydrogen.

Chapter 2 Experimental Methods

2.1 Catalyst Synthesis

2.1.1 Zn Incipient Wetness Impregnation

Incipient wetness impregnation (IWI), also known as pore volume impregnation or dry impregnation, is one of the most prevalent methods for preparing heterogeneous catalysts. This method is attractive because of its technical simplicity, low costs, and limited amount of waste.[61] Typically, the precursor is dissolved in an aqueous solution and added to the catalyst support. The metal loading of the synthesized catalyst is thus determined by the concentration of precursor ions in solution. IWI relies on capillary action within the catalyst support to drive the transport of precursor solution into the pores and leads to an almost homogenous and complete pore filling.[62] Therefore, it is necessary to quantify the pore volume of the support to prevent the addition of too much solution. This would turn the process from capillary action to diffusion, marking the difference between IWI and the adsorption-controlled wet impregnation methods.

BEA zeolite was chosen based on previous works that studied the effects of pore size on oxygenate and hydrogen transfer reactions.[16,17,63] Zeolite NH_4-BEA (Si/Al 12.5, Zeolyst International, USA) was heated to 773 K (at 0.02 K s^{-1}) for 4 h in flowing dry air to synthesize acid form of zeolite BEA (H-BEA). Zinc impregnated H-BEA (Zn-H-BEA) samples were synthesized through incipient wetness impregnation of H-BEA with an aqueous solution of zinc nitrate (0.69 M). The samples were dried at 373 K for 20 h followed by heating to 773 K (at 0.02 K s^{-1}) for 20 h in flowing dry air. The catalysts were sieved to 60 – 80 US mesh (177 – 250 μm agglomerate diameter).

2.1.2 Zn Ion Exchange

Synthesis of Zn-exchanged BEA will occur through previously established methods of ion-exchange of H-BEA samples in aqueous solutions of zinc acetate to achieve Zn/Al ratios of 0.15. Previous work has shown that this ratio is the maximum at which divalent cations exchange into BEA zeolite while maintaining constant Brønsted acid site density.[30] H-BEA (Si/Al = 12.5) was prepared according to the procedure listed previously and suspended in an aqueous solution of zinc acetate (0.01-0.06 M) and stirred at 353 K for 14 to 69 h. The solid was separated from solution by centrifugation at 3000 rpm for 5 min, discarding the supernatant and re-dispersing the pellet in 20 mL deionized water. This process was repeated until the supernatant was clear, roughly three times. The sample was dried at 313 K for 20 h and temperature treated in flowing dry air. For Zn-BEA samples with Zn/Al ratios less than 0.15, the temperature treatment was RT to 120 °C, 0.5 °C/min; 120 °C, 3h; 120 - 500°C, 1 °C/min; 500 °C, 2 h. For samples with Zn/Al greater than 0.15, the temperature treatment was RT to 500 °C, 5 °C/min; 500 °C, 5 h. For experimental details, see **Table 1** below. The catalysts were sieved to 60 - 80 US mesh (177 – 250 μm agglomerate diameter) to minimize the effects of transport artifacts on reaction kinetics data. Zinc-exchanged zeolite samples are denoted as Zn-BEA. This method has been previously shown to create well-defined Zn^{2+} Lewis acid sites in BEA zeolites.[30,53] From here on out, these catalysts will be referred to as 0.03-0.35Zn-BEA with the number denoting the Zn/Al ratio. Samples subjected to an additional temperature treatment immediately prior to the reaction will be labeled with -pt. This temperature treatment was carried out *in situ* at 723 K, 0.17 K s^{-1}, for 1 h in flowing He (6.2 cm^3 g_{cat}^{-1} s^{-1}).[30]

Table 1. Preparation of ion exchanged Zn-BEA zeolite samples.

$Zn(CH_3CO_2)_2$ (mol L^{-1})	No. of repetitions	Total time of exchange (h)	Treatment method
0.01	1	93	A
0.02	1	14	A
0.03	1	14	A
0.06	1	45	B
0.06	2	69	B

2.1.3 Na-exchanged BEA

Sodium-exchanged BEA zeolite samples were synthesized with the intent to vary Brønsted acid site concentrations to serve as a baseline for acid-catalyzed reaction measurements. Na^+ exchange has already been shown to be an effective means of deactivating Brønsted acid sites for propanal conversion on H-Na-ZSM-5 without the reactivation of Brønsted acid sites by H_2O formed in deoxygenation reactions and without Na^+ catalyzing additional reaction paths.[64]

Proton form BEA (H-BEA) was submitted to ionic exchange in 0.01 – 0.5 M aqueous solutions of NaCl at 323 K under stirring for 2 h.[65] The exchange procedure was repeated up to three times. The solid was separated through centrifugation at 3000 rpm for 5 min and rinsed with a 0.002 M solution of NaOH. The Na-BEA samples were dried at 373 K for 12 h in flowing air. The samples were pressed and sieved to 60 – 80 US mesh (177 – 250 μm agglomerate diameter).

2.2 Catalyst Characterization

2.2.1 X-ray Absorption Spectroscopy

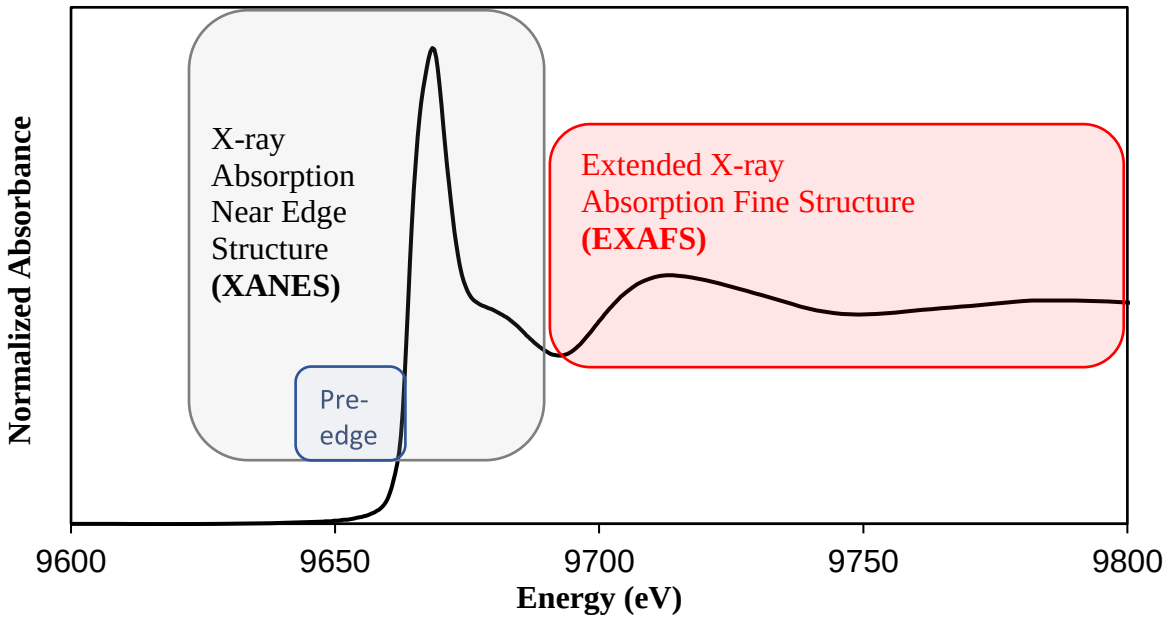

Figure 10. An X-ray absorption spectrum broken up into the XANES and EXAFS regions.

X-ray absorption spectroscopy (XAS) is an investigative technique used to identify atomic local structure as well as electronic states. The core theory behind XAS revolves around the mechanism in which an x-ray is absorbed and a core electron (typically from the 1s or 2p shell) is excited to an unoccupied state or ejected when x-rays are fired at a sample.[66] After the absorption event, the atom is left with an empty core-level electron and the excess energy is ejected as a photoelectron. The energy required to excite core electrons are on the order of thousands of eVs, therefore requiring high energy x-ray excitation at synchrotron facilities. An absorption edge occurs when the energy of the incident photons is just sufficient to excite core electrons and the absorption of incident beam increases dramatically. This makes XAS an element-specific technique as each element and absorption edge requires different amount of excitation energy. The absorption edges are labelled in order of increasing energy: K, L_I, L_{II}, L_{III}, M_I,…, corresponding to the excitation of an electron from the 1s, 2s, 2p, 2p, 3s,…, orbital states, respectively. An XAS

absorption spectrum is typically divided up into three sections that can be seen in **Figure 10**: 1) pre-edge ($E < E_0$); 2) x-ray absorption near edge structure (XANES) ($E < E_0 + 50$ eV); 3) extended x-ray absorption fine structure (EXAFS) ($E_0 > E_0 + 50$ eV). Each of these sections involve different interactions within the atomic structure. The features in the pre-edge region are due to electron transitions from the core level to unfilled or half-filled orbitals. In the XANES region, the higher energy photons push the core electrons past the orbitals into the continuum. The relaxation of these electrons into lower energy states can occur through two processes. The first of which is x-ray fluorescence which occurs when a higher energy electron core-level electron falls into a deeper core hole and ejects a characteristic x-ray. The alternative is the Auger Effect where an electron drops from a higher electron level and a second electron is ejected into the continuum. This allows the absorption coefficient to be measured via transmission geometries versus the fluorescence geometries needed for the x-ray fluorescence effect. At higher energy levels (>2 keV), x-ray fluorescence dominates while Auger Effect occurs more often at lower energy levels.[67]

XANES is a largely qualitative techniques and its analysis provides information about the chemical and electronic structure, primarily the oxidation state of the central atom and bound state transitions through interpretation of edge energies and pre-edge structures.[68] Element- and structure-specific features at the absorption edge act as "fingerprints" for comparisons between samples and reference samples as a first estimate on the local structure of the atom. Least-squares linear combination fitting of spectra from known standards can be carried out to identify the ratio of components within the samples.[69]

For more detailed qualitative and quantitative local structural information, the analysis of the EXAFS space is required. In the EXAFS region, the oscillations within the absorption can be easiest understood by the wave nature of the photoelectron created in the absorption process.

Therefore, EXAFS can be defined as the difference between the measured absorption coefficient and the "background" function as modelled by the absorption coefficient of an isolated atom normalized by the edge step at the adsorption edge (**Equation 1**). This allows for the EXAFS region to be examined in *k*-space, where the x-ray energy is converted into the wave number of the photoelectron. The oscillations are multiplied by a power of *k*, typically k^2 or k^3, to emphasize the oscillations that occur later in the *k*-space.[70]

$$\chi(E) = \frac{\mu(E) - \mu_0(E)}{\Delta\mu_0(E)}$$

Equation 1. EXAFS fine-structure function

The EXAFS region is sensitive to the neighboring atoms due to the constructive and destructive interference between the outgoing photoelectron wave and the backscattered wave from neighboring atoms. [71] Therefore, different frequencies will appear in the oscillations which correspond to the interference from neighboring atoms. Extracting these frequencies from the *k*-space requires modelling of the EXAFS spectra with **Equation 2**, where the sum is taken over the shells of neighboring atoms of type *j* at similar distances from the absorber, N is the number of neighboring atoms, S_0^2 is the *f(k)* is the scattering amplitude, *k* is the wavenumber, σ^2 is the disorder in the distance of the neighboring atom, R is the interatomic distance, and *δ(k)* is the phase-shift of the scattering path. Because *f(k)* and *δ(k)* are dependent on the atomic number of the neighboring atom, EXAFS is also sensitive to the species of the neighboring atom.[70] This function allows for the fitting of the EXAFS curve with known S_0^2, *f(k)*, and *δ(k)* to quantify N, σ^2, and R.[72]

$$\chi(k) = \sum_j N_j \frac{S_0^2}{kR_j^2} f_j(k) e^{-2k^2\sigma_j{}^2} e^{-2\frac{R_j}{\lambda}} \sin\left[2kR_j + \varphi_A(k) + \varphi_{BS}(k)\right]$$

Equation 2. EXAFS equation modelling the photoelectric as a damped spherical wave.[70]

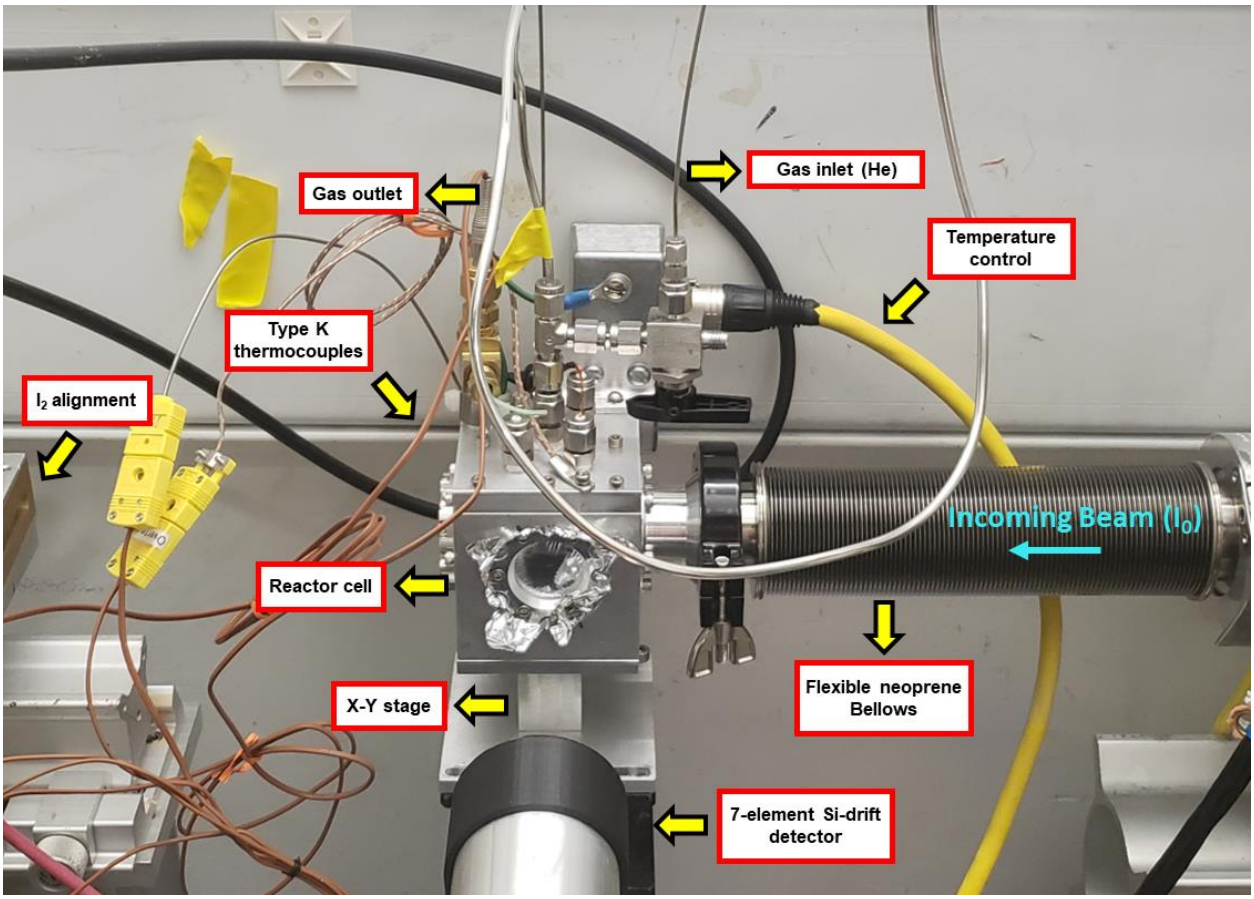

Figure 11. Experimental X-ray absorption spectroscopy setup for the analysis of samples at Beamline 4-3 in SSRL. Image courtesy of Sara Azzam.

X-ray absorption spectroscopy measurements were taken of Zn-BEA on the bending magnet beamline 2-2 and 4-3 at SSRL, SLAC National Accelerator Laboratory to study changes in oxidation states and local environments of zinc cations. The incident beam was selected using a water-cooled double crystal Si(220) phi = 0 monochromator. The ion chambers were filled with N_2 gas. Zn K-edge, 9659 eV, XAS spectra were collected in transmission mode with an energy step of 0.3 eV across the x-ray absorption near edge structure (XANES) and the extended x-ray absorption fine structure (EXAFS) regions with an energy range of 9460 eV – 10633 eV. *In situ* spectra were collected every 92 seconds during the activation of Zn-BEA samples with a zinc foil being scanned simultaneously for energy calibration. Zn-BEA samples were ground into a fine powder and sieved to 177 – 250 µm agglomerate diameter. For *in situ* measurements,

approximately 30 mg of each sample was packed into a 15 cm long 0.2 mm OD borosilicate glass tube and stabilized with quartz wool to prevent sample movement under gas flow. The glass tube was mounted into a flow through capillary cell heated by resistive coils that acts as a plug flow reactor. For *ex-situ* measurements, approximately 30 mg of catalyst were pelletized. Activation occurred in 6.2 cm^3 g_{cat}^{-1} s^{-1} He or H_2 (>99.95, Airgas) ramping from RT to 723 K, 0.17 K s^{-1}, and holding for 1 h before cooling down to 473 K.

Analysis of the XAS data was carried out on ATHENA and ARTEMIS.[73] This software package utilizes FEFF to generate scattering paths from crystallographic information files. FEFF is a set of code that performs *ab initio* self-consistent multiple-scattering calculations to provide scattering phase-shifts and probable single- and multiple-scattering path geometries from atomic coordinates.[74] This allows for the quantification of coordination number, bond distance, and mean-square displacement in bond distance from EXAFS curve fitting.

2.2.2 X-ray Diffraction (XRD)

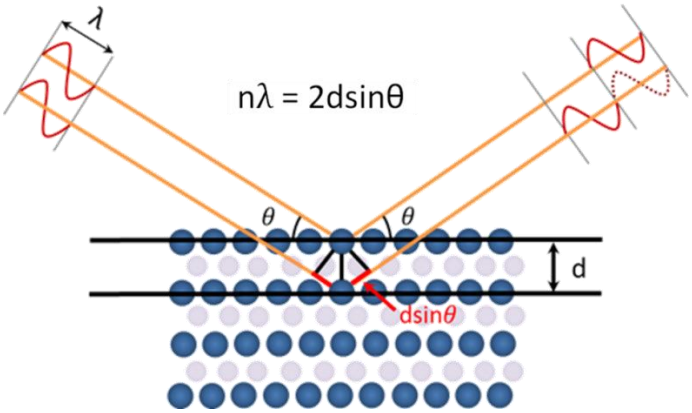

Figure 12. Schematic of the working principle of x-ray diffraction.

XRD is a technique that can be used to characterize the crystallographic nature of a material. **Figure 12** shows a schematic of the working principle of this technique. During XRD, x-rays with wavelengths shorter than the lattice spacing irradiate a sample surface at a sweeping

angle. Constructive interference occurs if the photon path difference is equal to an integral number of wavelengths. Using Bragg's law, the crystal structure and lattice parameter can be determined based on the angle of the detected diffraction peak at the given angle, and the lattice parameters can be extracted. A map of the peaks at all the angles where the constructive interference occurs allows us to uniquely identify the crystal structure of the entire material. Further analysis of XRD diffraction peaks can be done by examining the diffraction peak to obtain the average size of coherently reflecting crystallites in the sample, often termed as the grain size. This is accomplished using the Scherrer equation, which is limited to nano-scale crystallites smaller than 0.1 μm. Crystallinity of the samples can be calculated by deconvoluting the amorphous and crystalline contributions to the diffraction spectrum and taking the ratio of the integrated areas of all crystalline peaks to the total integrated area.

The X-ray diffraction patterns of the catalysts were obtained on a Rigaku Miniflex II diffractometer (Rigaku, Japan) using Cu Kα radiation operated at 30 kV and 15 mA (2Θ = 10 – 80°, step 0.02°, 1 s/step). This data was used to determine the crystallinity and identity of the samples using the Scherrer formula.

2.2.3 Inductively Coupled Plasma Optical Emission Spectroscopy

Inductively coupled plasma optical emission spectroscopy (ICP-OES) is a powerful tool used for the determination of composition of elements in aqueous solutions with detection limits in the upper ppb range. Samples are introduced to the ICP into the plasma, a process which excites the molecules into charged ions. When the excited electrons relax from their higher energy states, photon waves are emitted which possess characteristics of their respective elements are emitted. These photons are quantified by a spectrophotometer and calculated into a concentration using calibration standards.

The catalysts were digested in 1 M HNO_3 and sonicated at 323 K for 4 hours to ensure full digestion of the zeolite. The resulting solutions were analyzed by an Avio 200 (Perkin Elmer, MA, USA). The measured solution concentrations were used to calculate concentrations of Zn, Si, and Al for the zeolites.

2.2.4 N_2 Physisorption

Physical gas adsorption (physisorption) is a technique of importance for the characterization of surface area, pore size, and pore volume of materials. Nitrogen is universally the gas of choice when conducting physisorption experiments.[75] Langmuir's work on monolayer adsorption became the key to interpreting adsorption and desorption isotherms by identifying complete monolayer coverage at the plateau of a Type I isotherm.[76] However, later on it was shown that multilayer adsorption of N_2 was possible at 77 K and empirical evidence indicated the switch to multilayer adsorption occurred at the beginning of the linear section of Type II isotherms. The publication of the Brunauer-Emmet-Teller (BET) theory provided a way to obtain surface areas from these adsorption isotherms.[77] While the BET theory does not properly model highly porous materials, surface areas values of zeolites calculated through this method agree well with the accessible surface areas obtained directly from crystal structures.[78]

While BET theory is used to calculate surface area, physisorption isotherms are used to identify pore size distributions through an application of the Kelvin equation. The method devised by Barret, Joyner, and Halenda (BJH) is the most widely used method to correct for multilayer thickness on the pore walls in the Kelvin equation.[79]

N_2 physisorption measurements were performed on an ASAP 2020 Plus (Micromeritics, USA). Samples were degassed at 423 K for 8 h at a rate of 10 K min^{-1} to desorb gas and water

molecules present on the sample surface. Nitrogen was then adsorbed and desorbed from the surface at 77 K. The adsorption and desorption isotherms were used to calculate surface areas, pore volume, and pore diameter using the BET and BJH methods.

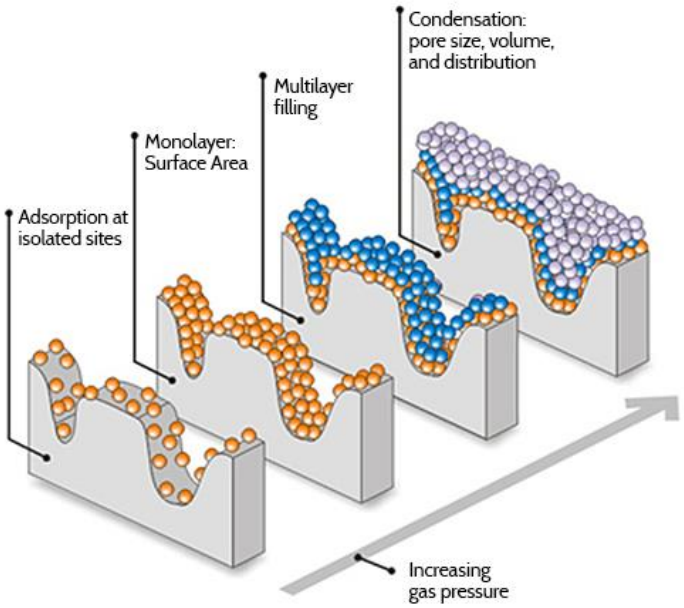

Figure 13. Diagram showing the steps of gas adsorption process. Initially, the isolated sites on the sample surface begin to adsorb gas molecules at low pressure. As the pressure increases, coverage of gas molecules increases to form a monolayer and then the multilayer followed by complete coverage of the sample and pore filling.[80]

2.2.5 Quantification of Acid Sites

Identification and quantification of catalytic active sites is necessary to compare catalytic rates between samples and experimentally determine acid site concentration. Multiple experimental techniques to identify and count BAS and LAS in solid acid catalysts have been described in literature in the last fifty years.[81] Infrared spectroscopy was first to characterize solid state bond frequencies found in zeolites.[82] Fourier transform infrared spectroscopy (FTIR) of pyridine adsorbed on solid acid catalysts allows for the counting of acid sites through quantification of pyridinium ions however has the drawback of requiring accurate molar extinction coefficients, which are highly variable.[83,84] Temperature programmed desorption (TPD) of probe molecules (typically ammonia) can also be an effective and accurate method of characterizing acid sites. An ammonia TPD profile consists of two convoluted peaks and the higher temperature peak is assumed to be the adsorbed stronger acid site (Brønsted acid sites). However, ammonia has been shown to adsorb strongly onto many oxides and causes non-catalytic sites to be counted.[85] This non-specific binding causes ammonia TPD to be an unreliable method for quantifying acid site concentration because it is challenging to conclusively assign the entire adsorption peak to only Brønsted acidity. In this case, *in situ* titration of sites during acid catalyzed isopropanol dehydration was conducted to determine acid site concentrations.

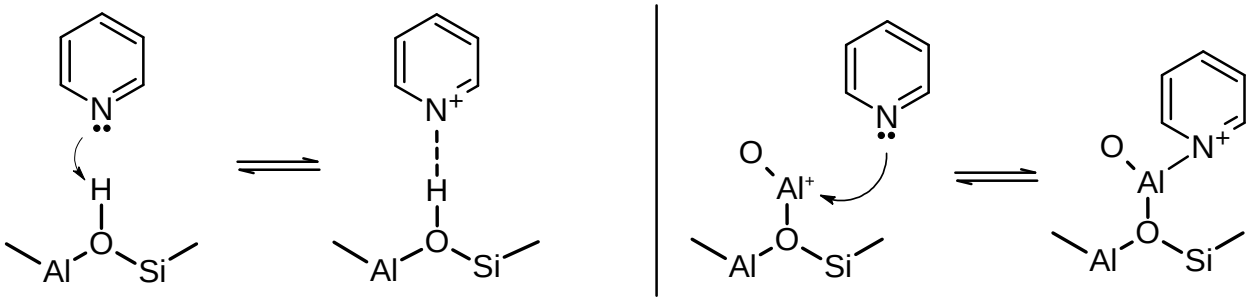

Figure 14. Chemisorption of pyridine onto a Brønsted acid site (left) and Lewis acid site (right).

Pyridine was chosen as a probe molecule because it has been shown to adsorb onto both Brønsted acid sites and Lewis acid sites in stoichiometric manner. Adsorption can be broken up into physisorption and chemisorption. Physisorption is a phenomenon that occurs through van der Waals interaction between the adsorbate to the substrate. As van der Waals forces can exist between any two molecules, physisorption is considered a non-specific process. In comparison, chemisorption is adsorption that involves chemical bond formation between the adsorbate and the adsorbant and has a high specificity. Unlike physisorption, the electronic structure of the molecules participating in chemisorption is changed. Pyridine titrates acid sites through chemisorption of the molecule to the active site. This occurs through hydrogen bonding of the N atom to Brønsted acid sites and through coordinate covalent bonding of the N atom to Lewis acid sites as seen in **Figure 14**. 2,6-di-*tert*-butylpyridine (hindered pyridine) selectively and stoichiometrically titrates only Brønsted acid sites and cannot coordinate to Lewis acid sites due to their steric hinderance.[86] The nitrogen atom in hindered pyridine is so well shielded by the neighboring butyl groups that it cannot participate in the same hydrogen bonding process as pyridine. As a result, hindered pyridine must undergo long-distance proton transfer between the Brønsted acid site and the N atom.[87] These titrated acid sites are then unavailable for isopropanol dehydration.

The number of active acid sites was quantified during isopropanol dehydration catalysis by *in situ* titration with pyridine (99.8%, Sigma Aldrich) and 2,6-di-*tert*-butylpyridine (≥97%, Sigma Aldrich). Quantification of Brønsted and Lewis acid site concentrations was carried out in the same reactor system as the reaction kinetic studies. Steady state measurements of isopropanol dehydration of zeolite catalysts were performed in the reactor heated at 473 K (at 0.16 K s^{-1}). The titrant was introduced by a mixture of titrant and isopropanol (molar ratio of 250:1 isopropanol to titrant). Titrant mixture was fed into the vaporization zone heated at 403 K with flowing He (UHP

>99.999%, Praxair) to give a stream containing 11.4 kPa isopropanol and 45.6 Pa titrant. This concentration of titrant is at a low enough regime to prevent adsorption to the pore walls.[85] Cumulative titrant uptake was calculated from the difference in titrant concentration in feed and effluent vapor stream as measured by online gas chromatography. The titration is considered complete after an hour of steady-state isopropanol concentration in the effluent stream. Cumulative pyridine and 2,6-di-*tert*-butylpyridine uptake were used to experimentally quantify total acid site concentration and Brønsted acid site concentration, respectively. Lewis acid site concentration was determined by performing a site balance using the measured total and Brønsted acid site concentrations.

2.3 Reaction Kinetic Studies

Reaction kinetic studies over the Zn-incorporated zeolites were conducted in a stainless-steel tubular reactor with a 6.4 mm (0.25 in) outer diameter. A bed of fresh powder catalyst (50-100 mg) was loaded in the center of the reactor between plugs of quartz wool with minimal pressure drop across the bed. The reactor was heated in a furnace consisting of a ceramic shell heater with Nichrome in a stainless-steel shell (Applied Test Systems series 3210). The temperature of the reactor was measured with a K-type thermocouple (Omega) attached externally to the reactor and controlled by an EZ-ZONE PM Express PID temperature controller (Watlow, USA). Flow rates of H_2, He, methane, and isobutane were introduced to the reactor *via* GE50A mass-flow controllers (MKS Instruments, USA). Liquid feed (butyraldehyde, ethanol, methanol, or isopropanol) was introduced to the gaseous reactant stream by introducing liquid through a 1 mL gas-tight syringe (SGE 1MDF-LL-GT) controlled with a NE-1000 syringe pump (New Era Pump Systems, USA) into a vaporization zone heated to 10 °C above the normal boiling point of the reactant. The orientation of the three-way valve is used to send gases to the bypass line or

through the reactor to ensure the reactant stream reaches steady-state before introduction to the reactor. Catalyst samples were heated to reaction temperatures (at 0.15 K s^{-1}) in helium prior the start of the reaction. Reactor effluent lines were heated to 180 °C to ensure all species remained in the vapor phase. Reactant and product stream compositions were measured using online gas chromatography/mass spectrometry (GC/MS) with an 5977A GC/MS (Agilent Technologies, USA) equipped with a flame ionization detector (FID) and a HP-5 column (Agilent Technologies, USA). Samples were taken via automatic injection at a split ratio of 50:1 and the inlet temperature was set to 250 °C with a typical initial oven temperature of 50 °C heating to 200 °C at 40 °C min^{-1}. A process flow diagram of the reactor setup can be found in **Figure 15**.

The effect of transport phenomena on the measured catalytic activity of the catalysts was determined through applying the Madon-Boudart criterion to an exothermic reaction of methanol dehydration.[88] To eliminate the possibility of transport limitations on the catalyst pellet, the Madon-Boudart criterion states that the activity of the catalyst is required to be proportional to the number of active sites. This can be accomplished by measuring the rate of reaction as a function of the number of active sites for a series of BEA zeolites with different acid site densities. Sodium was ion exchanged with Brønsted acid sites on H-BEA to prepare catalyst samples with varying acid site concentrations.

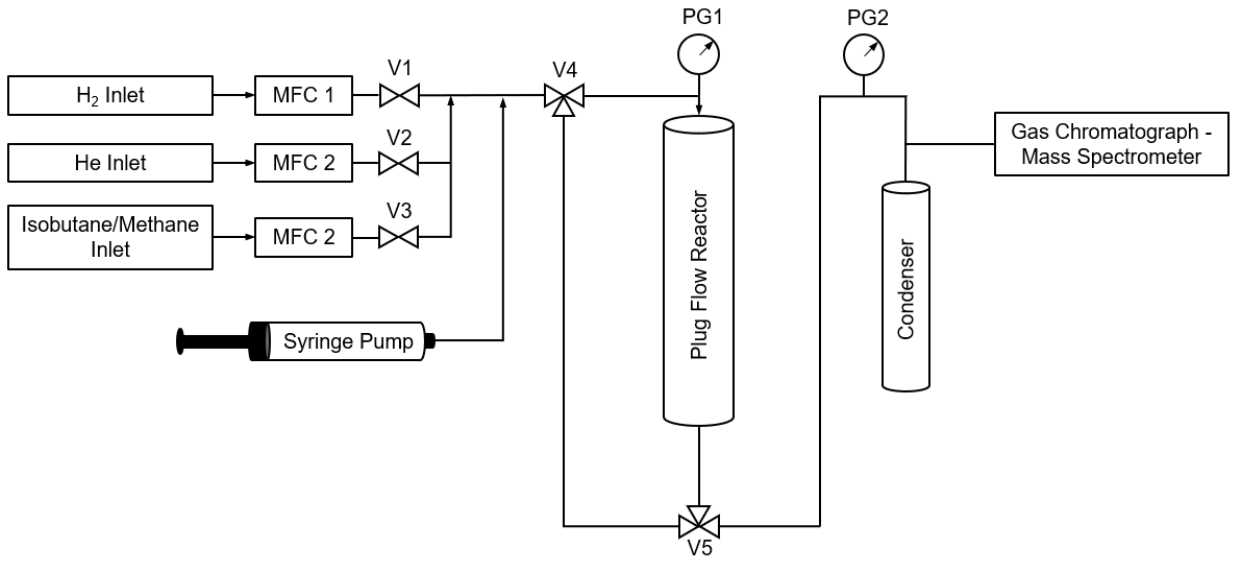

Figure 15. Process flow diagram of laboratory plug flow reactor for reaction and titration experiments.

Chapter 3 Characterization of Metal Species and Acid Sites in Metal-exchanged BEA

3.1 Quantification of Acid Sites

Preliminary studies probed the role of Zn content and synthesis techniques on acid site concentrations in catalytic samples. It is critical to be able to accurately quantify the Brønsted and Lewis acid site concentrations within the catalyst samples to properly evaluate catalytic activity in terms of turnover rates per acid site. These studies used pyridine and hindered pyridine as titrants for acid sites found in Zn-BEA samples synthesized through ion exchange and incipient wetness impregnation at various Zn loadings. Zn-modified zeolites are known to be effective catalysts for promoting dehydrogenation and aromatization of light alkanes and thus have been chosen to be exchanged with BEA zeolite.[89–91] Brønsted acid sites are exchanged for Zn Lewis acid sites through ion exchange and thus identifying the role of these three groups of acid sites present in the Zn-BEA catalysts on acid catalyzed reactions is paramount.

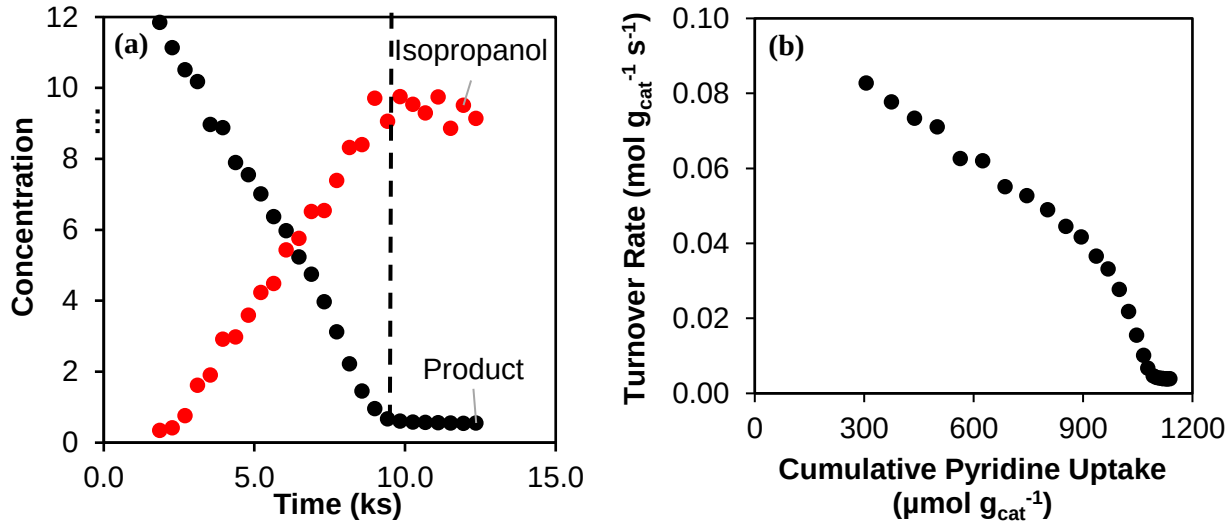

Figure 16. (a) Example of acid site titration process showing the steady decrease in product (di-isopropyl ether and propene) concentration and increase in reactant (isopropanol) concentration as the probe molecule, pyridine, adsorbs to the acid sites on the zeolite catalysts. The dashed line indicates when all accessible acid sites have been titrated. **(b)** Turnover rate of isopropanol dehydration on H-BEA as a function of cumulative pyridine uptake.

As shown in **Figure 16a**, the measured concentration of product and turnover rate in a typical acid site titration process drops off and indicates when all accessible acid sites have been titrated. **Figure 16b** shows measured isopropanol dehydration turnover rates per gram catalyst on H-BEA as a function of cumulative pyridine uptake. The value of cumulative pyridine uptake was used to calculate site concentration with the assumption of stoichiometric adsorbance onto acid sites. The residual turnover rate catalyzed by inaccessible acid sites was accounted for by extrapolation of the titration curve in **Figure 16b** to zero rates. Quantification of acid site concentrations in H-BEA zeolite are consistent with previous literature values (811 μmol Brønsted acid sites g^{-1}, < 0.4% difference).[92] The remainder of the figures used to calculate acid site concentrations can be found in the **Appendix** (**Figure 38** - **Figure 48**) and the experimental values are shown in **Table 2**. Zn/Al ratios and Zn concentrations were obtained through ICP-OES. Samples marked -pt (ex. 0.03Zn-BEA-pt) were treated *in situ* at 723 K, 0.17 K s^{-1}, for 1 h in flowing He (6.2 cm^3 g_{cat}^{-1} s^{-1}), a process described as activating or pre-treating the catalyst [30].

The thermal treatment (activation) process in flowing He for Zn-BEA reduced the number of available Brønsted acid sites across all loadings of Zn. Meanwhile, the Lewis acid site concentration has no readily apparent trend as Zn/Al increases. During the decomposition of 2-propylamine, it has been reported that two different Zn^{2+} ion exchange sites are present in Zn-BEA with one peak increasing linearly from 0 – 0.15 Zn/Al and the other peak increasing markedly between 0.15 – 0.26 Zn/Al. The first peak can be associated with Zn^{2+} incorporated on vicinal aluminum and the second peak is bridged Zn-O-Zn sites.[30] A detailed explanation of the possible Zn sites found in ion-exchanged Zn zeolites can be found in the following section.

Catalyst	Zn/Al	Total Acid Sites (µmol/g)	Bronsted Acid Sites (µmol/g)	Lewis Acid Sites (µmol/g)
H-BEA	0.00	1.10E+03	8.14E+02	2.86E+02
Na-BEA-1	0.00	2.37E+02	1.50E+02	8.70E+01
Na-BEA-2	0.00	1.27E+02	3.56E+01	9.14E+01
Na-BEA-3	0.00	9.85E+02	7.69E+02	2.16E+02
Na-BEA-4	0.00	3.58E+02	2.50E+02	1.08E+02
0.03Zn-BEA	0.03	6.92E+02	6.28E+02	6.40E+01
0.03Zn-BEA-pt	0.03	6.31E+02	5.74E+02	5.70E+01
0.04Zn-BEA	0.04	7.13E+02	6.19E+02	9.40E+01
0.04Zn-BEA-pt	0.04	6.50E+02	5.48E+02	1.02E+02
0.08Zn-BEA	0.08	9.10E+02	6.78E+02	2.32E+02
0.08Zn-BEA-pt	0.08	7.55E+02	5.47E+02	2.08E+02
0.19Zn-BEA	0.19	4.50E+02	3.00E+02	1.50E+02
0.19Zn-BEA-pt	0.19	4.07E+02	2.45E+02	1.62E+02
0.35Zn-BEA	0.35	4.23E+02	3.40E+02	8.30E+01
0.35Zn-BEA-pt	0.35	3.10E+02	2.28E+02	8.20E+01

Table 2. Tabulated experimental values for total, Brønsted, and Lewis acid site concentrations for the catalyst samples.

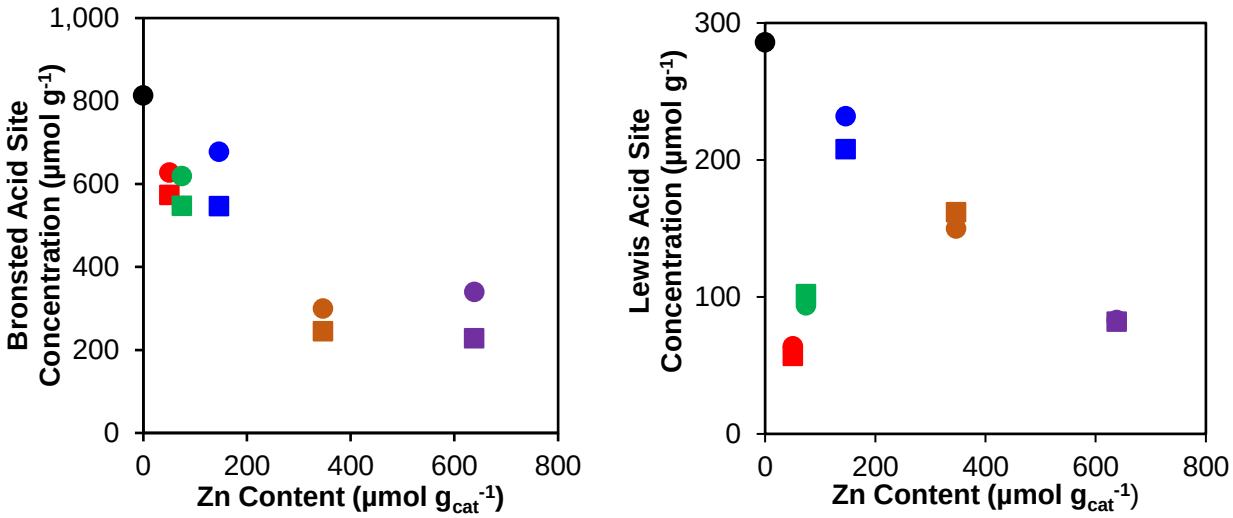

Figure 17. Brønsted (left) and Lewis (right) acid site concentration of H-BEA (●), 0.03Zn-BEA (●), 0.03Zn-BEA-pt (■), 0.04Zn-BEA (●), 0.04Zn-BEA-pt (■), 0.08Zn-BEA (●), 0.08Zn-BEA-pt (■), 0.19Zn-BEA (●), 0.19Zn-BEA-pt (■), 0.35Zn-BEA (●) , and 0.35Zn-BEA-pt (■) as a function of Zn content.

When looking at Brønsted acid site concentrations as a function of Zn content (**Figure 17**), there is a decrease in site density as Zn content increases. This occurs because the ion exchanged Zn replaces the Brønsted acid sites in BEA as the exchange occurs. In each instance, temperature treatment of the catalysts showed a drop in Brønsted acid site concentration which suggests a change in the local structure of the Zn site. Changes in calculated Lewis acid site concentrations as Zn content increases can be supported by the presence of different local site structures depending on the Zn concentration within the catalyst samples. There is a sharp drop in Lewis acid sites when carrying out the ion exchange process, suggesting that the extra-framework aluminum sites found in H-BEA are either removed or become inaccessible to probe molecules. From 0.03 – 0.08 Zn/Al, the Lewis site density increases linearly, indicating generation of accessible Zn^{2+} sites within the pores of the zeolite. Once past this threshold, 0.19Zn-BEA and 0.35Zn-BEA both have lower calculated Lewis acid site concentrations. This suggests that sites formed after a certain threshold of Zn/Al concentrations are unable to be titrated by the probe molecules. Pre-treatment

of the catalysts showed very little changes in the calculated Lewis acid site concentrations. Overall, this forms a volcano plot of Lewis acid site concentrations as a function of Zn concentration.

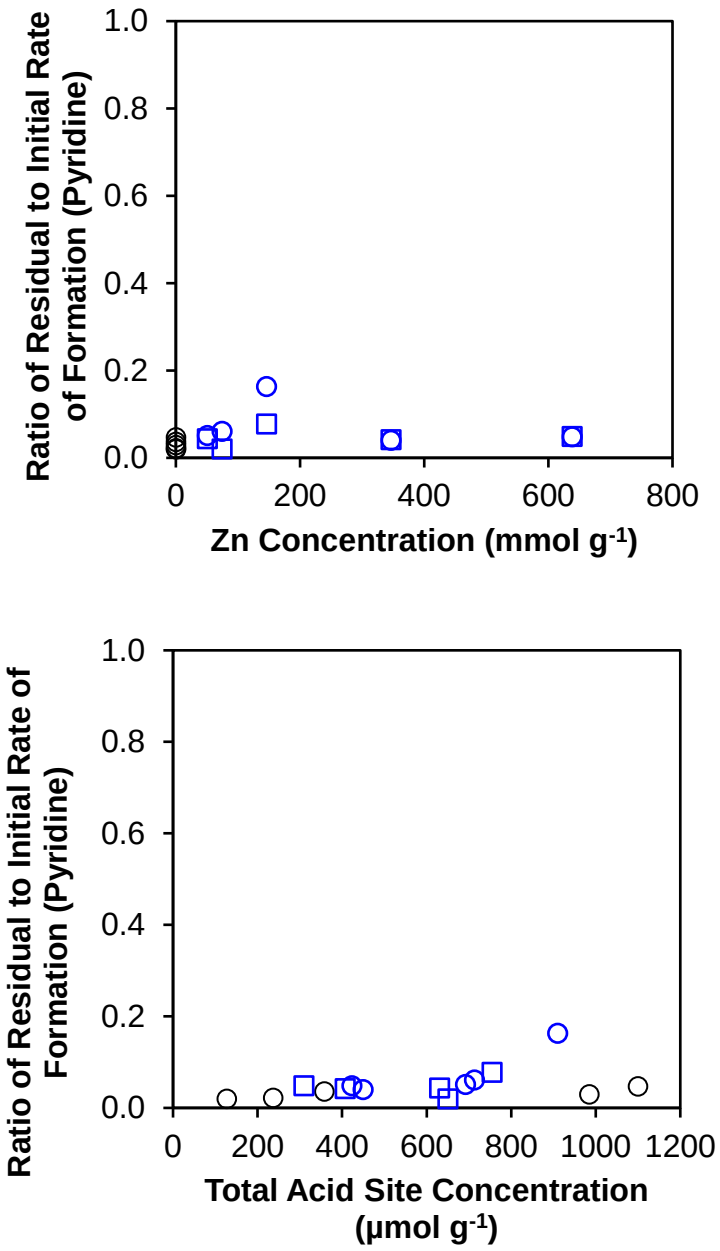

Figure 18. Ratio of residual to initial turnover rates for isopropanol dehydration during pyridine titration as a function of Zn concentration (top) and total acid site concentration (bottom) over Na-H-BEA and H-BEA catalysts (black circles), Zn-BEA (blue circles), and Zn-BEA-pt (blue squares).

The residual rates of product formation for isopropanol dehydration carried out concurrently with the acid site titration process allows us to determine the extent of titration over these catalysts. When taking a look at **Figure 18**, the ratio of the residual rate to initial rate for the Zn exchanged catalysts were mostly in line with the residuals rates of H-BEA and Na-H-BEA samples. 0.08Zn-BEA was shown to have the highest turnover rate after titration, suggesting that there are inaccessible acid sites that are catalyzing isopropanol dehydration or the Zn sites formed at 0.08 Zn/Al are unable to be fully titrated by pyridine. Residual rates for H-BEA after saturation with pyridine were significantly smaller than initial rates (factor of 20) but remain high for saturation with 2,6-di-*tert*-butylpyridine (factor of 5). As increasing amounts of Zn are exchanged with the Brønsted acid sites on H-BEA, the ratio of residual to initial turnover rates during 2,6-di-*tert*-butylpyridine titration (titrating only Brønsted acid sites) increase concomitantly up to 0.08 Zn/Al. An increase in residual rates was anticipated for the 2,6-di-*tert*-butylpyridine titration as Lewis acid sites (both inherent LAS from extra-framework Al and Zn sites) remain available to catalyze the isopropanol dehydration reaction. With this information, there is confidence that the acid site titration process was carried out smoothly with the majority of Bronsted and Lewis acid sites being accurately counted.

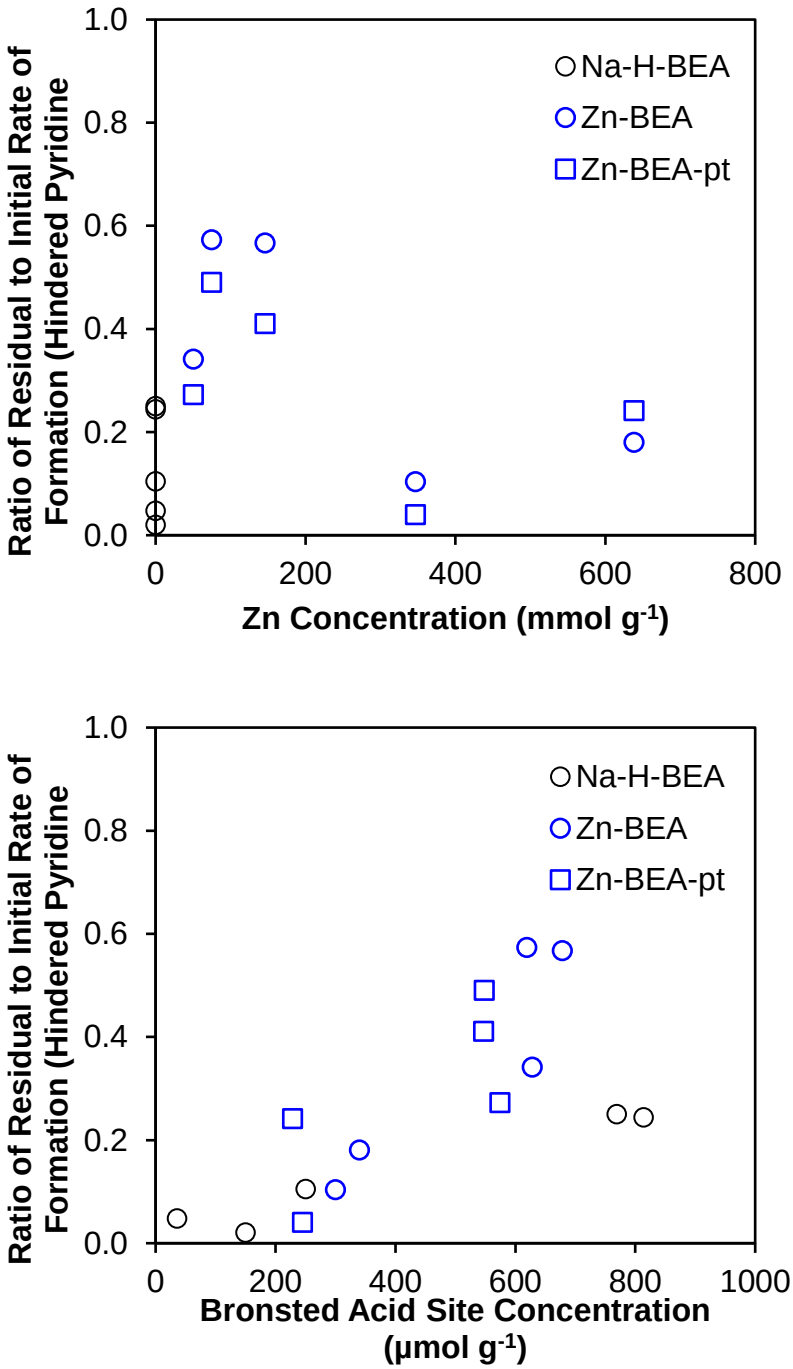

Figure 19. Ratio of residual to initial turnover rates for isopropanol dehydration during pyridine titration as a function of Zn concentration (top) and total acid site concentration (bottom) over Na-H-BEA and H-BEA catalysts (black circles), Zn-BEA (blue circles), and Zn-BEA-pt (blue squares).

3.2 Powder X-ray Diffraction

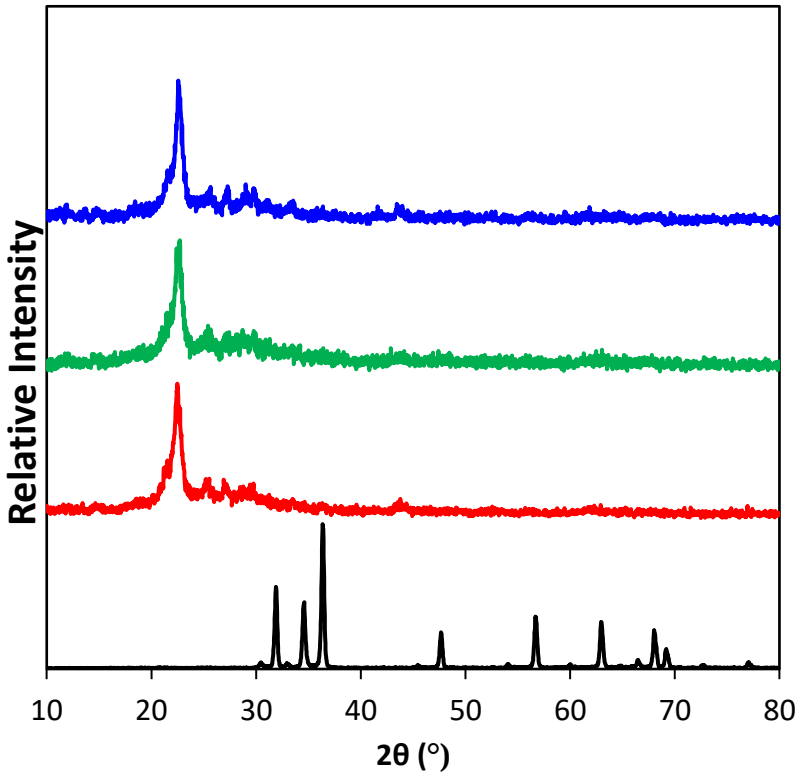

Figure 20. XRD patterns of ZnO (black), H-BEA (red), incipient wetness impregnated Zn-H-BEA (green), and ion exchanged Zn-BEA (blue).

Powder x-ray diffraction was carried out on reference samples, ion-exchanged Zn-BEA, and incipient wetness impregnated Zn-H-BEA. On the metal-loaded BEA samples, there were no characteristic peaks for ZnO, indicating that clusters of ZnO did not form in the zeolite pores. The degree of crystallinity for H-BEA was calculated to be 96.8% when compared to reference H-BEA spectra, with the main crystalline peak being the peak at $2\Theta = 22.3°$. This extent of crystallinity was preserved throughout the modified samples.

3.3 Zn K-Edge X-ray Absorption Spectroscopy

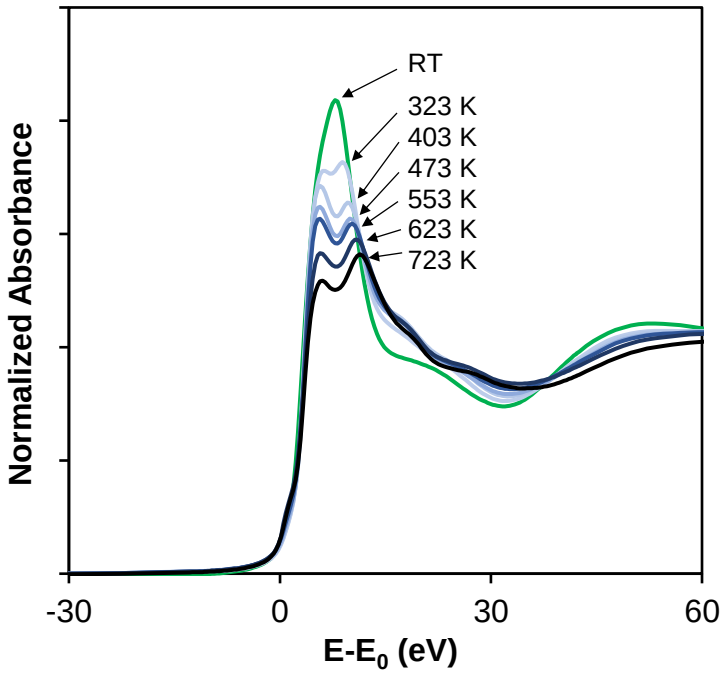

Figure 21. Normalized Zn K-edge X-ray absorption near-edge spectra of 0.08Zn-BEA at RT, 323 K, 403 K, 473 K, 553 K, 623 K, 723 K during *in situ* activation in flowing He (6.2 cm^3 g_{cat}^{-1} s^{-1}).

The work presented here focuses on elucidating the identity of Zn moieties in BEA zeolites through X-ray absorption spectroscopy with XANES analysis providing information on Zn coordination and establishing a path for EXAFS analysis to identify local structures. In the previous section, it was highlighted that: (i) Zn sites change upon thermal treatment and (ii) the acid site concentrations for these Zn-containing BEA samples are dependent not only on synthesis technique but also on thermal treatment.

The normalized Zn K-edge XANES spectra (-30 to 60 eV from the absorption edge) for the *in situ* activation of Zn-BEA 0.08 Zn/Al is shown in **Figure 21**. Spectra were taken at different temperatures during the thermal treatment process. Changes in the Zn coordination can be confirmed by comparison of edge energies between different Zn standards with absorption edges shifting to higher energies during oxidation [68]. The Zn K-edge peaks are attributed to the excitation

of Zn 1*s* electrons to higher energy bound states and therefore changes in the oxidation state of Zn is reflected in the absorbance spectrum and edge energy. At the absorption edge, the *in situ* Zn-BEA spectrum splits into two peaks as the sample undergoes thermal treatment and becomes more distinct as the temperature rises. These two peaks remain after cooling to reaction temperature (473 K) and room temperature in flowing He. The changes in features for Zn-BEA at the white line suggests that the coordination sphere of Zn sites changes significantly during the activation process. This peak morphology remains consistent during activation in either flowing He or H_2 (**Figure 22**).

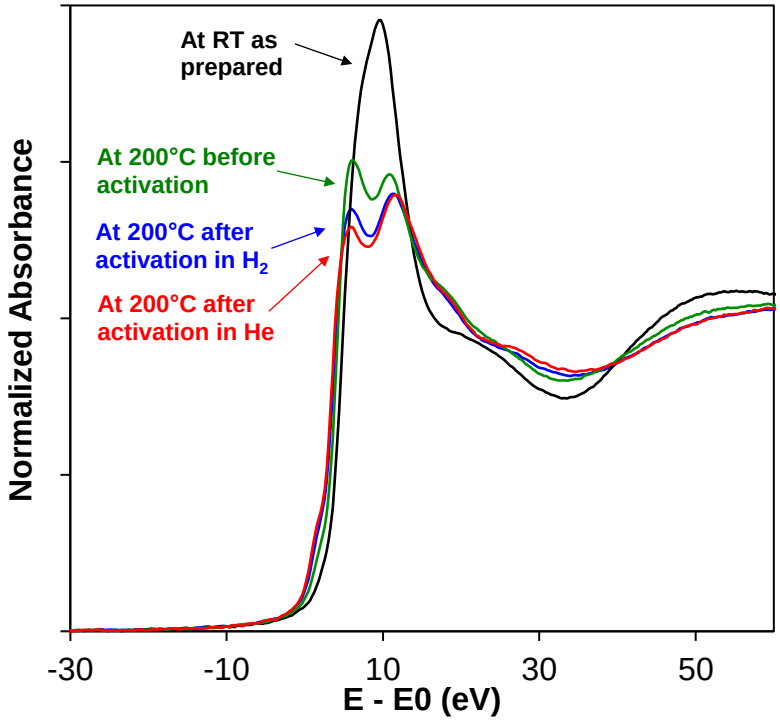

Figure 22. Normalized Zn K-edge X-ray absorption near-edge spectra of 0.35Zn-BEA before and after thermal treatment in flowing **He** and **H_2** (6.2 $cm^3\ g_{cat}^{-1}\ s^{-1}$).

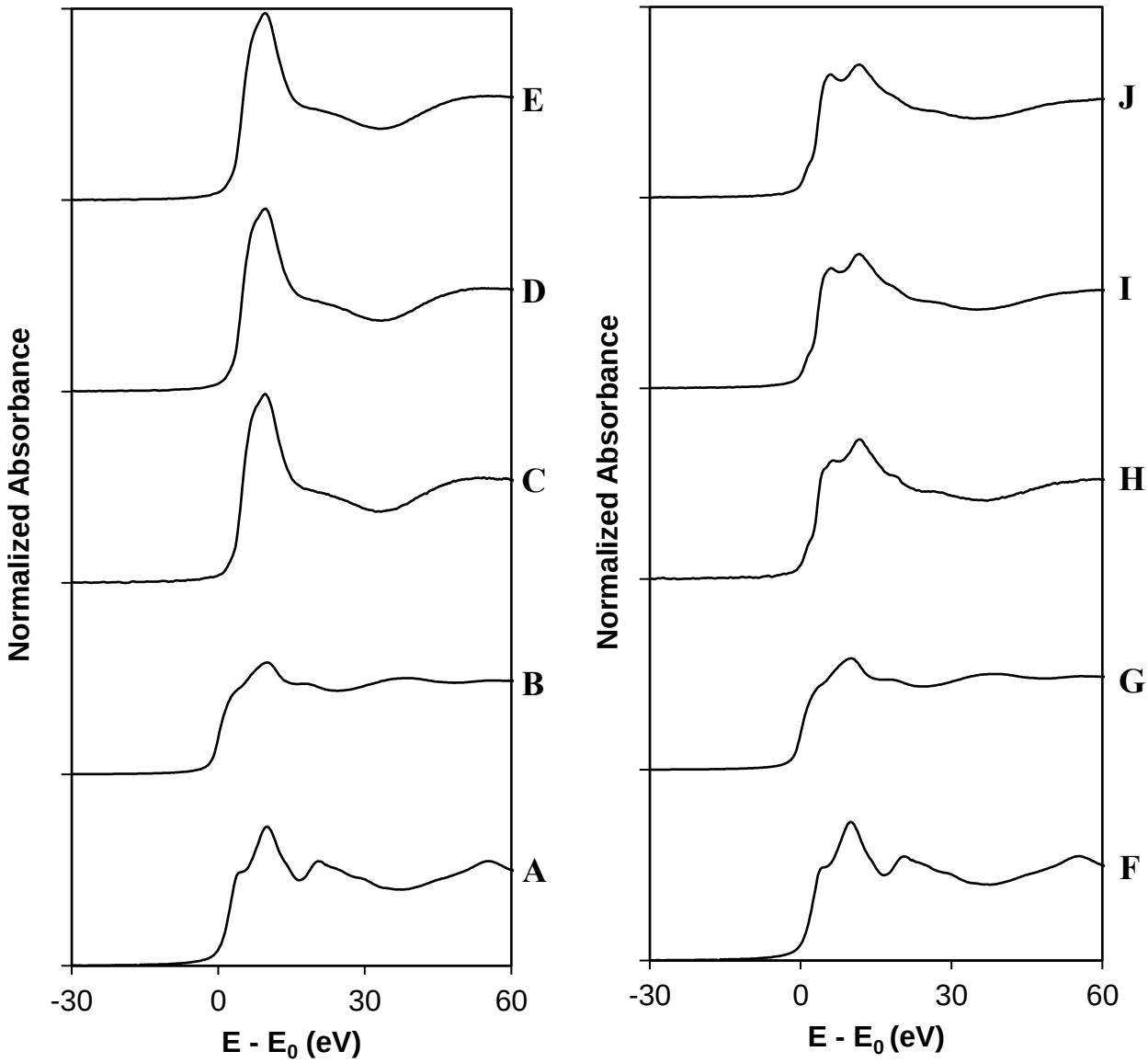

Figure 23. Normalized XANES spectra at the Zn K-edge of **(A)** zinc oxide, **(B)** metallic Zn, **(C)** 0.08Zn-BEA, **(D)** 0.19Zn-BEA, **(E)** 0.35Zn-BEA, **(F)** zinc oxide, **(G)** metallic Zn, **(H)** 0.08Zn-BEA-pt, **(I)** 0.19Zn-BEA-pt, and **(J)** 0.35Zn-BEA-pt.

A XANES spectra of metallic zinc, zinc oxide, and Zn-BEA 0.08 – 0.35 Zn/Al is shown in **Figure 23**. The edge energy for metallic Zn and ZnO was found to be 9659.0 eV and 9661.9 eV respectively and reflects an increase in oxidation state from Zn to Zn^{2+} with a step of +2.9 eV. When compared to the ZnO reference, ion exchanged Zn-BEA has even higher edge energies before and after activation, confirming the presence of Zn in higher oxidation states in the zeolite

samples compared to metallic Zn or ZnO. 0.08Zn-BEA, 0.19Zn-BEA, and 0.35Zn-BEA before activation all have edge energies of 9663.2 eV while after activation have 9662.3 eV, 9662.4 eV, and 9662.5 eV respectively (**Table 3)**.

Sample	Edge energy (eV)
Metallic Zn	9659.0
ZnO	9661.9
0.08Zn-BEA	9663.2
0.08Zn-BEA-pt	9662.3
0.19Zn-BEA	9663.2
0.19Zn-BEA-pt	9662.4
0.35Zn-BEA	9663.2
0.35Zn-BEA-pt	9662.5

Table 3. Energies at the Zn K-Edge for reference materials and Zn-BEA before and after activation.

The decrease in edge energy post-activation can be attributed to the loss of H_2O ligands and a change in Zn coordination during activation. This is supported by the spectra where a well-defined single peak in the edge region can be seen in the metallic Zn and the various Zn-BEA samples before activation **(B and C in Figure 23)**. The pre-treated Zn-BEA near-edge spectra, however, do not resemble either of the available Zn standards tested. In comparison, two peaks can be observed above the absorption edge in the spectrum taken after *in situ* thermal treatment of 0.08Zn-BEA-pt, 0.19Zn-BEA-pt, and 0.35Zn-BEA-pt **(H, I** and **J in Figure 23)** and the peak morphology resembles that of ZnO **(F)** with pre-treated Zn-BEA having a more pronounced double peak. The similarity between the edge features in ZnO (Zn^{2+} coordination) and Zn-BEA after activation spectra supports the theory that ion exchanging Zn onto H-BEA produces $Zn(OH)^+$ acid

sites on tetrahedral aluminum.[93,94] These $Zn(OH)^+$ acid sites are dehydrated during the thermal treatment and form a bridge between two tetrahedral framework alumina. Additionally, changes in Zn concentration alters the morphology of the double peak with the first peak growing and the second peak shrinking as Zn concentration increases. Whether this can be directly correlated with changes in site structure requires analysis of the EXAFS region of these spectra.

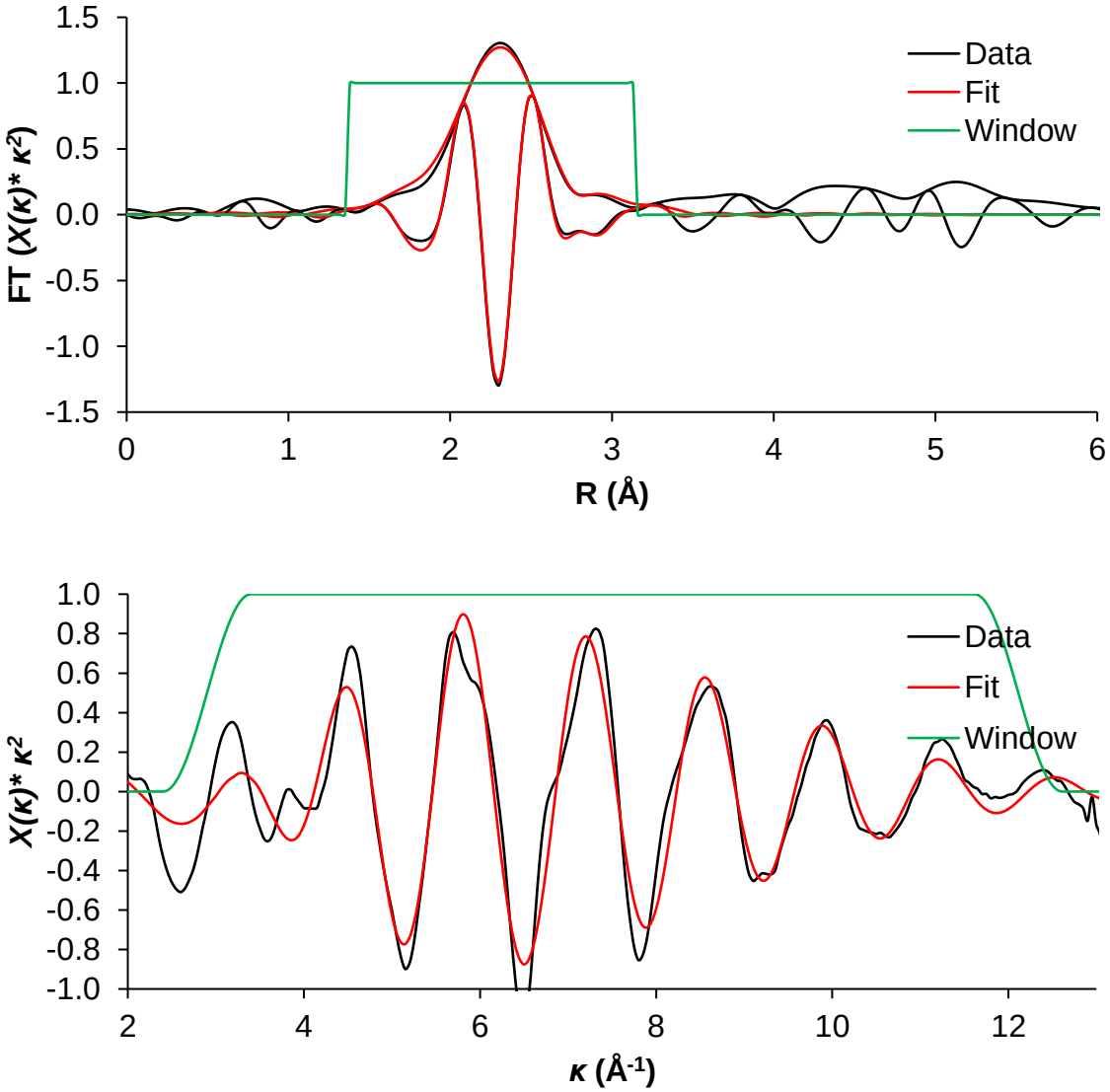

Figure 24. EXAFS data and best-fit model characterizing the metallic Zn foil sample. Spectra were collected at room temperature. Top: k^2-weighted magnitude and imaginary part of the Fourier transform of the data (black line) and fit (red line). Bottom: k^2-weighted EXAFS function of the data (black line) and fit (red line). The green line in both plots represents the window used to determine the number of independent parameters.

EXAFS was extracted in k-space and Fourier-transformation was done on the k^2- or k^3-weighted EXAFS function. Relevant back-scattering paths were generated by FEFF6 using crystallographic information from hexagonal ZnO and metallic Zn taken from The Materials Project and Artemis.[72–74,95–110] S_0^2 was determined to be 0.96 ± 0.10 for the Zn K-edge from experimentally fitting Zn foil with the fit found in **Figure 24**. S_0^2 has been shown to be a shared value for all EXAFS measurements of a specific element. This allows for the quantification of the coordination number and bond distance for a given sample provided it has the same element core-absorber.[111]

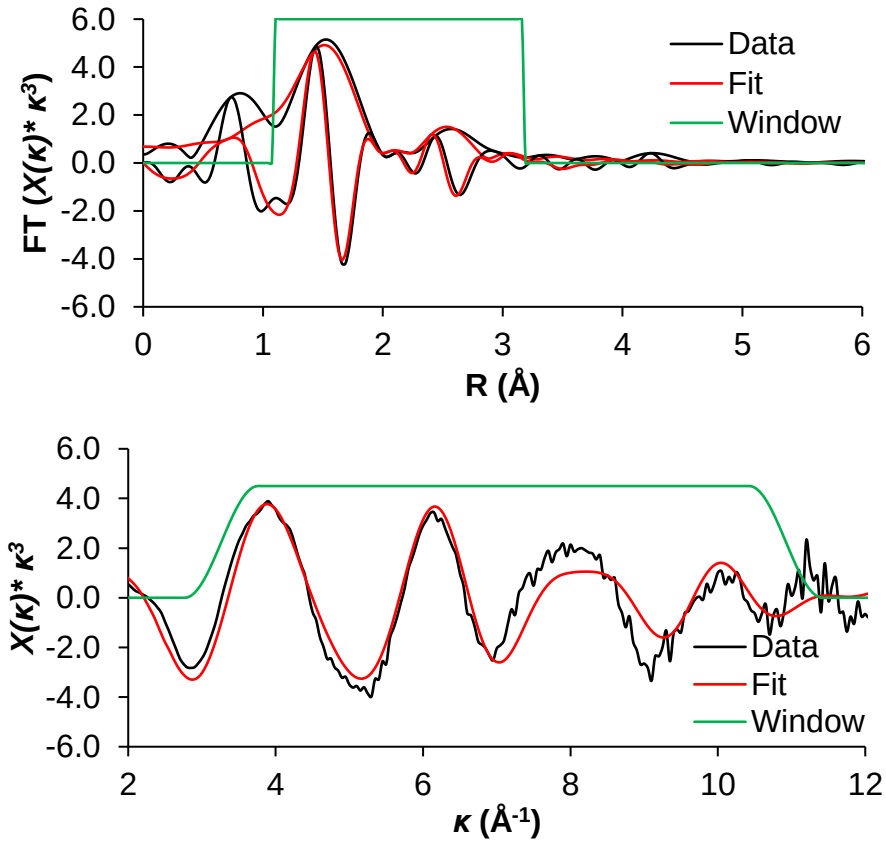

Figure 25. EXAFS data and best-fit model characterizing the 0.19Zn-BEA sample. Spectra were collected at room temperature in flowing helium. Top: k^3-weighted magnitude and imaginary part of the Fourier transform of the data (black line) and fit (red line). Bottom: k^3-weighted EXAFS function of the data (black line) and fit (red line). The green line in both plots represents the window used to determine the number of independent parameters.

Fitting was carried out simultaneously through the samples, effectively constraining fits with shared parameters to allow for more reliable models. ΔE_0, the energy shift used to align the energy grids of the theoretical spectrum to the experimental spectrum, was shared for each individual scattering path amongst all of the samples because this value is unique to the back-scattering atom from which the FEFF generated the scattering path.[112] As the samples were measured at the same temperature, the thermal component of σ^2 can be ignored. σ^2, a measure of the mean square variance in bond distance, also contains a structural component. Due to structural disorder, the scatterers around the absorber have still some variances in the path length between them.[70] This allows for identical scattering paths to share one σ^2 parameter among the different samples because the extent of structural disorder will remain fixed. The spectra demonstrate a lack of Zn-Zn and Zn-Si scattering for all samples regardless of Zn loading and temperature treatment. This is confirmed by null models rejecting these scattering paths with unrealistic path parameters or poor fits. These samples were fitted with two well-defined scattering paths, Zn-O and Zn-Al. The Al shell was modeled as a single scattering path rather than a double or obtuse triangle scattering path. EXAFS spectra and fitting of these catalysts can be found in **Figure 49 - Figure 56** with the full fitting parameters and constraints listed in **Table 4**. A sample of the results of the simultaneous fit is shown in the figure above.

The lack of Zn-Zn contributions in the first or second coordination shell indicates that the Zn atoms were exchanged into isolated cation-exchange positions without the formation of a significant amount of Zn clusters. The first coordination shell was identified to be Zn-O contributions, which was observed throughout the range of samples. Of all the samples, 0.08Zn-BEA had the most unique features, suggesting that Zn^{2+} sites are better defined at low ion exchange ratios. **Figure 26** depicts the number of neighboring O and Al atoms in Zn-BEA samples. Note

that the number of oxygen neighbors decreases after each temperature treatment. This suggests that fresh, as-prepared samples of Zn-BEA have water coordinated to Zn sites within BEA and that the temperature treatment dehydrates the surface of the catalyst. The change in behavior in the Al coordination shell for the highest concentration samples, 0.35Zn-BEA and 0.35Zn-BEA-pt, suggests that temperature treatment can produce varying Zn^{2+} site structures depending on the exchange ratio.

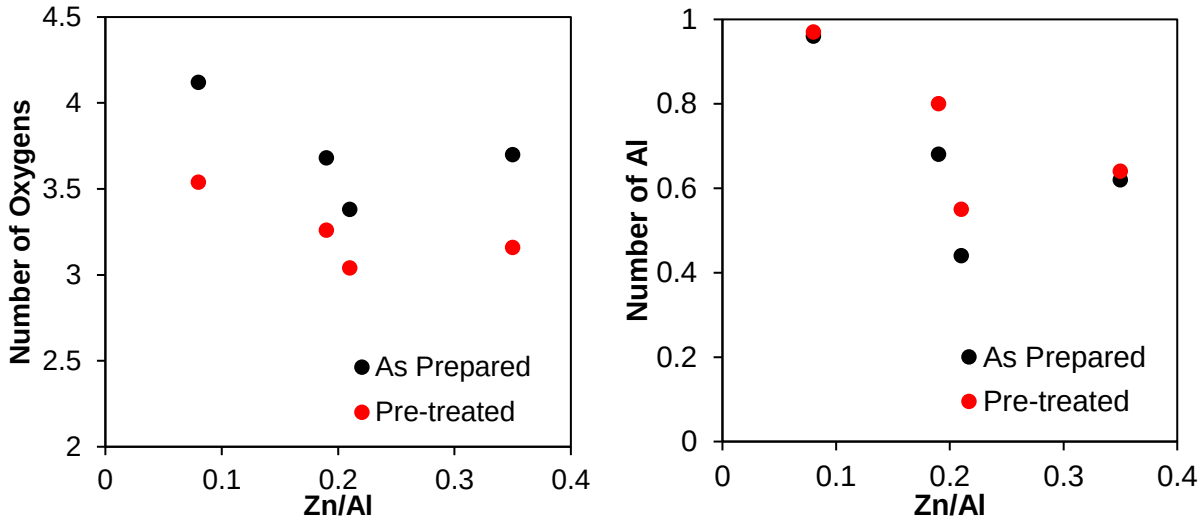

Figure 26. Number of neighboring O and Al atoms as a function of Zn content for as prepared and pre-treated samples.

There was negligible change in oxygen bond distance between as prepared and pre-treated samples. However, **Figure 27** shows a strong correlation between oxygen bond distance and Zn concentration, suggesting that Zn has an increasingly strong interaction with framework oxygen as the degree of ion exchange decreases. Previous simulations of the local environment of Zn^{2+} at three preferential ion exchange positions resulted in bimodal distributions of Zn-O distances.[30] Zn^{2+} exchanged at six-membered rings have an average bond distance of 1.95 Å, five-membered rings have an average bond distance of 2.08 Å, and 2.01 Å for four-membered rings. This suggests

that the preferential ion exchange positions for Zn shifts between these sites as more Zn is introduced to the zeolite.

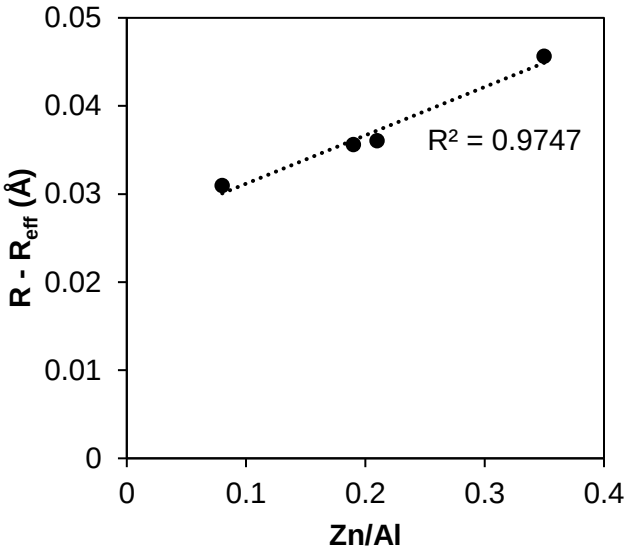

Figure 27. Changes in Zn-O bond length as determined from EXAFS spectra fitting.

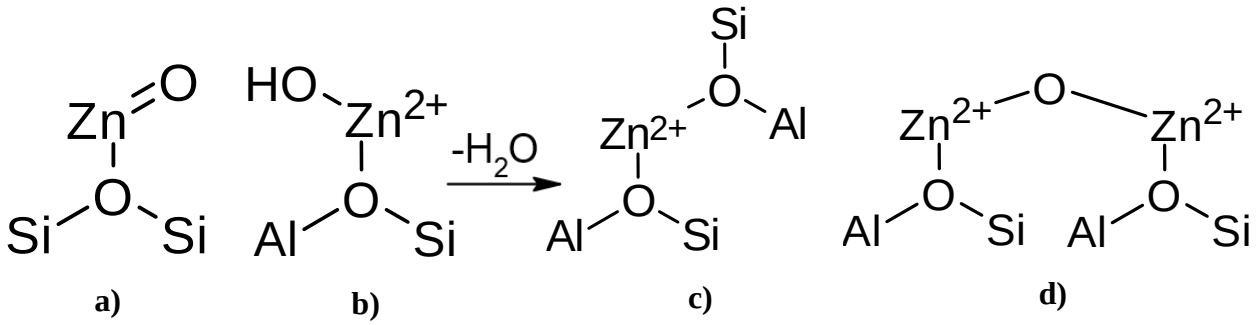

Figure 28. Possible configurations of Zn sites in ion exchanged Zn-BEA.[30,53,56]

It has been proposed that Zn sites in Zn-exchanged zeolites in the range of 0 – 0.26 Zn/Al can take the form of four possible active site configurations, found in **Figure 28**. The Lewis acidic Zn^{2+} cations may exist as **a)** extra-pore neutral ZnO or neutral ZnO located at the pore wall, **b)** ion exchanged as $Zn(OH)^{+}$ to one tetrahedral aluminum site ($Zn/Al \leq 1.00$), **c)** ion-exchanged as Zn^{2+} to two tetrahedral aluminum sites ($Zn/Al \leq 0.50$) while requiring close proximity to neighboring Al^{3+} sites, , or **d)** $[Zn\text{-}O\text{-}Zn]^{2+}$ cations charge balanced by two framework Si-O-Al groups with the

framework aluminum atoms located further apart up to 1.2 nm.[30,113] Zn^{2+} acid sites that are stabilized by two tetrahedral framework aluminum atoms are the preferential ion exchange positions for Zn given that the aluminum atoms are sufficiently close together.[114] For framework atoms further apart, the fourth configuration is preferable. Note that the formation of $Zn(OH)^{+}$ species has been reported only for hydrated zeolites.[115] It has also been shown by XAS on Zn-exchanged ZSM-5 that $Zn(OH)^{+}$ species are not stable and dehydrate upon thermal treatment.[53] As a result, the single to double peak transition during the temperature treatment of Zn-BEA suggests that Zn sites change configuration from $Zn(OH)^{+}$ sites to either the two tetrahedrally Al bound Zn^{2+} sites or the bridged $[Zn\text{-}O\text{-}Zn]^{2+}$ sites. Dehydration of the Zn^{2+} sites can be supported by the acid site titration experiments in which the Brønsted acid site concentration decreases after activation across the board for Zn-BEA catalysts.

Chapter 4 Role of Zn Sites in Reactions of Alcohols

4.1 Methanol Dehydration Kinetics Measurements

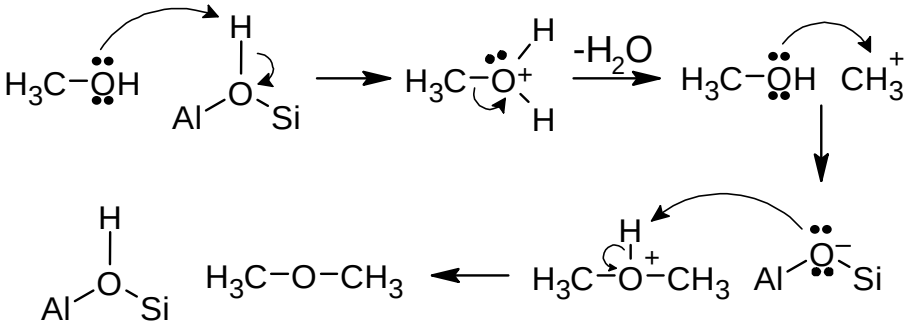

Figure 29. Mechanism of methanol dehydration to DME over a Brønsted acid site.

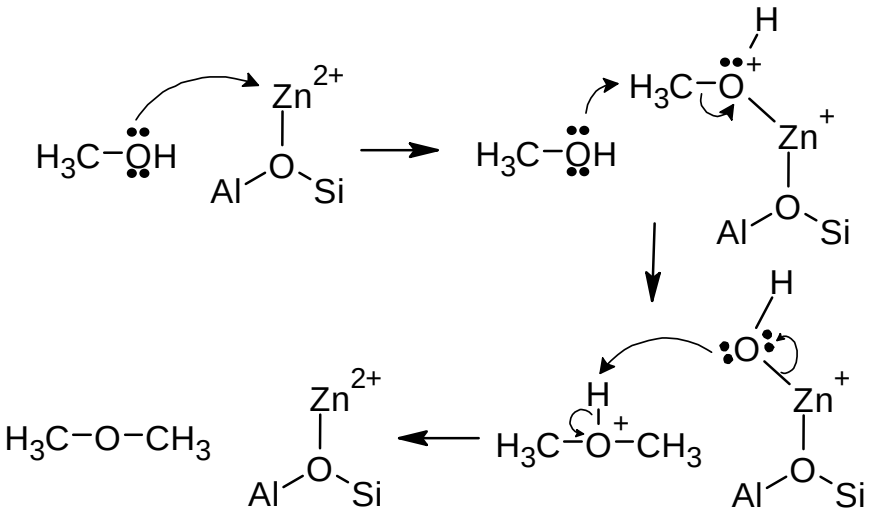

Figure 30. Mechanism of methanol dehydration to DME over a Zn^{2+} Lewis acid site.

This work aims to determine the role of different Zn species on reactions of oxygenates with simple alcohol dehydration reaction. The reaction shown in **Figure 31** is the dehydration of methanol to DME over H-BEA in addition to a series of Na-BEA, Zn-BEA, and Zn-H-BEA catalysts. Sodium was chosen to be exchanged with protons on H-BEA to vary Brønsted acid sites because they have been shown to not participate in methanol dehydration. The reference Na-BEA catalysts are used to establish a baseline for turnover rate per acid site (dashed line) as to compare the modified Zn-exchanged and Zn-impregnated BEA samples. Because the turnover rate for this

exothermic reaction was proportional to the acid site concentration, the Madon-Boudart criterion was satisfied.[88] This eliminates the possibility of transport limitations affecting the measured catalytic rates in this reactor system.

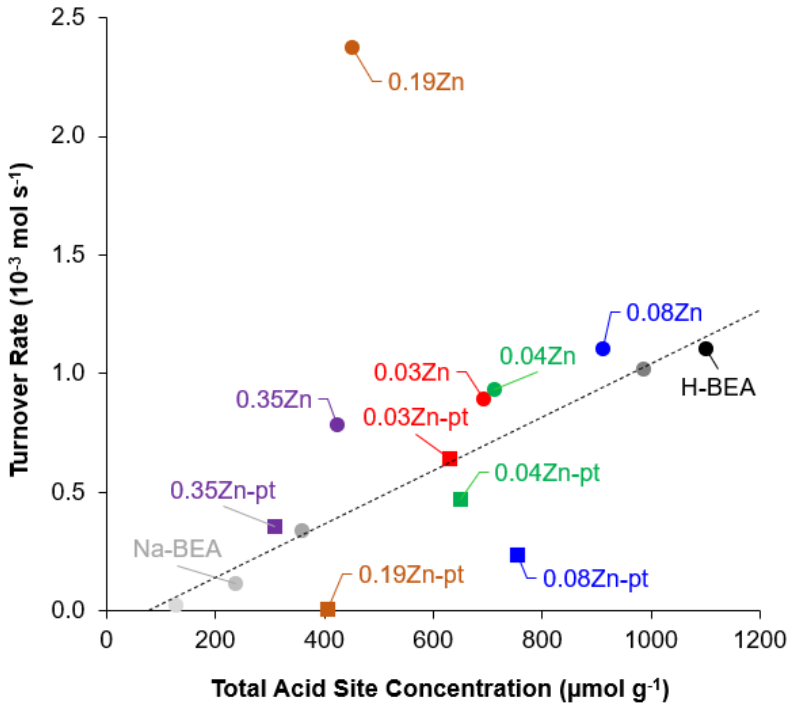

Figure 31. Dimethyl ether turnover rates as a function of total acid site concentration on H-BEA (●), Na-BEA-1 (●), Na-BEA-2 (●), Na-BEA-3 (●), Na-BEA-4 (●), 0.03Zn-BEA (●), 0.03Zn-BEA-pt (■), 0.04Zn-BEA (●), 0.04Zn-BEA-pt (■), 0.08Zn-BEA (●), 0.08Zn-BEA-pt (■), 0.19Zn-BEA (●), 0.19Zn-BEA-pt (■), 0.35Zn-BEA (●), and 0.35Zn-BEA-pt (■). The dashed lines represent baselines for acid site reactivites established from H-BEA and Na-BEA samples.

The addition of Zn sites to BEA zeolite does not appear to significantly change the measured turnover rate. 0.03Zn-BEA, 0.04Zn-BEA, 0.35Zn-BEA all exhibited a slightly higher rate of DME formation when normalized by their respective total acid site concentrations compared to the reference H-BEA and various exchange ratios of Na-BEA. The only exception was 0.19Zn-BEA, with a turnover rate nearly 5-fold greater than the expected turnover rate. Pre-treatment of the catalysts by *in situ* heating at 723 K causes the measured turnover rate to decrease below their respective catalysts before activation. This is accompanied by a loss in total acid site

concentration that reflects the loss of Brønsted acid sites during the Zn site dehydration process. The magnitude of change in turnover rates before catalyst activation increases from 0.03 Zn/Al to 0.19 Zn/Al, suggesting that Zn^{2+} bound to two tetrahedral aluminum sites is not as effective as $Zn(OH)^{+}$ sites at methanol dehydration as the concentration of these Zn sites reach a maxima in the 0.19Zn-BEA sample.[30]

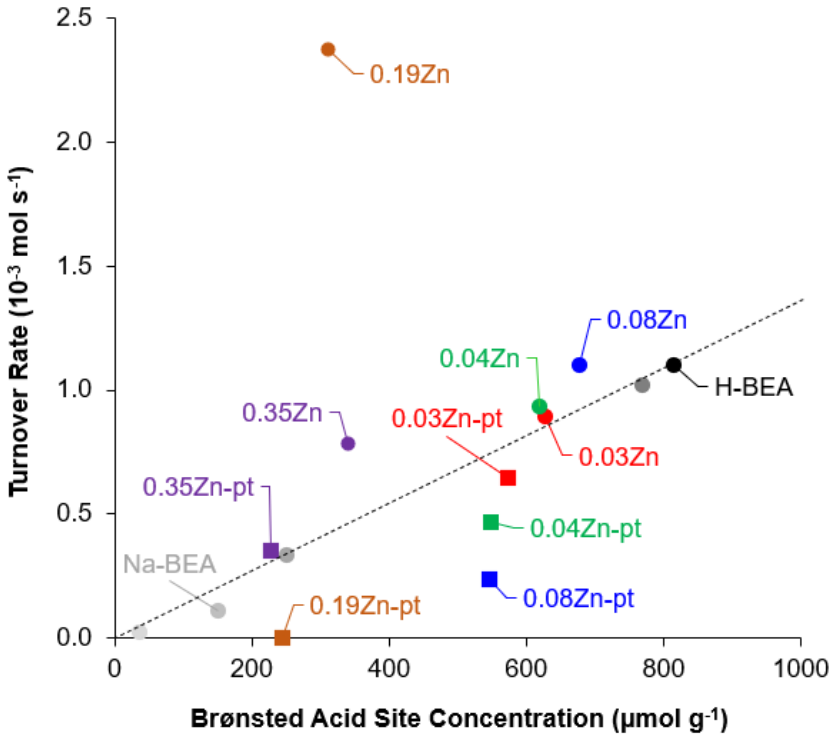

Figure 32. Dimethyl ether turnover rates as a function of Brønsted acid site concentration on H-BEA (●), Na-BEA-1 (●), Na-BEA-2 (●), Na-BEA-3 (●), Na-BEA-4 (●), 0.03Zn-BEA (●), 0.03Zn-BEA-pt (■), 0.04Zn-BEA (●), 0.04Zn-BEA-pt (■), 0.08Zn-BEA (●), 0.08Zn-BEA-pt (■), 0.19Zn-BEA (●), 0.19Zn-BEA-pt (■), 0.35Zn-BEA (●), and 0.35Zn-BEA-pt (■). The dashed lines represent baselines for acid site reactivites established from H-BEA and Na-BEA samples.

Figure 32 shows the same turnover rates for these catalysts as a function of Brønsted acid site density. The DME turnover rates for the 0.03 – 0.19 Zn/Al samples indicates that the both the Brønsted acid sites and the Lewis acidic Zn^{2+} sites are participating in the dehydration reaction. Again, the activated catalysts had lower turnover rates with 0.03 – 0.19 Zn/Al samples falling

below the baseline as well. For 0.35Zn-BEA, the $[Zn\text{-}O\text{-}Zn]^{2+}$ bridged sites exhibited a turnover rate that fell on the baseline normalized by Brønsted acid site concentration. Differences in acidity between these three forms of acid sites can contribute to the changes in turnover rates between ion exchange samples.

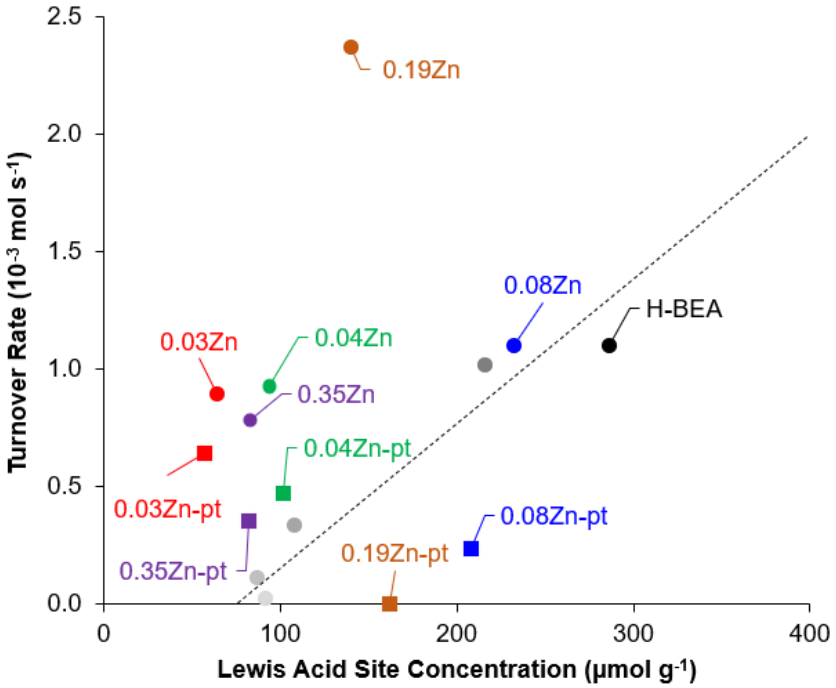

Figure 33. Dimethyl ether turnover rates as a function of Lewis acid site concentration on H-BEA (●), Na-BEA-1 (●), Na-BEA-2 (●), Na-BEA-3 (●), Na-BEA-4 (●), 0.03Zn-BEA (●), 0.03Zn-BEA-pt (■), 0.04Zn-BEA (●), 0.04Zn-BEA-pt (■), 0.08Zn-BEA (●), 0.08Zn-BEA-pt (■), 0.19Zn-BEA (●), 0.19Zn-BEA-pt (■), 0.35Zn-BEA (●), and 0.35Zn-BEA-pt (■). The dashed lines represent baselines for acid site reactivites established from H-BEA and Na-BEA samples.

A trend can be seen for 0.03 – 0.08 Zn/Al, representing the ability of $Zn(OH)^{+}$ to facilitate methanol dehydration. Another trendline could potentially be formed by the Zn^{2+} coordinated to two tetrahedral aluminum sites in the 0.03 – 0.08 Zn/Al activated samples. This data suggests that two lines can be drawn for turnover rate as a function of Lewis acid site concentration to represent each of the Lewis acid sites and their respective acid strengths. Understanding and isolating how

these acid sites coordinate with reaction intermediates formed by Brønsted acid catalyzed mechanisms plays an important role in tuning catalyst selectivity in Zn-modified zeolites.

Chapter 5 Role of Zn Sites in Co-fed Oxygenate and Alkane Reactions

5.1 Establishing Oxygenate Reaction Network

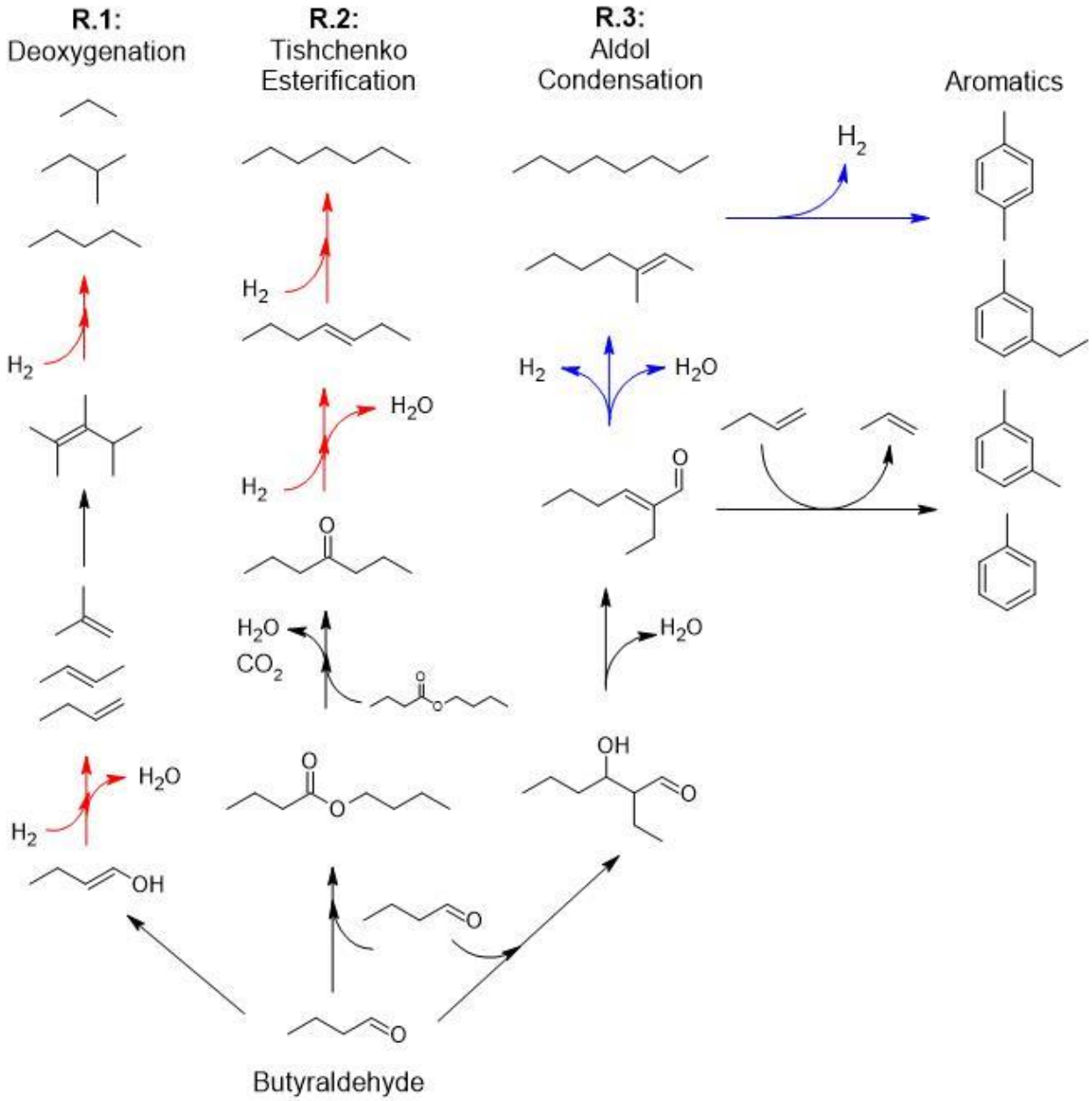

Scheme 1. Reaction network for acid catalyzed oxygenate turnover on H-BEA zeolite with butyraldehyde being shown as the representative reactant. Red arrows indicate steps in which H_2 is needed and blue arrows indicate steps in which H_2 is produced.

The aim of the work presented here is to coordinate the identities of Zn sites with the established reaction network to elucidate the role of Zn in acid-catalyzed reactions with oxygenates and alkanes. Development of the proposed oxygenate reaction network was based on similar Brønsted acid catalyzed reactions on MFI and BEA zeolites.[64] The conversion of butyraldehyde on Brønsted acid sites can be broken down into three primary pathways, each containing characteristic species prior to ring closing reactions to form arenes. The deoxygenation pathway is characterized by selectivity to C_3-C_5 paraffins/olefins while selectivity to butyl butyrate and C_7 paraffins/olefins. Meanwhile, presence of 2-ethyl-2-hexenal and C_8 paraffins/olefins indicate acid-catalyzed aldol condensation. In the absence of external hydrogen typically generated through steam reforming reactions, the molecular hydrogen needed for many of the steps (shown in red) can be obtained by converting a portion of the reactant to arenes during hydrogen transfer reactions. Addition of co-fed light alkanes (e.g. isobutane) aims to eliminate formation of undesirable products by enabling direct hydrogen transfer from the light alkanes to unsaturated bonds in oxygenates. While Zn sites in zeolite channels have been shown to be effective for alkane activation, whether oxygenate conversion will interface with alkane activation cycles in the same way as the previously mentioned hydrodesulfurization or dehydrocyclization reactions remains to be seen.

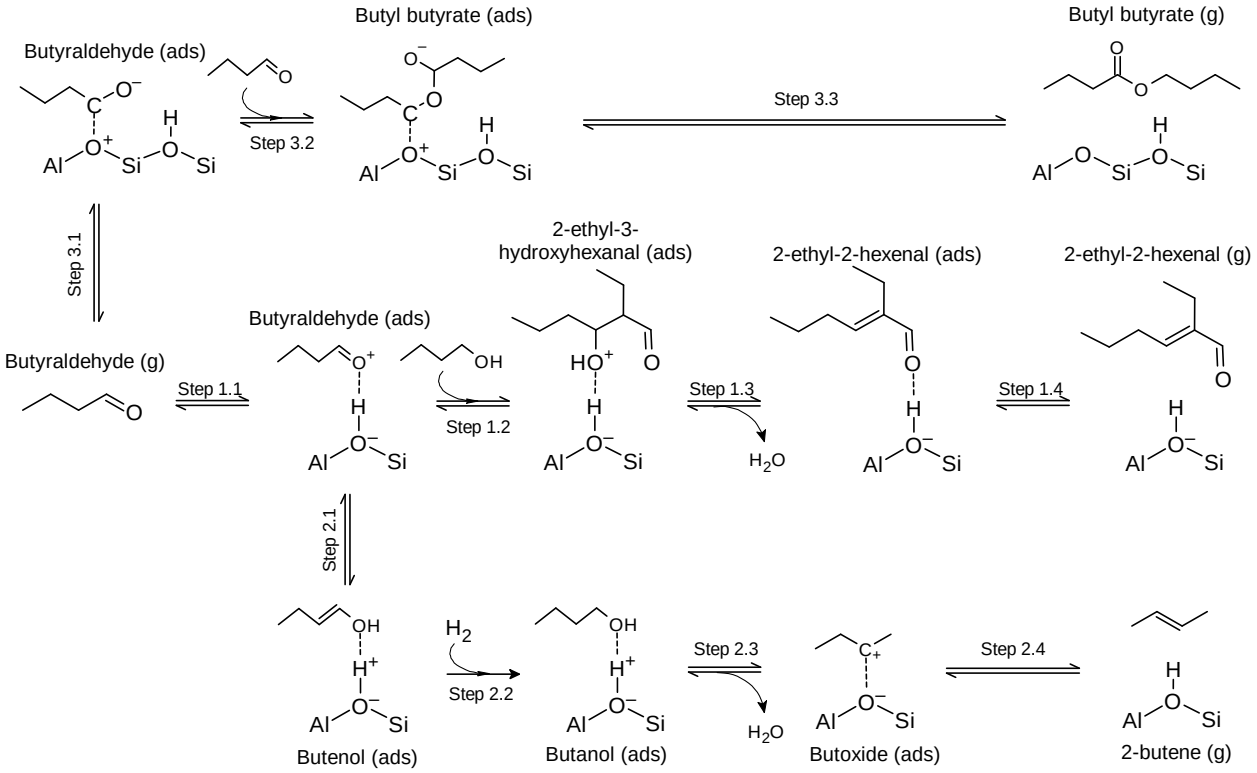

Scheme 2. Mechanisms for the formation of the primary products of the deoxygenation, aldol condensation, and Tishchenko-esterification pathways in n-butanal over Brønsted acid sites.[64,116]

Scheme 2 and **Scheme 3** show the mechanisms for the formation of the primary products over Brønsted acid sites and Zn^{2+} acid sites, respectively. The mechanisms for forming primary products from each pathway are different due to Brønsted and Lewis acid chemistry. However, the primary products remain the same from deoxygenation, Tishchenko-esterification, and aldol condensation (butyl butyrate, 2-ethyl-2-hexenal, and butenes). More importantly, Zn^{2+} introduces new mechanisms for hydride abstraction and hydrogenolysis of alkanes. The example in **Scheme 4** is shown with pentane, however any of the paraffins generated by Brønsted acid catalyzed oxygenate conversion will apply. Hydride abstraction from Zn^{2+} sites provides the molecular hydrogen needed for some of the Brønsted acid catalyzed reactions that were originally obtained through aromatization reactions. Pentane is activated by the Zn^{2+} sites, forming a pentylzinc intermediate followed by β-hydride elimination into a pentene. Alternatively, pentane can

coordinate to Zn^{2+} in addition to a neighboring Brønsted acid site. Scission of the C-C bond in the pentylzinc intermediate forms a methylzinc and a butoxy intermediate – desorbing to form butane.

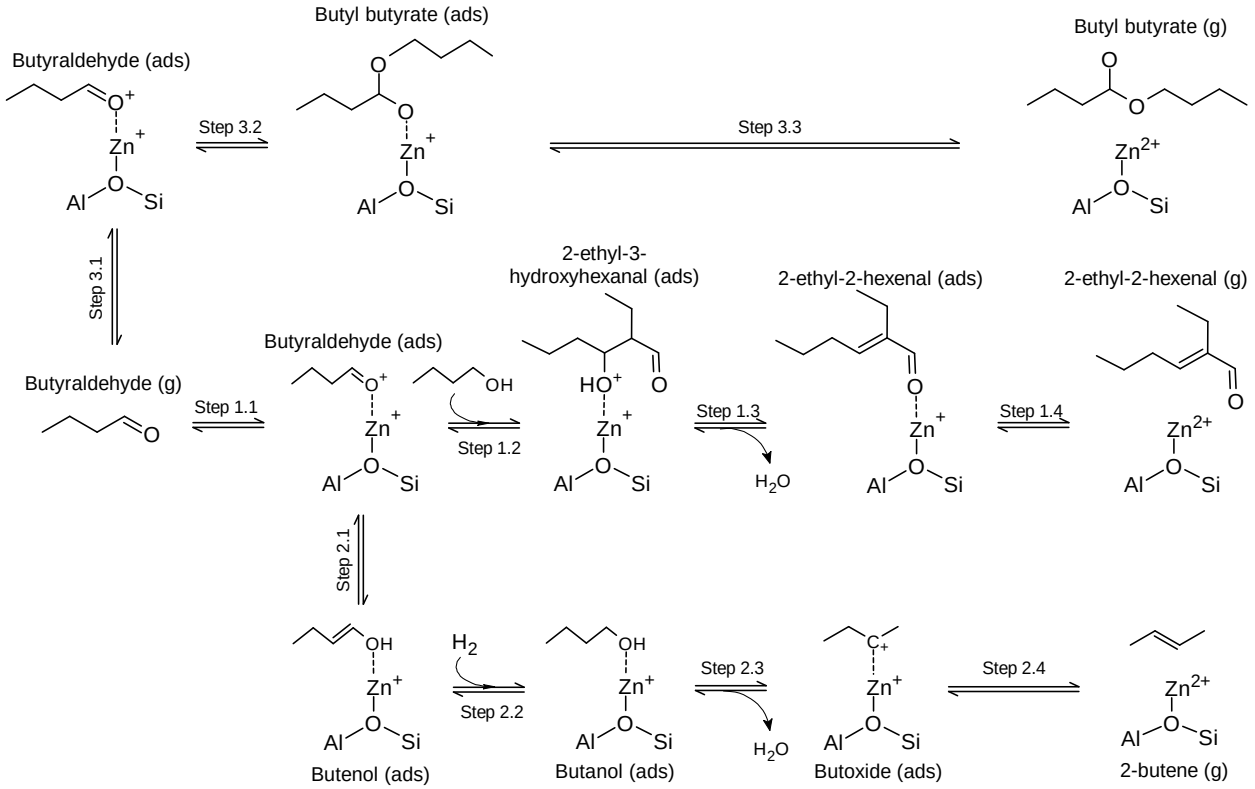

Scheme 3. Mechanisms for the formation of the primary products of the deoxygenation, aldol condensation, and Tishchenko-esterification pathways in n-butanal over Zn^{2+} acid sites.[58,116]

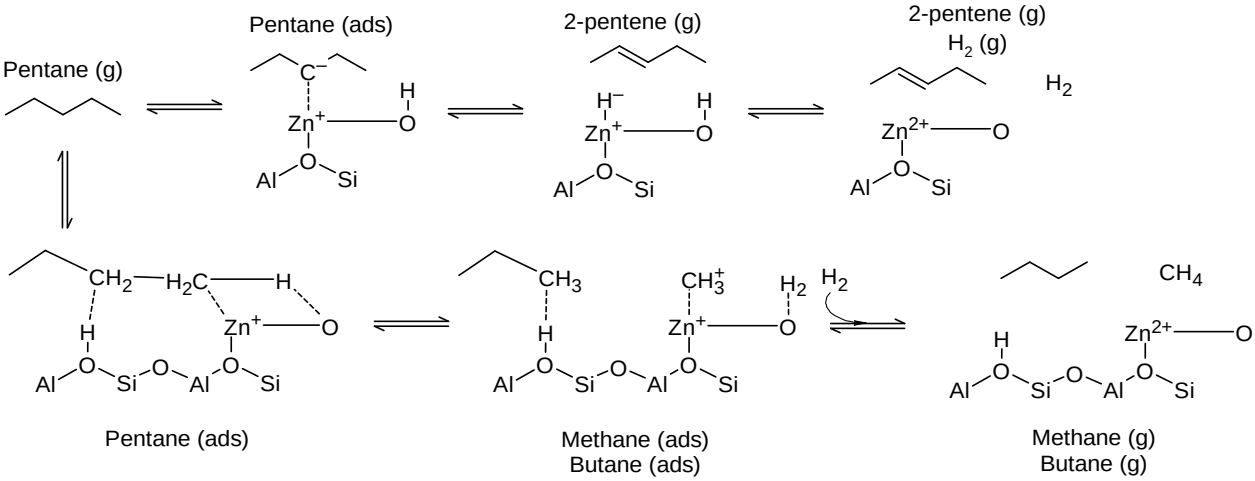

Scheme 4. Potential mechanisms for alkane transformation over ZnO sites in Zn-modified BEA.[58,89]

5.2 Co-fed Isobutane and Butyraldehyde Reaction Kinetics

Figure 34 shows a comparison of the effect of Zn ion-exchange and post-synthesis temperature treatment on H-BEA with regards to site-time yield (STY) as a function of turnover number at 473 K. Feeds of pure isobutane on each of the catalyst samples had negligible conversion. Aldol condensation was the dominant reaction pathway regardless of feed composition and catalyst preparation. Zn-BEA before activation **(c)** has a similar STY for aldol condensation and slightly more prominent Tishchenko-esterification and deoxygenation product formation in a feed with n-butanal. Upon activation of Zn-BEA **(e)**, the formation of aldol condensation's primary product, 2-ethyl-2-hexenal, was dramatically reduced. Formation of aromatics through any of the pathways on Zn-BEA was suppressed, suggesting that the acid-catalyzed reactions did not proceed as quickly to the end-point on exchanged catalysts when compared to proton form BEA. Addition of isobutane to the feed has little impact on the total STY on H-BEA **(b)** with a slight decrease in aldol condensate product formation compensated by an uptick in aromatic product formation. Exchanging Brønsted acid sites with Lewis acidic Zn sites in co-fed isobutane and n-butanal **(f)**, however, has a much different effect. STY for aldol condensation pathway products was significantly higher (29.0 vs 8.9 at similar TON) with a similar deoxygenation and Tishchenko-esterification STY. When Zn-BEA undergoes activation and $Zn(OH)^+$ sites dehydrate to form either Zn bonded to two tetrahedral framework Al or two tetrahedrally bonded Zn sites bridged by an oxygen atom (Zn-O-Zn), the overall STY remains higher when H-BEA. The aldol condensation pathway decreased compared to pre-activation (15.2 vs 22.2 at similar TON). In contrast, the STY for Tishchenko-esterification and deoxygenation pathways are the highest out of any of the reactions at 473 K. These results on ion exchanged Zn catalysts indicate that Lewis acid Zn sites influence pathway selectivities in co-fed oxygenate and alkane reactions.

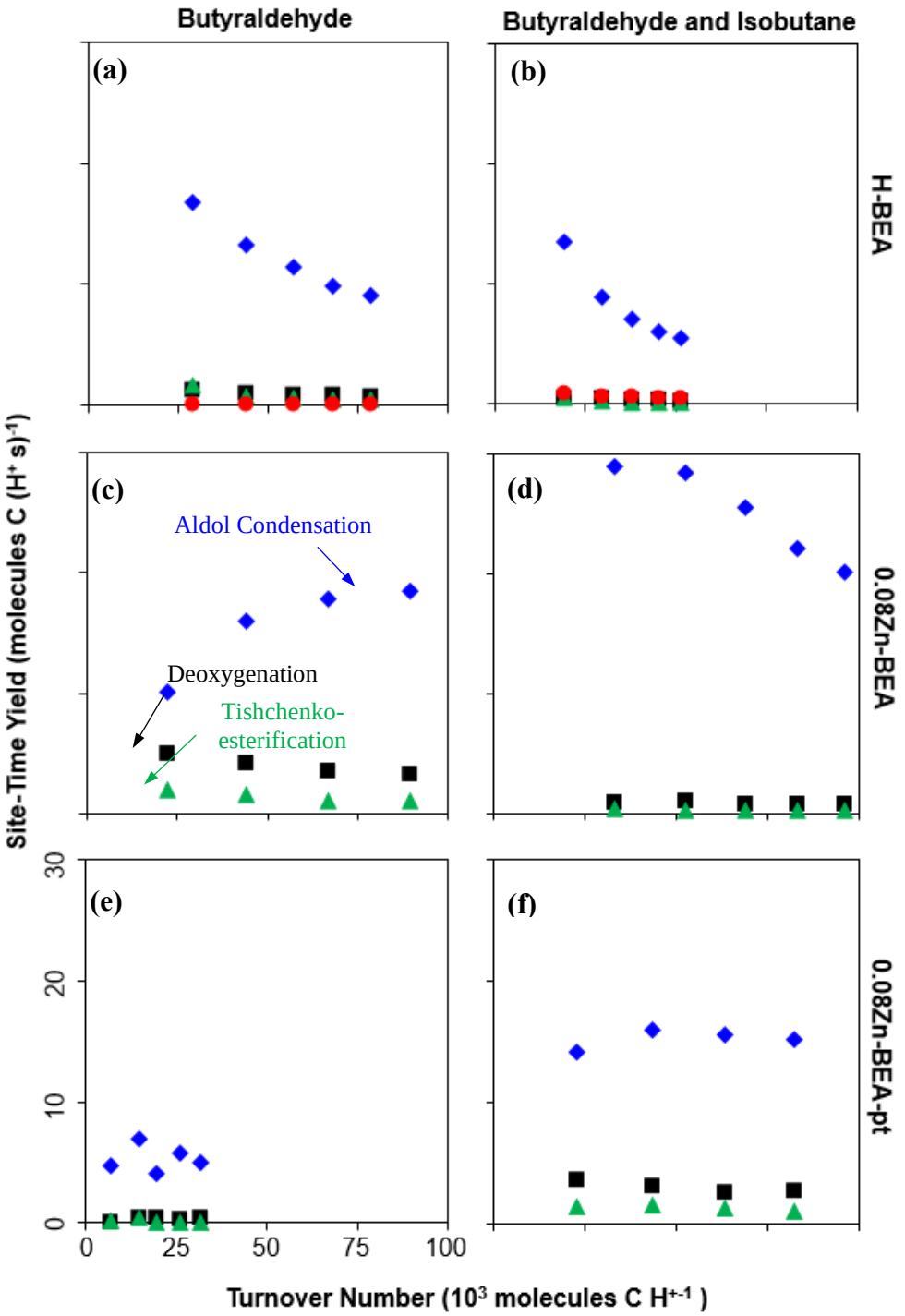

Figure 34. Site time yield (per accessible proton) of reaction pathway products (◆ aldol condensation, ■ deoxygenation, ▲ Tishchenko-esterification, and ● aromatics) at **473 K** as a function of turnover number on **(a)** H-BEA in 1.1 kPa butyraldehyde, **(b)** H-BEA in 1.1 kPa butyraldehyde and 50 kPa isobutane, **(c)** Zn-BEA 0.08 Zn/Al before activation in 1.1 kPa butyraldehyde, **(d)** Zn-BEA 0.08 Zn/Al before activation in 1.1 kPa butyraldehyde and 50 kPa isobutane, **(e)** Zn-BEA 0.08 Zn/Al after activation in 1.1 kPa butyraldehyde, and **(f)** Zn-BEA 0.08 Zn/Al after activation in 1.1 kPa butyraldehyde and 50 kPa isobutane.

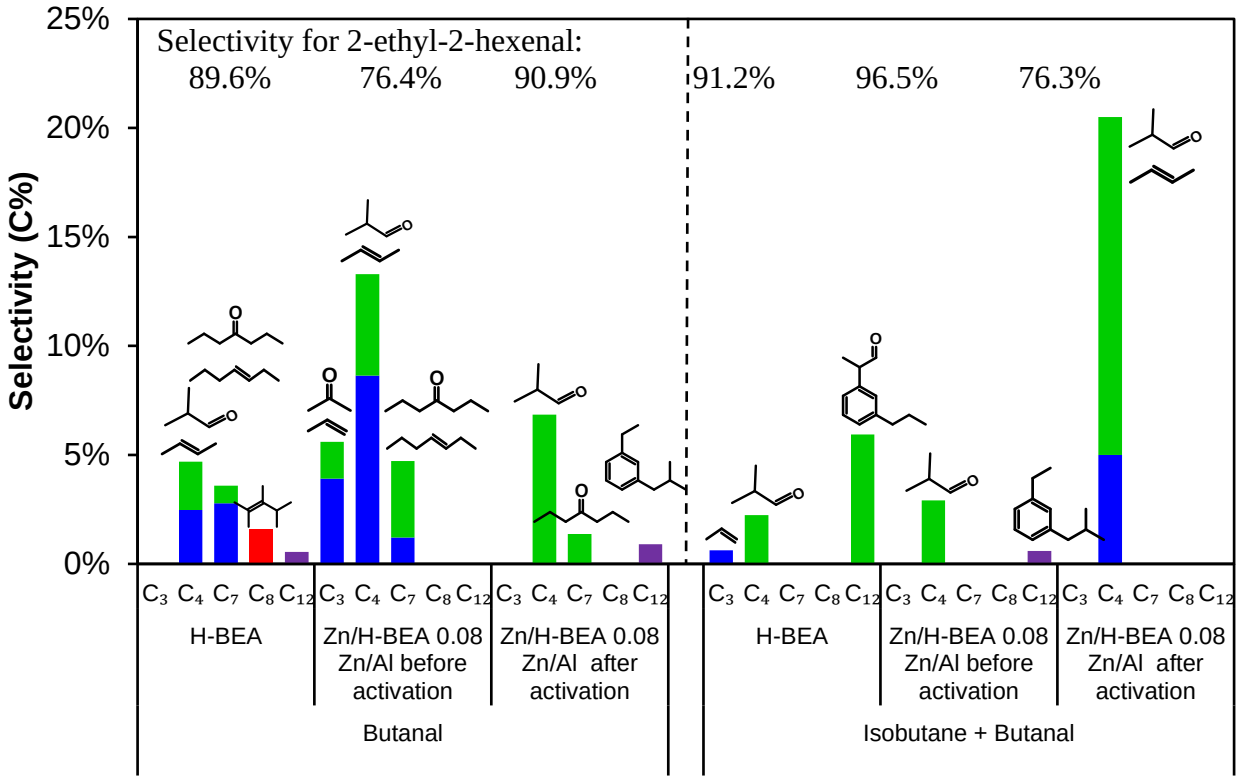

Figure 35. Selectivity (per carbon %) of classes of species (■ linear alkenes, ■ branched alkenes, ■ aromatics, and ■ oxygenates) at 473 K on H-BEA and Zn-BEA 0.08 Zn/Al before/after activation in a feed of 1.1 kPa n-butanal (left) and 1.1 kPa n-butanal and 50 kPa isobutane (right) at similar turnover numbers. Selectivity for primary product (2-ethyl-2-hexenal) was not displayed to improve visibility of other products.

Aside from comparing STY per reaction pathway, breaking down the pathways into classes of species can also provide insight into Zn site effects. Comparisons at similar turnover numbers, the cumulative number of carbon in the effluent hydrocarbon products normalized per Brønsted acid site, allow for more accurate representations of the reactivities of different catalysts than comparing at similar times on stream.[117] Turnover number condenses reaction conditions of bed loading, catalyst site density, inlet concentrations, and space velocity into a single progress variable.

Reactions of pure isobutane had conversions ranging from 0.05 – 0.2% on the H-BEA and Zn-BEA, indicating that dehydro-oligomerization of isobutane occurs to a negligible extent in

parallel with n-butanal conversion paths. The absence of trimethylpentane in the product stream is consistent with a negligible conversion of isobutane.

Selectivity for 2-ethyl-2-hexenal was not displayed in **Figure 35** to be able to compare non-aldol condensation products as 2-ethyl-2-hexenal formation is dominant at this temperature regime. For a feed of pure n-butanal, hydrated $Zn(OH)^+$ sites on Zn-BEA before activation showed an increase in selectivity for propenes and butenes when compared to H-BEA (12.5% vs. 2.5%) coupled with a lower selectivity for 2-ethyl-2-hexenal (76.4% vs. 89.6%). After dehydrating Zn sites through activation, n-butanal undergoes Tishchenko-esterification-ketonization to form C_4 and C_7 oxygenates in addition to 90.9% selectivity for the primary selectivity for aldol condensation product, 2-ethyl-2-hexenal. Coupled with the site-time yield values for these reaction pathways, this suggests that bridged Zn^{2+} sites formed from dehydrating Zn sites hinder neighboring Brønsted acid sites from performing acid-catalyzed deoxygenation of n-butanal. $Zn(OH)^+$ sites on Zn-BEA before activation, however, have the highest selectivity and STY for C_3 and C_4 olefins and oxygenates out of all three types of acid sites in n-butanal.

Co-fed isobutane inhibits the formation of linear C_4 and C_7 olefins on H-BEA and Zn-BEA before activation with both catalysts preferentially catalyzing oxygenates from aldol condensation and Tishchenko-esterification pathways (2-ethyl-2-hexenal and butyl butyrate). H-BEA also has selectivity for an oxygenated aromatic from ring-closure reaction of 2-ethyl-2-hexenal. In comparison, in a co-feed with n-butanal and isobutane, Zn-BEA after activation has the added presence of butenes with a lower selectivity for 2-ethyl-2-hexenal. The shift in selectivity from 90.9% to 76.3% of aldol condensation product upon adding isobutane to activated Zn-BEA suggests that isobutane acts as a H_2 source for hydro-deoxygenation of n-butanal. A deeper look

on the effects of Zn sites and co-fed isobutane can be found by operating in a higher temperature regime that promotes formation of products other than 2-ethyl-2-hexenal.

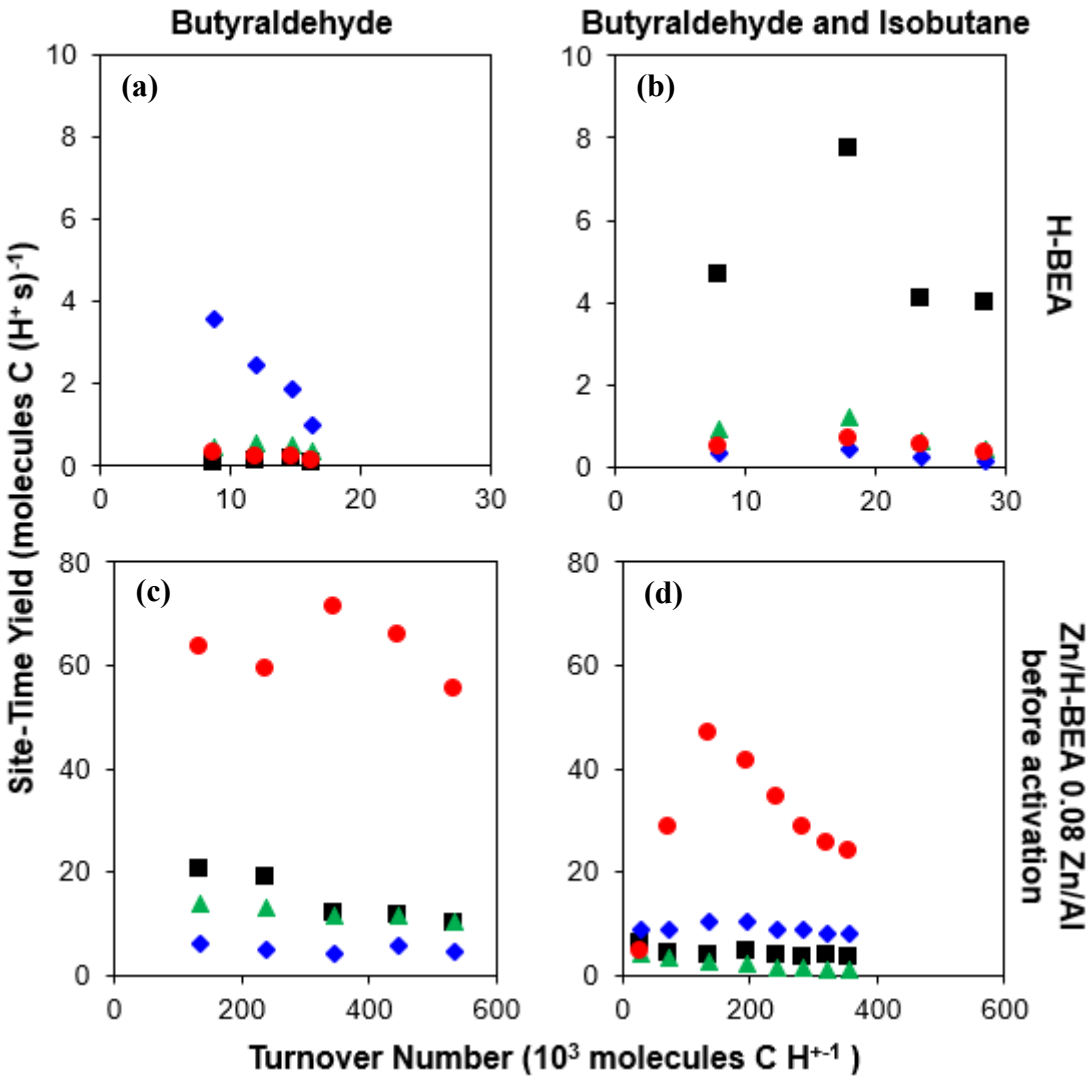

Figure 36. Site time yield (per accessible proton) of reaction pathway products (◆ aldol condensation, ■ deoxygenation, ▲ Tishchenko-esterification, and ● aromatics) at **523 K** as a function of turnover number on **(a)** H-BEA in 1.1 kPa butyraldehyde, **(b)** H-BEA in 1.1 kPa butyraldehyde and 50 kPa isobutane, **(c)** Zn-BEA 0.08 Zn/Al before activation in 1.1 kPa butyraldehyde, and **(d)** Zn-BEA 0.08 Zn/Al before activation in 1.1 kPa butyraldehyde and 50 kPa isobutane.

Figure 36 examines site-time yields of n-butanal and co-fed isobutane and n-butanal reactions on H-BEA and Zn-BEA before activation at 523 K. The overall STY for H-BEA in both feed conditions were significantly lower at 523 K than 473 K (1.5 vs 19.5 molecules C H^{+-1} s^{-1} for

n-butanal and 6.5 vs 15.4 molecules C H^{+-1} s^{-1} for co-fed isobutane and n-butanal) which is unexpected as operating at a higher temperature would lead to higher STY. Reactions at 523 K are not immediately apparent to be aldol condensation dominated as formation of arenes can be attributed to either Tishchenko-esterification or aldol condensation pathways. H-BEA in n-butanal **(a)** continues to have primarily aldol condensation product, 2-ethyl-2-hexenal. In comparison, Zn-BEA **(c)** had dramatically higher overall STY with significant aromatics, deoxygenation, and Tishchenko-esterification formation (63.4, 20.3, and 13.8 molecules C H^{+-1} s^{-1} respectively). The shift in pathway STY upon the addition of Zn to H-BEA indicates Zn sites are participating in acid-catalyzed reactions either directly as Lewis acid sites or indirectly in conjunction with neighboring Brønsted acid sites.

Addition of isobutane to a feed of n-butanal causes deoxygenation products to dominate on H-BEA **(b)**. However, lower formation for arenes, deoxygenation, and Tishchenko-esterification pathway products were observed on a reaction of isobutane to n-butanal on Zn-BEA **(d)**. The overall STY observed for each of the co-fed reaction pathways on Zn-BEA were still higher than that of H-BEA by a factor of 10. The decrease in arene formation upon addition of isobutane suggests that isobutane could be participating in the reaction as a hydrogen donor as ring-closing reactions to form arenes acts as a major source of molecular hydrogen. This would be evident with an increase in selectivity for paraffins and olefins when looking at the product selectivity breakdowns in a co-fed reaction.

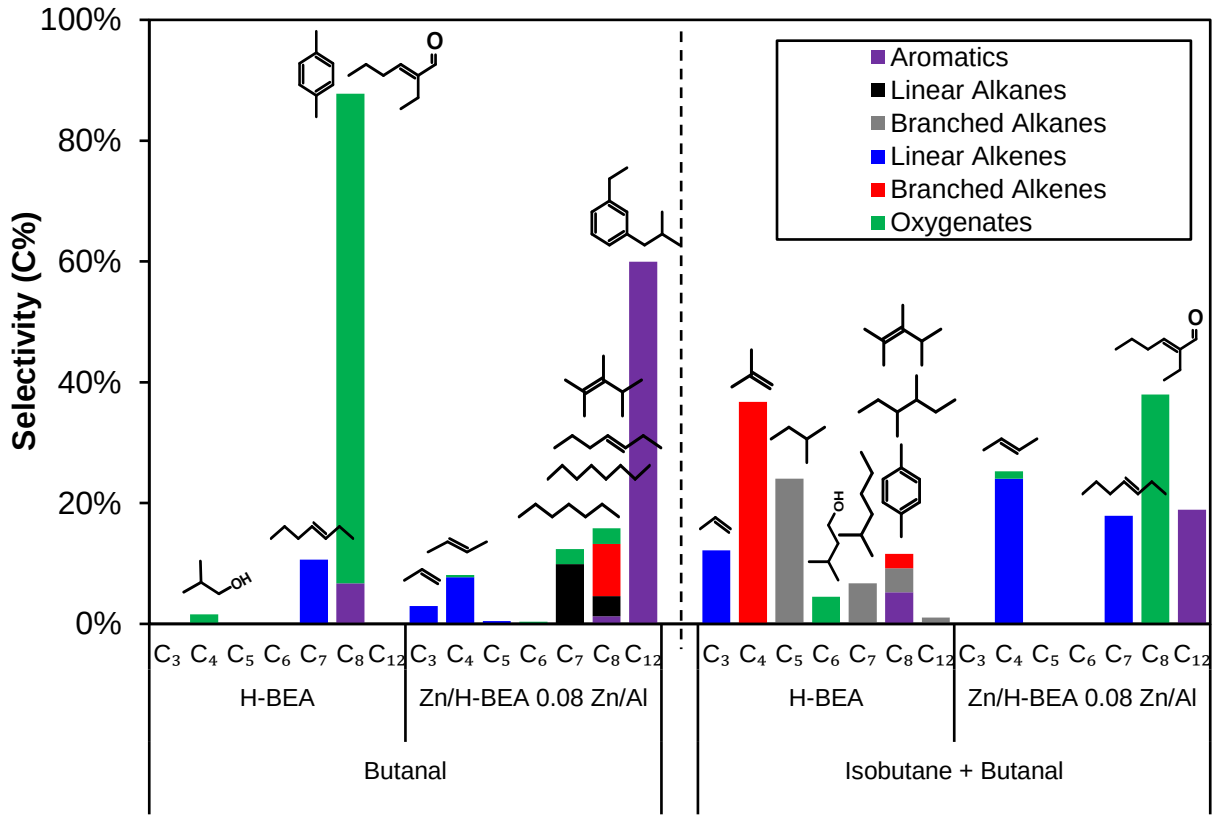

Figure 37. Selectivity (per carbon %) of classes of species (■ linear alkanes, ■ branched alkanes, ■ linear alkenes, ■ branched alkenes, ■ oxygenates, ■ aromatics) at 523 K on H-BEA and Zn-BEA 0.08 Zn/Al before activation in a feed of 1.1 kPa n-butanal (left) and 1.1 kPa n-butanal and 50 kPa isobutane (right).

Figure 37 shows the product selectivity for reactions of 1.1 kPa n-butanal and 1.1 kPa n-butanal and 50 kPa isobutane on H-BEA and Zn-BEA at 523 K. Comparisons at a similar turnover number was not possible because of the large differences in site-time yields between the two catalysts. Therefore, this product selectivity comparison occurs at similar time on stream. n-Butanal reactions on H-BEA predominantly forms 2-ethyl-2-hexenal and heptenes via aldol condensation. The lack of other pathway species in the product stream also suggests that the xylenes observed were formed via cyclization-deoxygenation of 2-ethyl-2-hexenal. In a co-fed n-butanal and isobutane, H-BEA shows selectivity for C_3 – C_4 olefins and C_5 paraffins through deoxygenation of n-butanal in addition to C_7 branched paraffins from deoxygenation of

Tishchenko-esterification-ketonization products. Each of these reactions require molecular hydrogen to occur and thus suggests that the unsaturated species formed from n-butanal conversion act as hydride abstracting agents in hydrogen transfer reactions from isobutane.

Selectivity for C_{12} arenes dominates the product distribution for Zn-BEA in a feed of n-butanal. Formation of arenes can be driven by a need for molecular hydrogen for the formation of C_3, C_4, C_7, and C_8 paraffin/olefins observed in addition to the arenes. These hydrocarbons are formed through the deoxygenation, Tishchenko-esterification, and aldol condensation reaction pathways and can be seen in the increased STY values for each of these pathways. Addition of isobutane to the feed causes Zn-BEA to shift selectivity towards C_4 and C_7 olefins along with 2-ethyl-2-hexenal and C_{12} aromatics. A concomitant decrease in selectivity for arenes with an increase in selectivity for olefins suggest that the isobutane acts as a hydrogen source for the hydro-deoxygenation of n-butanal and deoxygenation of Tishchenko-esterification ketones.

Chapter 6 Conclusion

This work focused on exploring the site identity of ion exchanged Zn sites in BEA zeolites and their role in the conversion of biomass-derived oxygenates. Careful preparation of ion exchanged Zn in BEA (Zn-BEA) allowed for the generation of different catalytic sites within the pores of the zeolite. Depending on the preparation method, Zn species have been suggested to exist as extra-pore large ZnO clusters, isolated Zn^{2+} ions at the cation-exchange site, $Zn(OH)^{+}$ ions exchanged to one aluminum sites, binuclear $[Zn\text{-}O\text{-}Zn]^{2+}$ clusters formed from the coupling of neighboring $Zn(OH)^{+}$ species, and Zn^{2+} exchanged to two aluminum sites.

XANES analysis of the Zn K-edge XAS spectra taken at SLAC provided information about the oxidation states and coordination sphere of Zn-BEA. The absorption edge energies in these catalysts were larger than that of the Zn standards, suggesting that the oxidation state of these Zn sites were higher than the +0 and +2 states of the reference samples. Spectra were also taken during the *in situ* temperature treatment of Zn-BEA in flowing He. During the temperature treatment, the features at the absorption edge changes drastically, splitting from a sharp single peak into two peaks. The lasting changes at the white line suggests that the coordination sphere of Zn sites changes significantly during this activation process. Analysis of the EXAFS region was conducted to examine the local structure of Zn in the catalysts. Fitting was carried out simultaneously through the samples, effectively constraining fits with shared parameters to allow for more reliable models. There was a lack of Zn-Zn and Zn-Si contributions in the first and second coordination shell, which indicates that Zn atoms were exchanged into isolated exchange positions without the formation of a significant amount of Zn clusters. *In situ* thermal treatment of Zn-BEA caused the number of oxygen neighbors to decrease in the first coordination shell. This supports the theory that as-prepared samples of Zn-BEA have water coordinated to Zn sites within the pores of the zeolite

and the temperature treatment process dehydrates the catalyst. There was a strong correlation between oxygen bond distance and Zn concentration, suggesting that Zn has an increasingly strong interaction with framework oxygen as the degree of ion exchange decreases. Changes in bond distance as more Zn is introduced to the pores can be explained shifts in the preferential ion exchange positions for Zn. As Zn replaces Brønsted acid sites during the ion exchange process, the lowest energy exchange locations may shift between the four-, five-, and six-member rings.

Brønsted and Lewis acid site density was measured by *in situ* titration during acid catalyzed isopropanol dehydration using probe molecules of pyridine and 2,6-di-*tert*-butylpyridine. By measuring the acid site densities, Zn-BEA has been shown to lose Brønsted acid sites during the temperature treatment process. Changes in the calculated Lewis acid site concentrations can suggest the presence of shifts in preferred site structures as Zn concentration increases. This catalyst characterization was combined with the activity of Zn-BEA for methanol dehydration to determine the reactivity of different Zn sites. The Lewis acidic Zn sites were shown to participate in the methanol dehydration reaction, however, the different sites formed by the Zn exchange process showed differences in reactivities. The conversion of butyraldehyde over a range of Zn loadings on Zn-BEA was also conducted to probe how the local structure of Zn sites influence the rates and selectivity of the various pathways in reactions of butyraldehyde.

In conclusion, the local structure and oxidation state of Zn in Zn-exchanged BEA was determined as well as quantification of the Bronsted and Lewis acid sites. The activity of these sites was probed through various oxygenate conversion reactions and showed that these Zn-exchanged catalysts and their role in oxygenate conversion cannot be predicted by just classic catalyst characterization techniques but requires more in-depth analysis on the structure of the available sites.

Chapter 7 Appendix

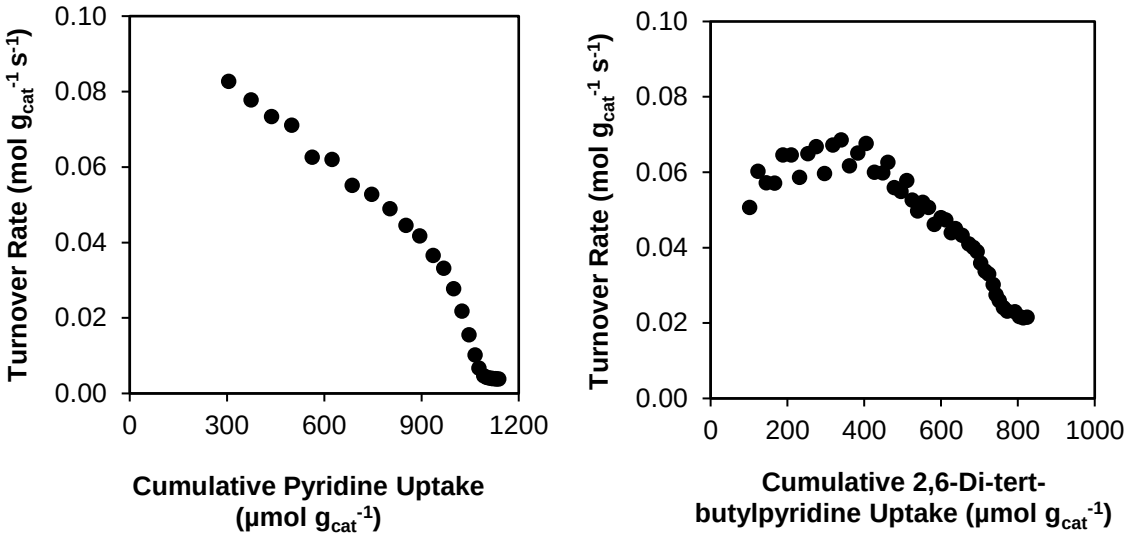

Figure 38. Turnover rate of isopropanol dehydration on H-BEA as a function of cumulative pyridine uptake (left) and cumulative 2,6-di-*tert*-butylpyridine uptake (right).

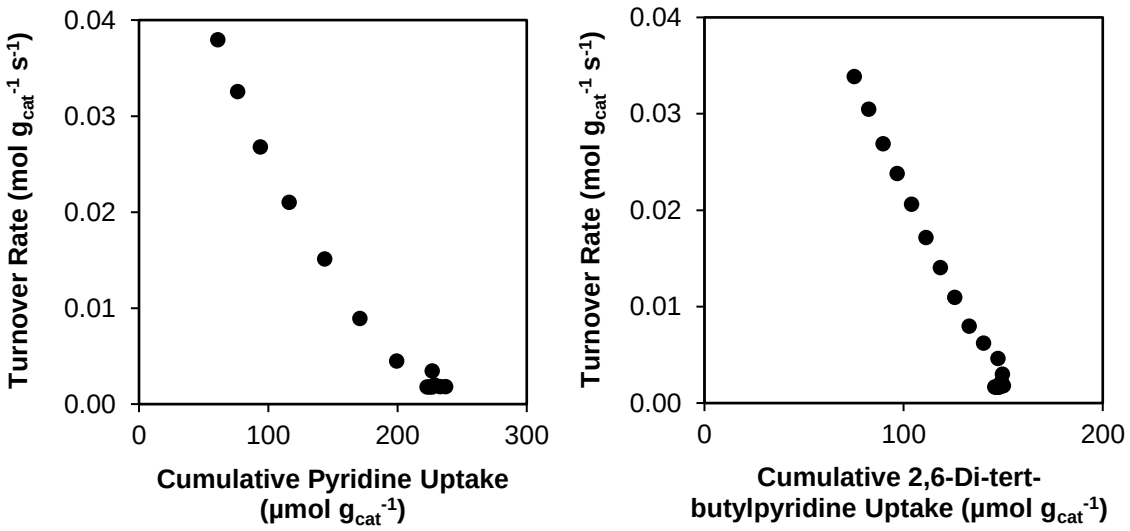

Figure 39. Turnover rate of isopropanol dehydration on Na-BEA-1 as a function of cumulative pyridine uptake (left) and cumulative 2,6-di-*tert*-butylpyridine uptake (right).

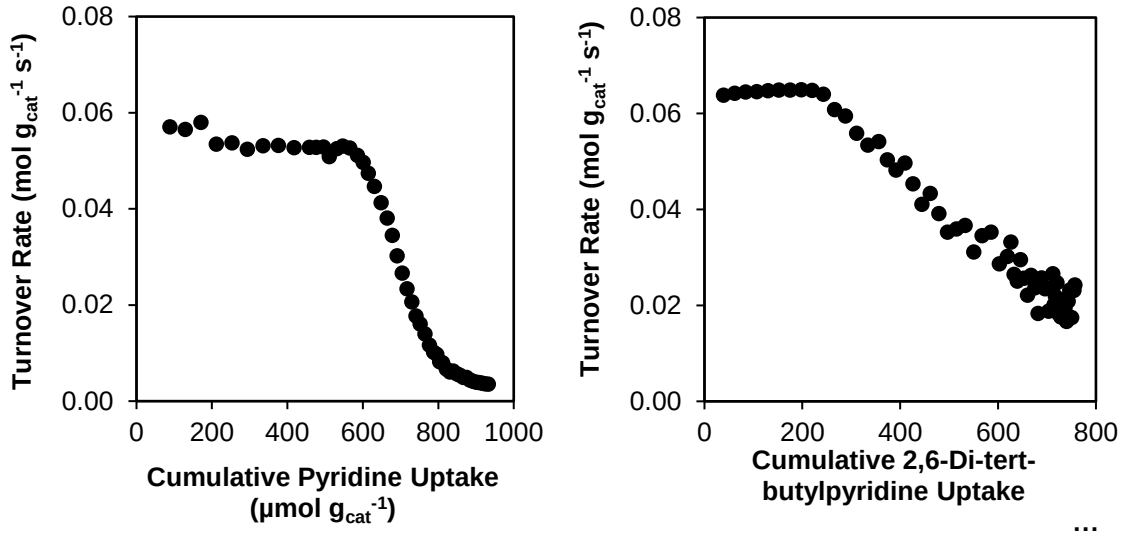

Figure 40. Turnover rate of isopropanol dehydration on Na-BEA-7 as a function of cumulative pyridine uptake (left) and cumulative 2,6-di-*tert*-butylpyridine uptake (right).

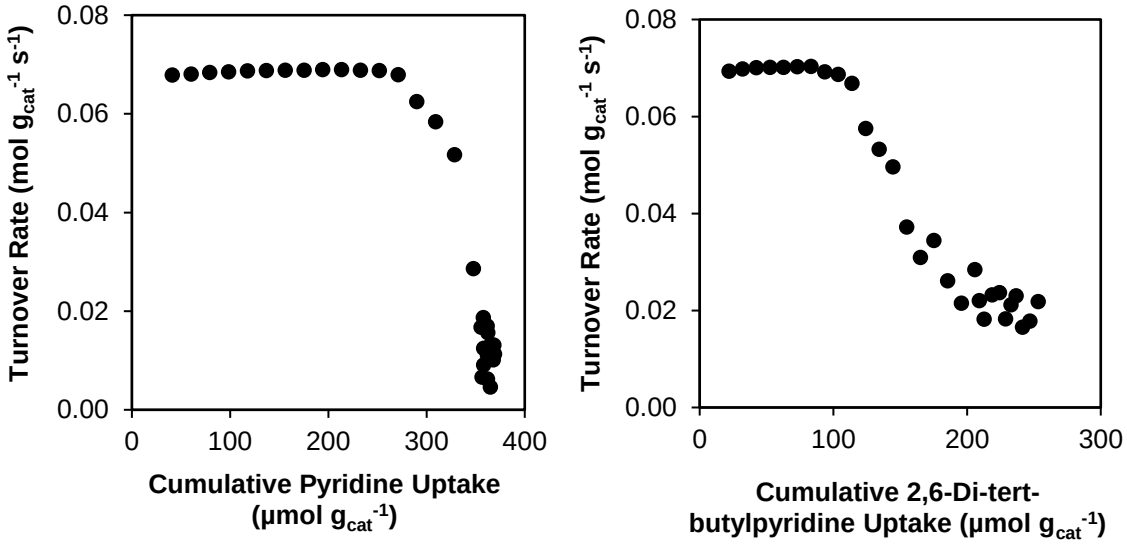

Figure 41. Turnover rate of isopropanol dehydration on Na-BEA-8 as a function of cumulative pyridine uptake (left) and cumulative 2,6-di-*tert*-butylpyridine uptake (right).

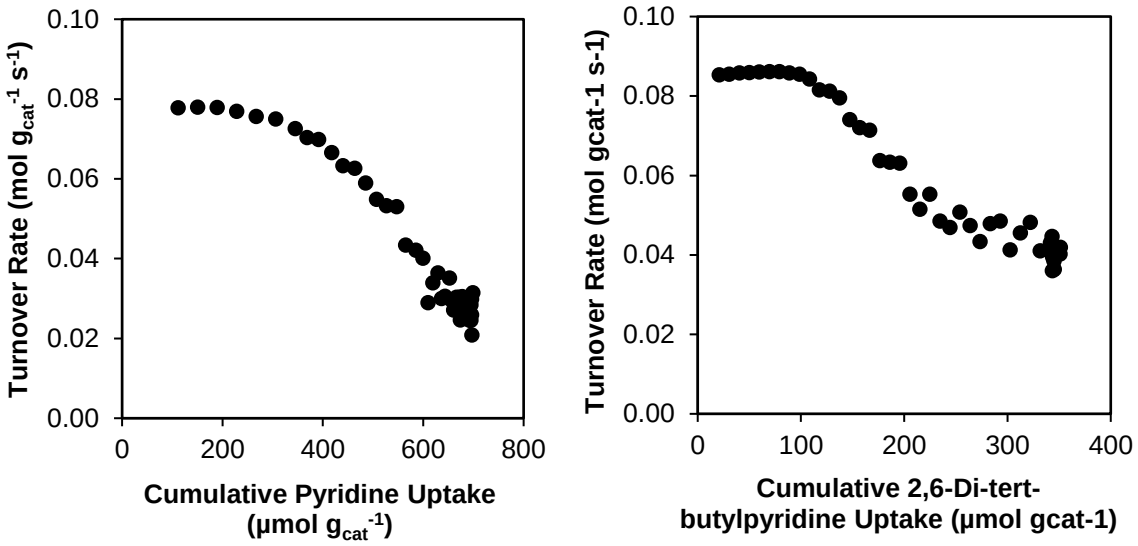

Figure 42. Turnover rate of isopropanol dehydration on Zn-BEA 0.03 Zn/Al before activation as a function of cumulative pyridine uptake (left) and cumulative 2,6-di-*tert*-butylpyridine uptake (right).

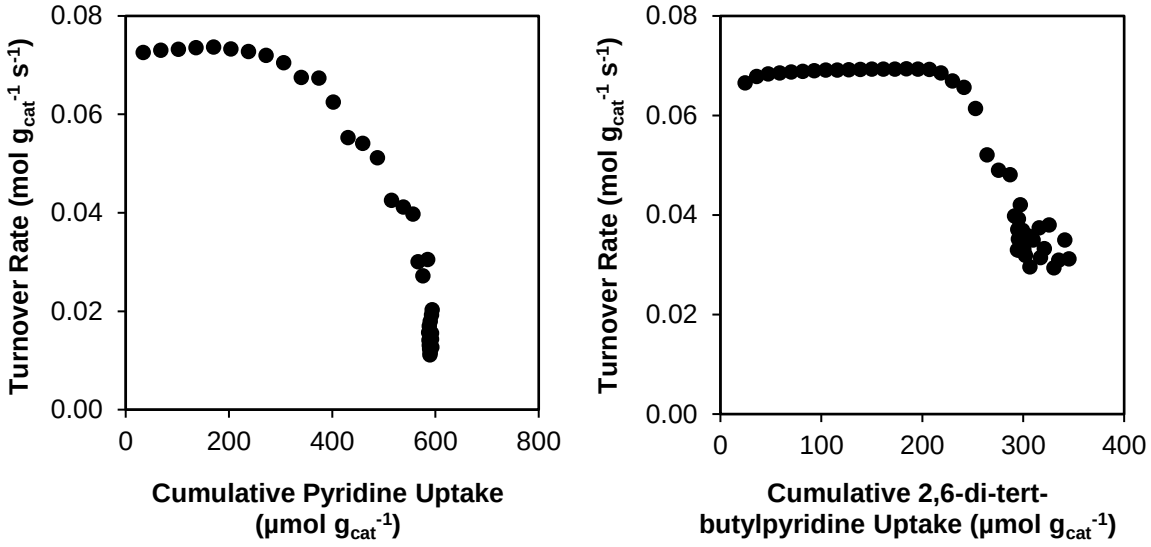

Figure 43. Turnover rate of isopropanol dehydration on Zn-BEA 0.03 Zn/Al after activation as a function of cumulative pyridine uptake (left) and cumulative 2,6-di-*tert*-butylpyridine uptake (right).

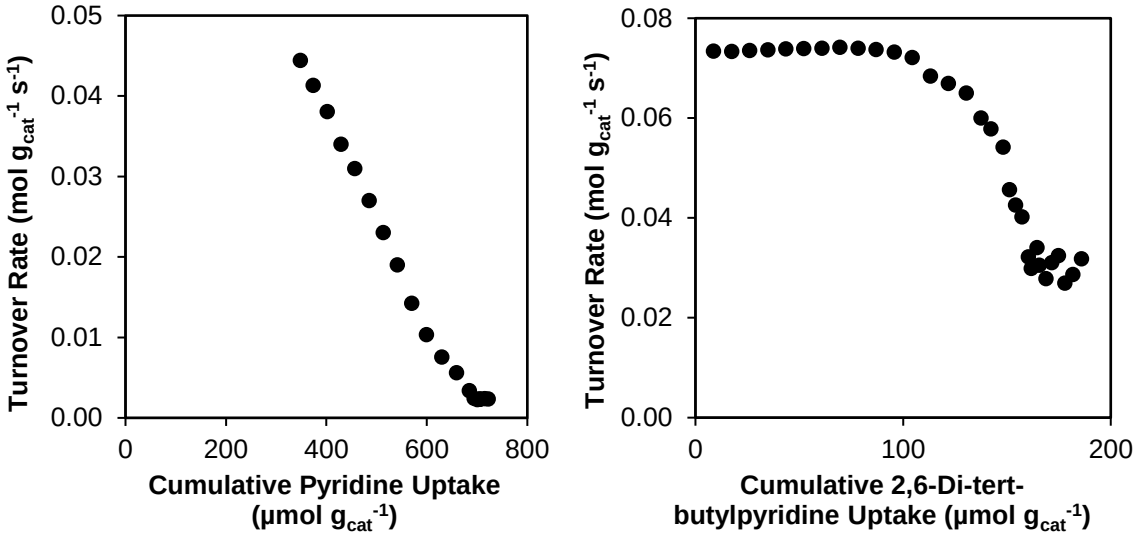

Figure 44. Turnover rate of isopropanol dehydration on Zn-BEA 0.04 Zn/Al before activation as a function of cumulative pyridine uptake (left) and cumulative 2,6-di-*tert*-butylpyridine uptake (right).

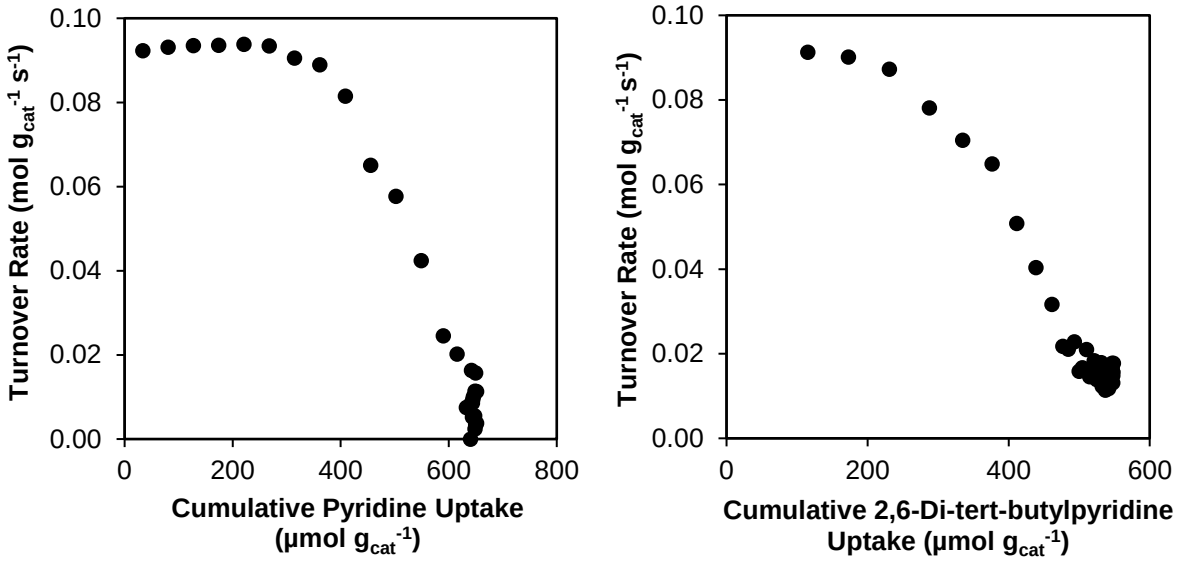

Figure 45. Turnover rate of isopropanol dehydration on Zn-BEA 0.04 Zn/Al after activation as a function of cumulative pyridine uptake (left) and cumulative 2,6-di-*tert*-butylpyridine uptake (right).

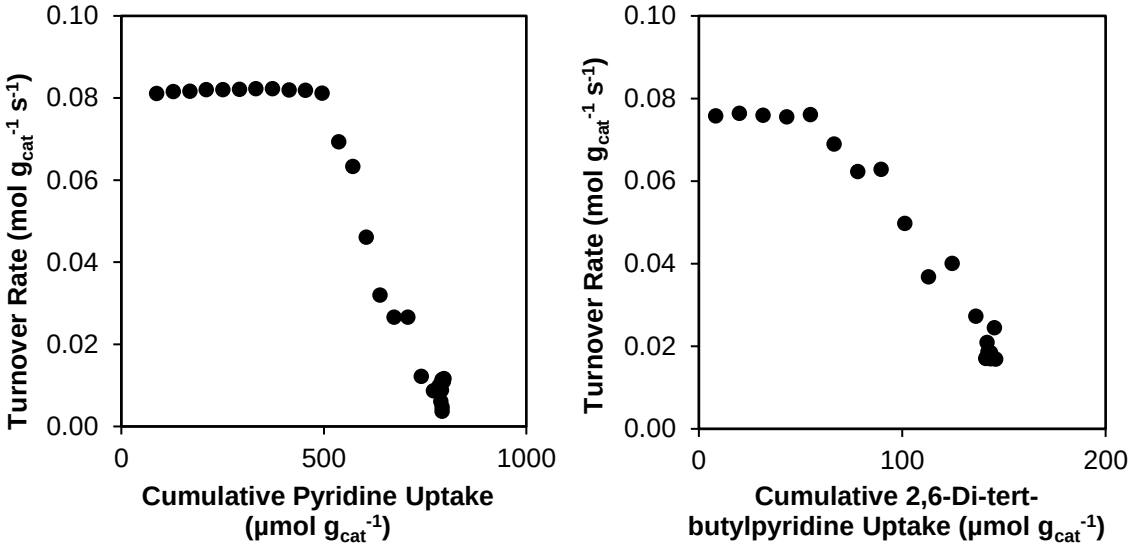

Figure 46. Turnover rate of isopropanol dehydration on Zn-BEA 0.21 Zn/Al before activation as a function of cumulative pyridine uptake (left) and cumulative 2,6-di-*tert*-butylpyridine uptake (right).

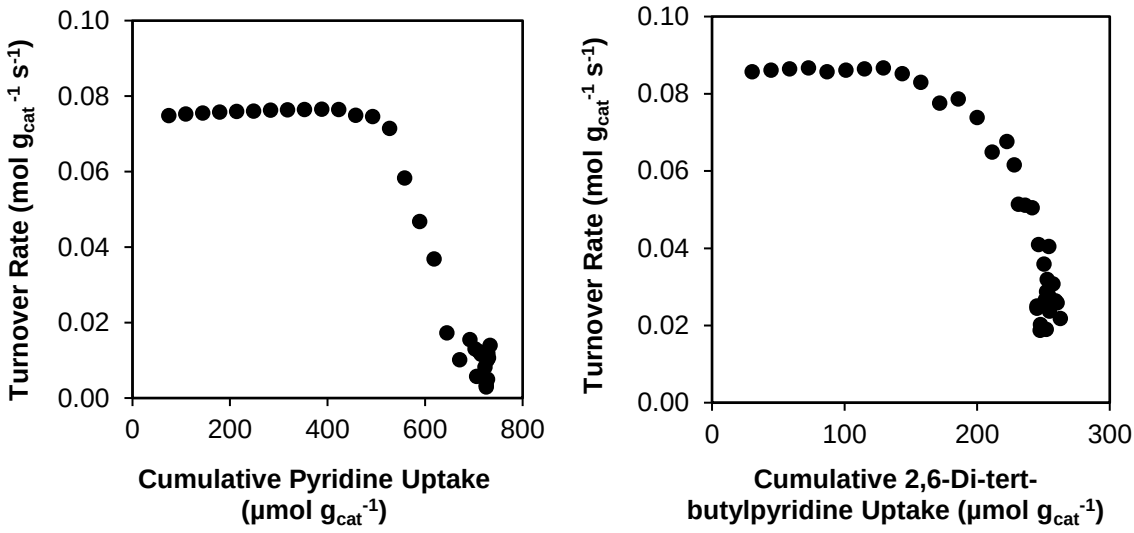

Figure 47. Turnover rate of isopropanol dehydration on 1 wt.% Zn-H-BEA IWI as a function of cumulative pyridine uptake (left) and cumulative 2,6-di-*tert*-butylpyridine uptake (right).

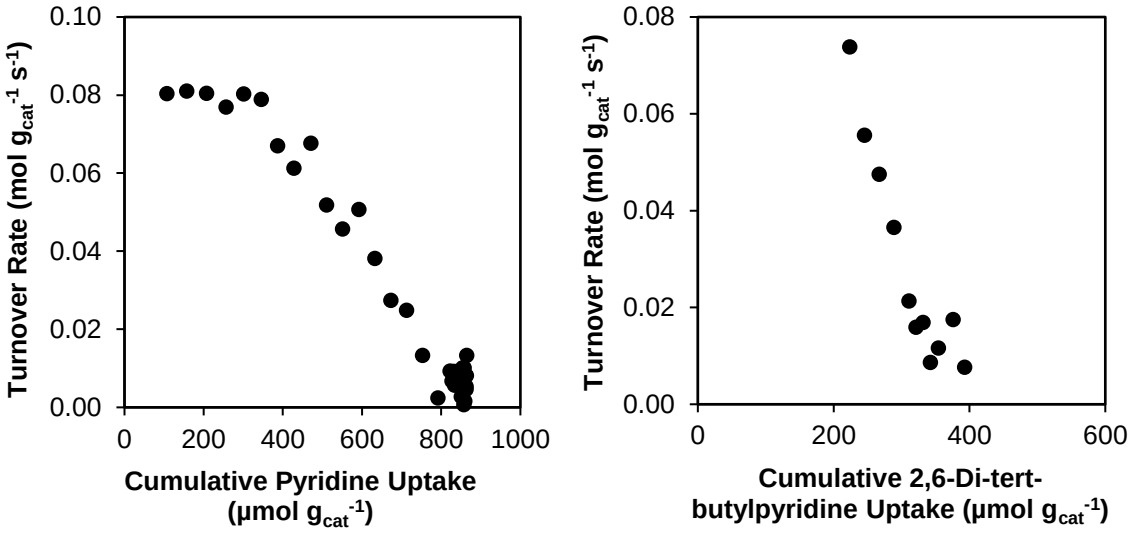

Figure 48. Turnover rate of isopropanol dehydration on 10 wt.% Zn-H-BEA IWI as a function of cumulative pyridine uptake (left) and cumulative 2,6-di-*tert*-butylpyridine uptake (right).

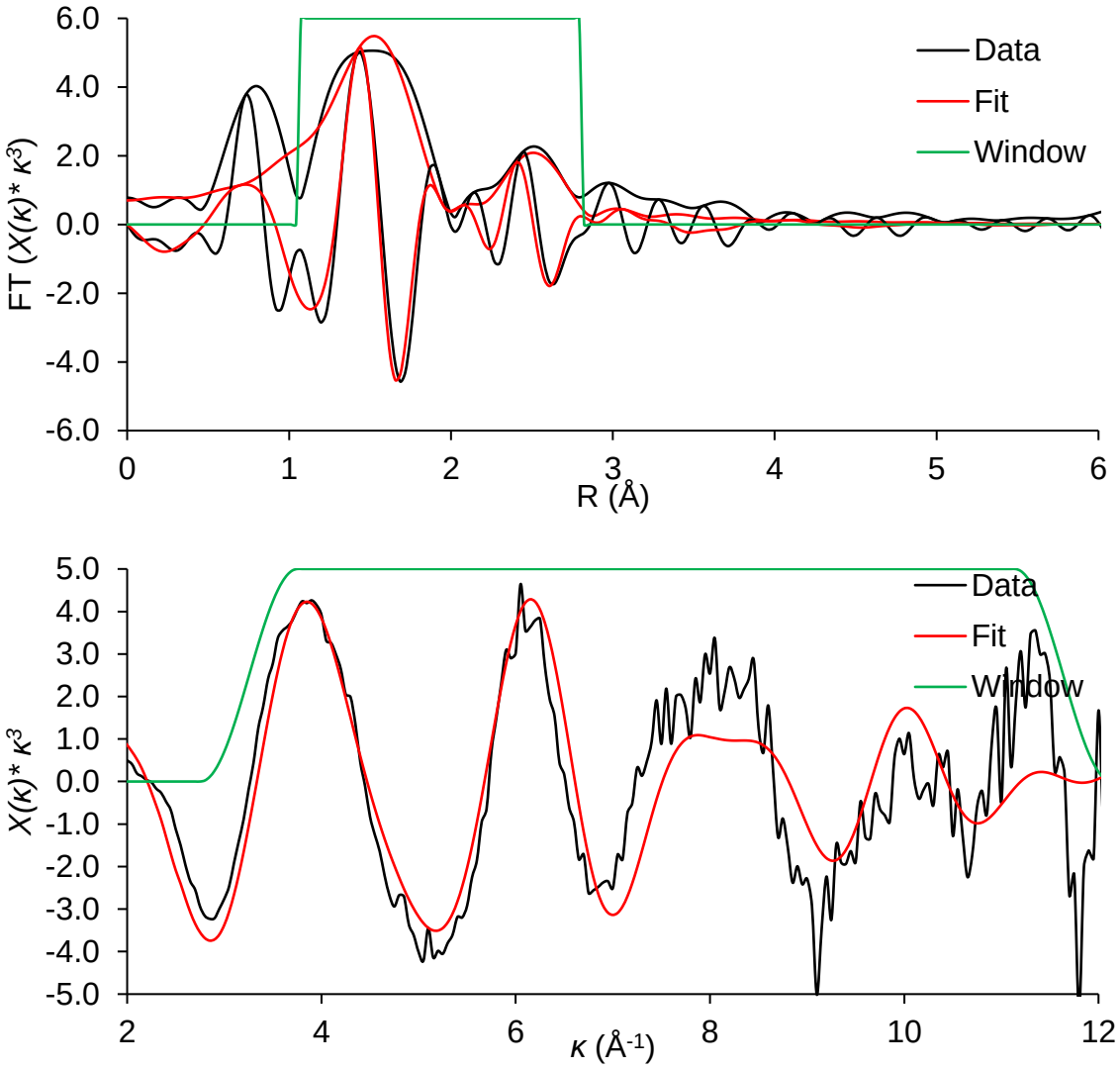

Figure 49. EXAFS data and best-fit model characterizing the 0.08Zn-BEA sample. Spectra were collected at room temperature in flowing helium. Top: k^3-weighted magnitude and imaginary part of the Fourier transform of the data (black line) and fit (red line). Bottom: k^3-weighted EXAFS function of the data (black line) and fit (red line). The green line in both plots represents the window used to determine the number of independent parameters.

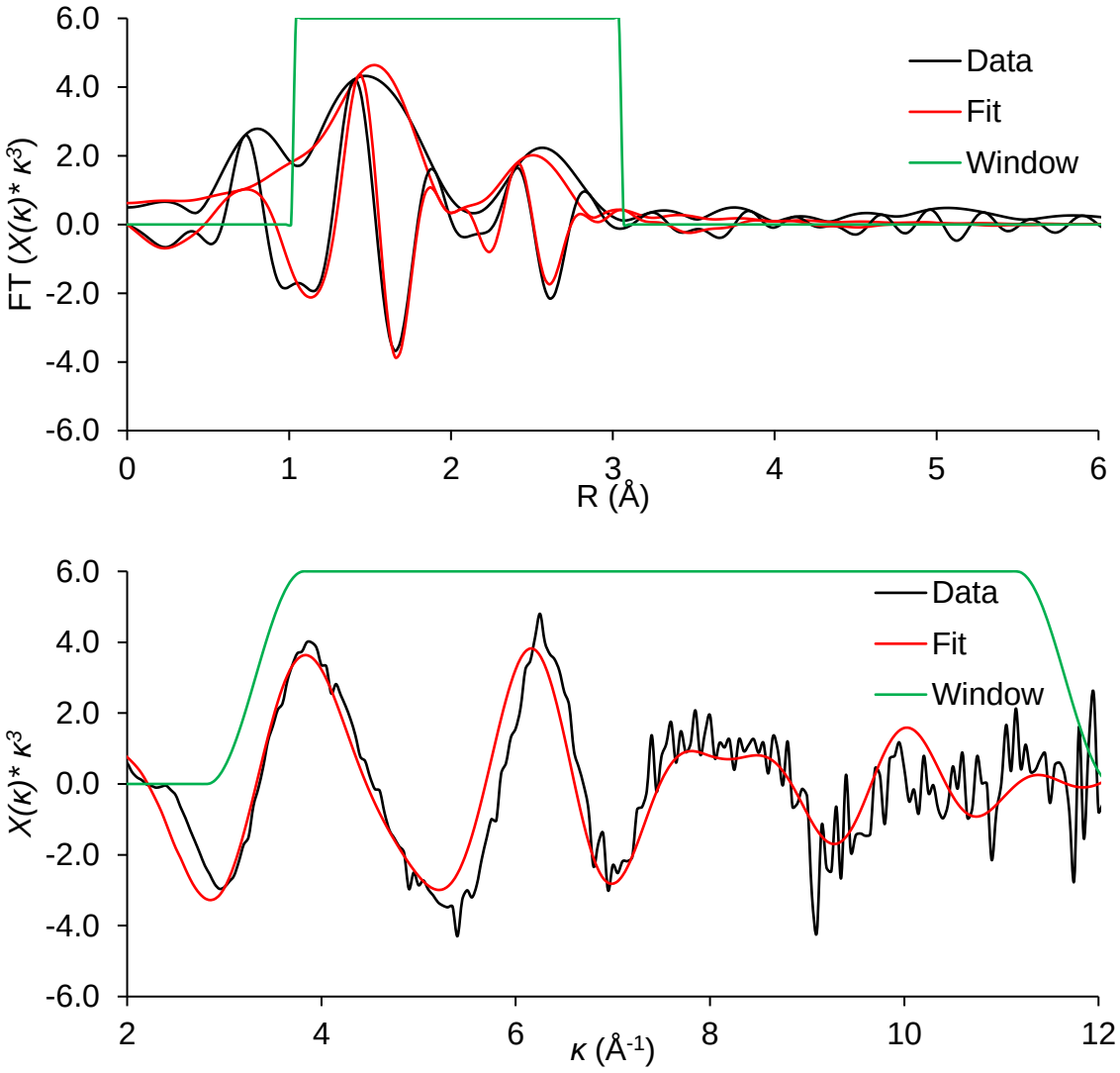

Figure 50. EXAFS data and best-fit model characterizing the 0.08Zn-BEA-pt sample. Spectra were collected at room temperature in flowing helium. Top: k^3-weighted magnitude and imaginary part of the Fourier transform of the data (black line) and fit (red line). Bottom: k^3-weighted EXAFS function of the data (black line) and fit (red line). The green line in both plots represents the window used to determine the number of independent parameters.

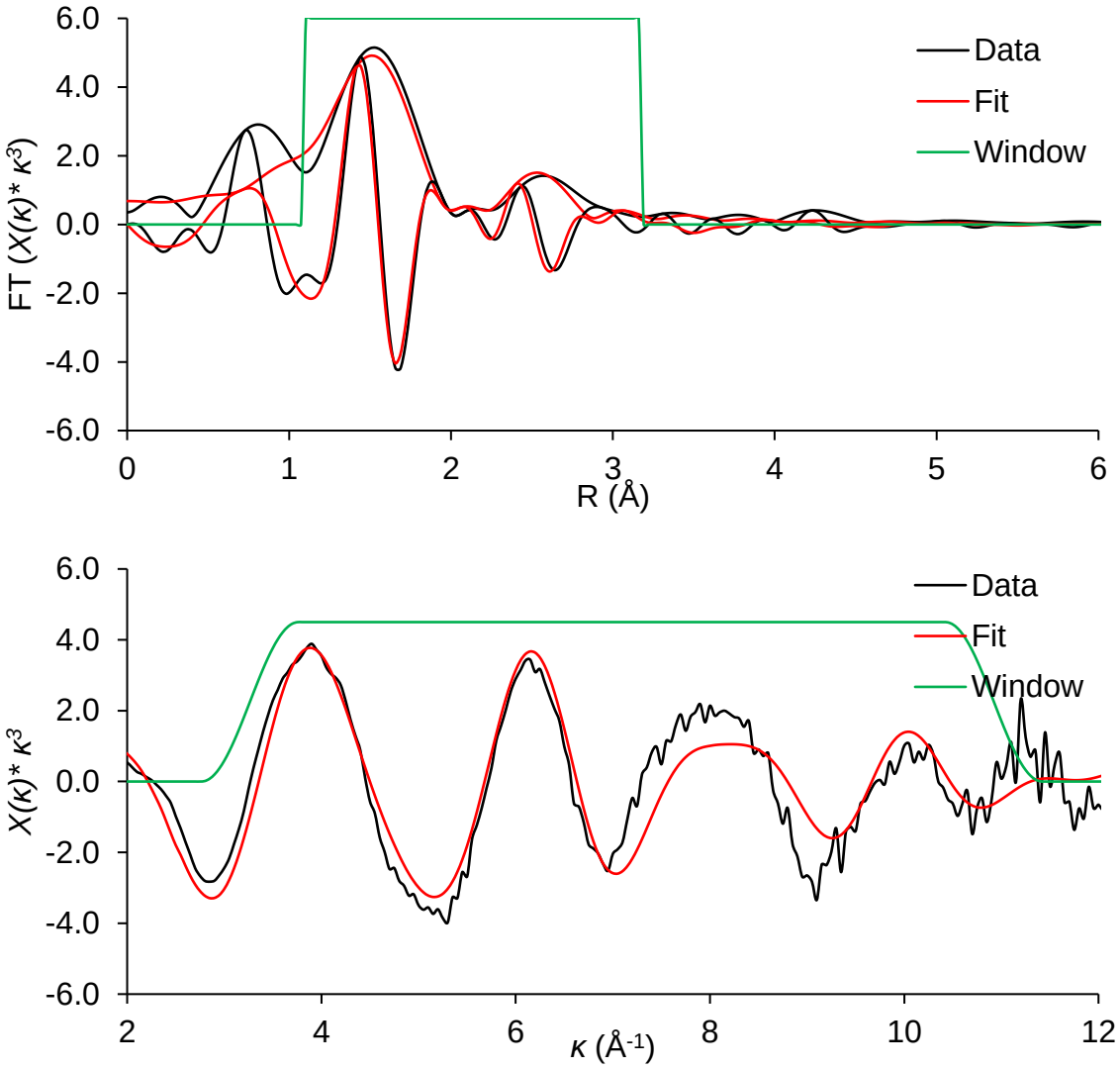

Figure 51. EXAFS data and best-fit model characterizing the 0.19Zn-BEA sample. Spectra were collected at room temperature in flowing helium. Top: k^3-weighted magnitude and imaginary part of the Fourier transform of the data (black line) and fit (red line). Bottom: k^3-weighted EXAFS function of the data (black line) and fit (red line). The green line in both plots represents the window used to determine the number of independent parameters.

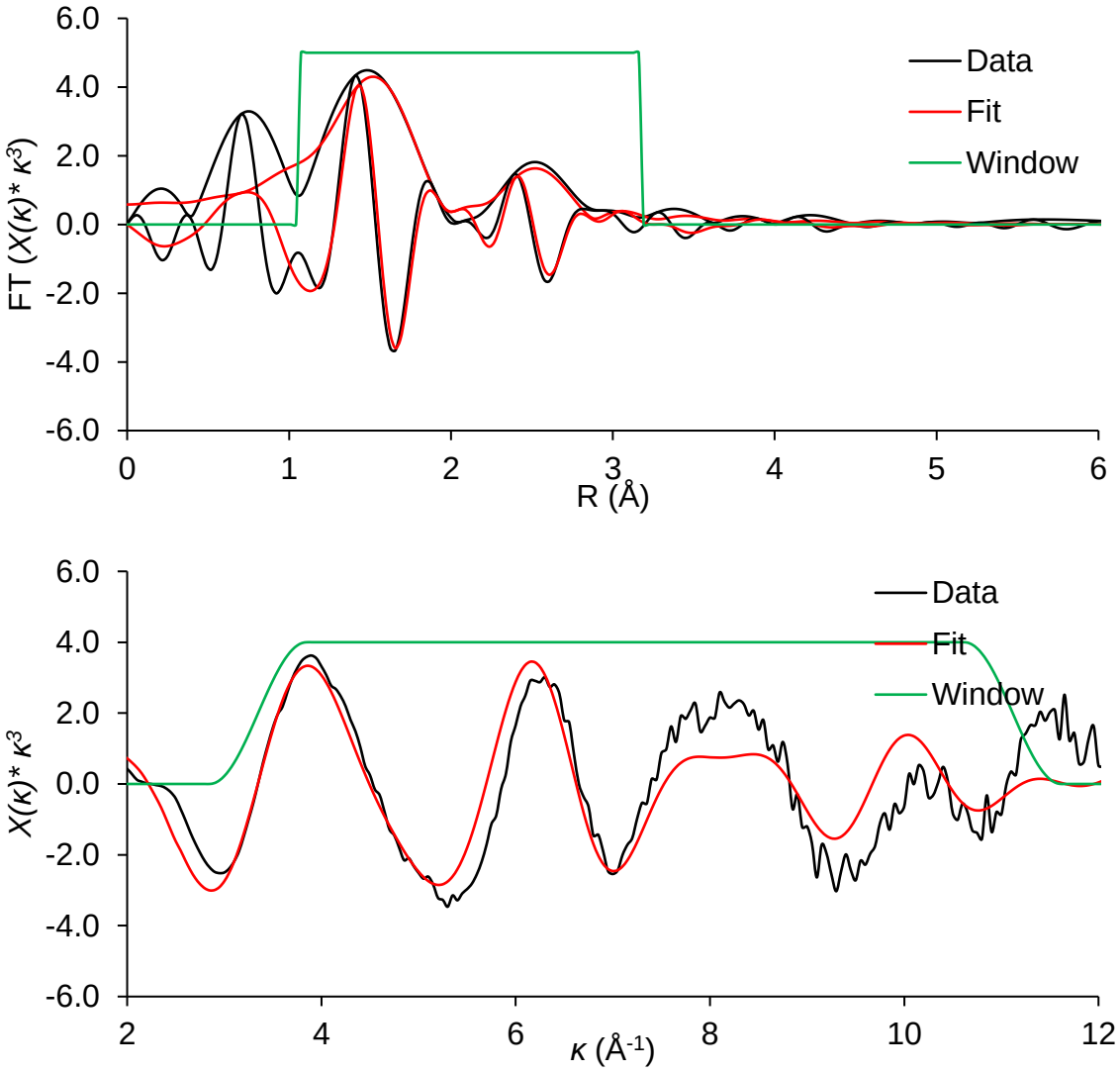

Figure 52. EXAFS data and best-fit model characterizing the 0.19Zn-BEA-pt sample. Spectra were collected at room temperature in flowing helium. Top: k^3-weighted magnitude and imaginary part of the Fourier transform of the data (black line) and fit (red line). Bottom: k^3-weighted EXAFS function of the data (black line) and fit (red line). The green line in both plots represents the window used to determine the number of independent parameters.

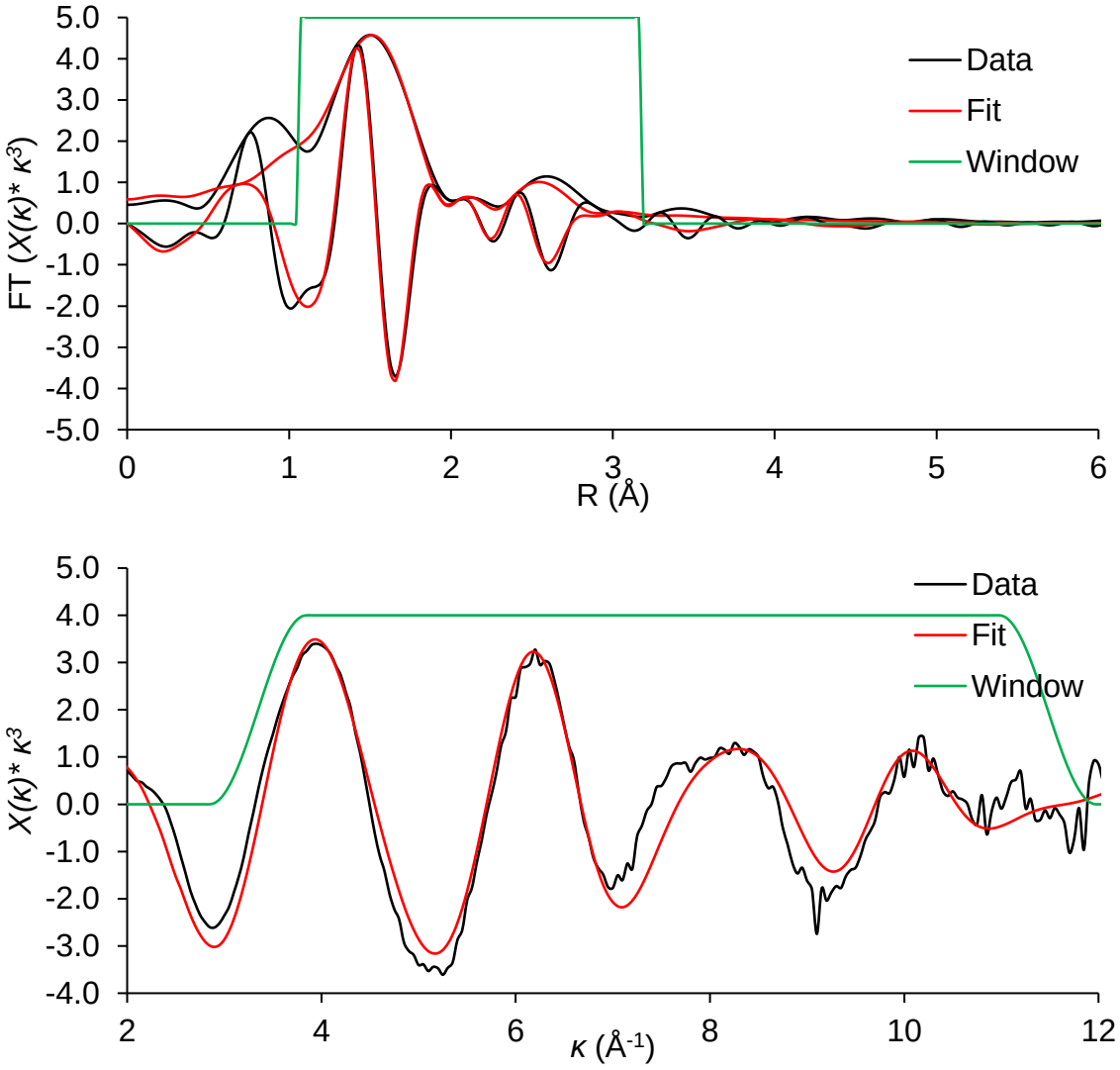

Figure 53. EXAFS data and best-fit model characterizing the 0.21Zn-BEA sample. Spectra were collected at room temperature in flowing helium. Top: k^3-weighted magnitude and imaginary part of the Fourier transform of the data (black line) and fit (red line). Bottom: k^3-weighted EXAFS function of the data (black line) and fit (red line). The green line in both plots represents the window used to determine the number of independent parameters.

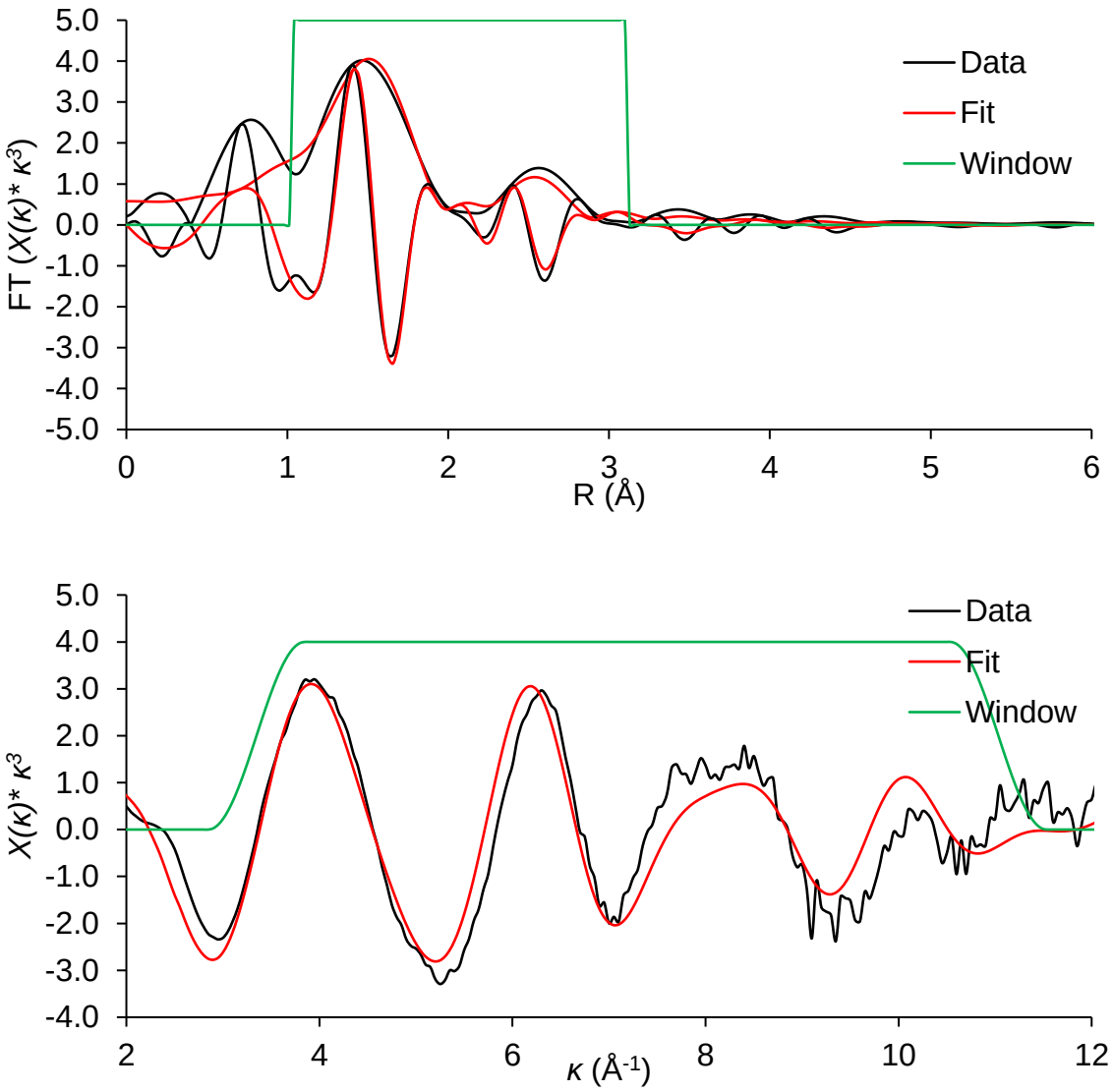

Figure 54. EXAFS data and best-fit model characterizing the 0.21Zn-BEA-pt sample. Spectra were collected at room temperature in flowing helium. Top: k^3-weighted magnitude and imaginary part of the Fourier transform of the data (black line) and fit (red line). Bottom: k^3-weighted EXAFS function of the data (black line) and fit (red line). The green line in both plots represents the window used to determine the number of independent parameters.

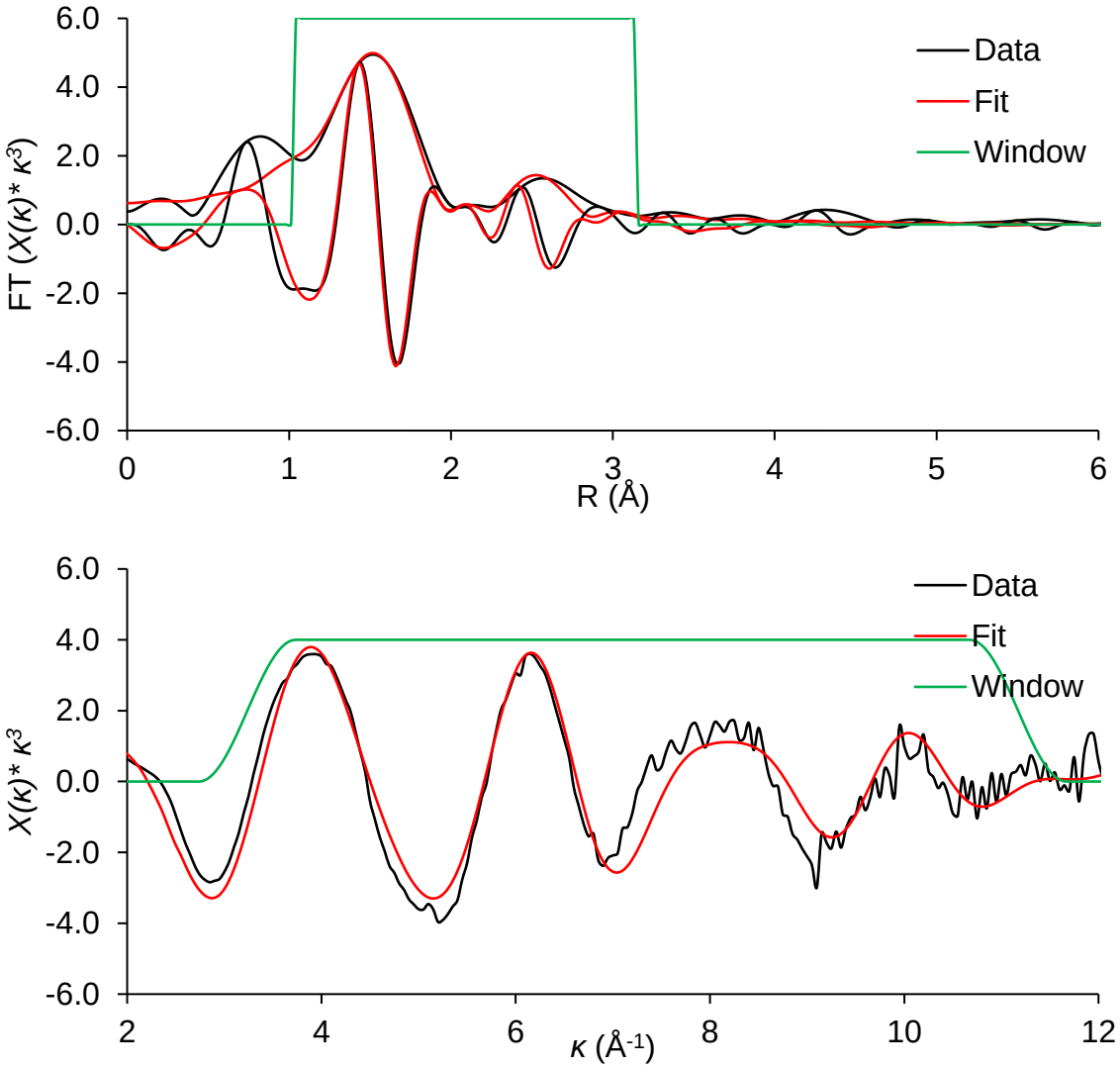

Figure 55. EXAFS data and best-fit model characterizing the 0.35Zn-BEA sample. Spectra were collected at room temperature in flowing helium. Top: k^3-weighted magnitude and imaginary part of the Fourier transform of the data (black line) and fit (red line). Bottom: k^3-weighted EXAFS function of the data (black line) and fit (red line). The green line in both plots represents the window used to determine the number of independent parameters.

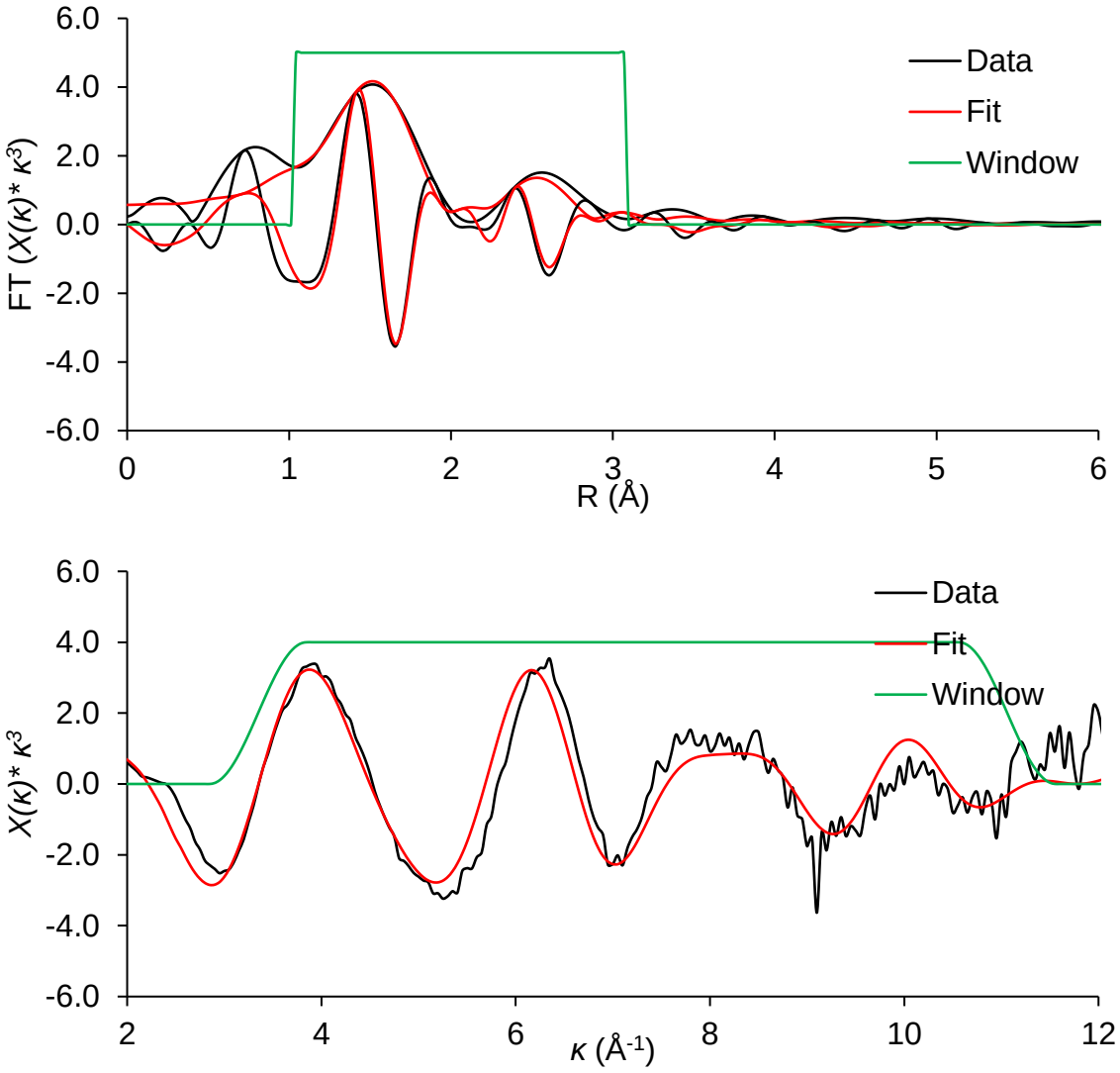

Figure 56. EXAFS data and best-fit model characterizing the 0.35Zn-BEA-pt sample. Spectra were collected at room temperature in flowing helium. Top: k^3-weighted magnitude and imaginary part of the Fourier transform of the data (black line) and fit (red line). Bottom: k^3-weighted EXAFS function of the data (black line) and fit (red line). The green line in both plots represents the window used to determine the number of independent parameters.

Table 4. Summary of the EXAFS fit parameters characterizing the Zn-BEA samples.

Sample	Absorber-Backscatter Scattering Path	ΔE_0 (eV)	R (Å)	N	σ^2 (10^{-3}Å^2)	K range (Å^{-1})	R range (Å)
Metallic Zn Foil	Zn-Zn	-0.1 ± 1.1	2.63 ± 0.01	6	11.4 ± 0.8	2.92 – 12.13	1.39 – 3.15
	Zn-Zn	-0.1 ± 1.1	3.01 ± 0.05	6	3.4 ± 7.6		
0.08Zn-BEA	Zn-O	-0.9 ± 0.8	1.97 ± 0.01	4.1 ± 0.5	9.3 ± 0.9	3.26 – 11.64	1.05 – 2.82
	Zn-Al	3.9 ± 2.2	2.83 ± 0.02	1.0 ± 0.5	4.2 ± 2.7		
0.08Zn-BEA-pt	Zn-O	-0.9 ± 0.8	1.98 ± 0.01	3.5 ± 0.5	9.3 ± 0.9	3.32 – 11.66	1.02 – 3.07
	Zn-Al	3.9 ± 2.2	2.83 ± 0.02	1.0 ± 0.5	4.2 ± 2.7		
0.19Zn-BEA	Zn-O	-0.9 ± 0.8	1.97 ± 0.01	3.7 ± 0.3	9.3 ± 0.9	3.26 – 10.92	1.08 – 3.16
	Zn-Al	3.9 ± 2.2	2.83 ± 0.02	0.7 ± 0.2	4.2 ± 2.7		
0.19Zn-BEA-pt	Zn-O	-0.9 ± 0.8	1.96 ± 0.01	3.3 ± 0.3	9.3 ± 0.9	3.35 – 11.12	1.05 – 3.16
	Zn-Al	3.9 ± 2.2	2.83 ± 0.02	0.8 ± 0.3	4.2 ± 2.7		
0.21Zn-BEA	Zn-O	-0.9 ± 0.8	1.96 ± 0.01	3.4 ± 0.2	9.3 ± 0.9	3.35 – 11.48	1.07 – 3.17
	Zn-Al	3.9 ± 2.2	2.83 ± 0.02	0.4 ± 0.2	4.2 ± 2.7		
0.21Zn-BEA-pt	Zn-O	-0.9 ± 0.8	1.96 ± 0.01	3.0 ± 0.2	9.3 ± 0.9	3.35 – 11.03	1.04 – 3.12
	Zn-Al	3.9 ± 2.2	2.83 ± 0.02	0.5 ± 0.2	4.2 ± 2.7		
0.35Zn-BEA	Zn-O	-0.9 ± 0.8	1.97 ± 0.01	3.7 ± 0.3	9.3 ± 0.9	3.24 – 11.17	1.04 – 3.14
	Zn-Al	3.9 ± 2.2	2.83 ± 0.02	0.6 ± 0.2	4.2 ± 2.7		
0.35Zn-BEA-pt	Zn-O	-0.9 ± 0.8	1.97 ± 0.01	3.2 ± 0.3	9.3 ± 0.9	3.35 – 11.06	1.04 – 3.09
	Zn-Al	3.9 ± 2.2	2.83 ± 0.02	0.6 ± 0.3	4.2 ± 2.7		

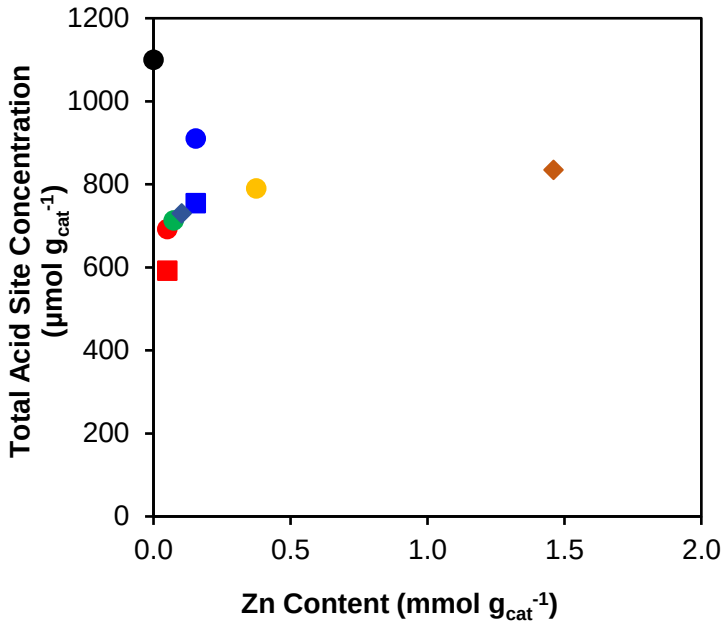

Figure 57. Total acid site concentration of H-BEA (●), Zn-BEA 0.03 Zn/Al before activation (●), Zn-BEA 0.03 Zn/Al after activation (■), Zn-BEA 0.04 Zn/Al before activation (●), Zn-BEA 0.08 Zn/Al before activation (●), Zn-BEA 0.08 Zn/Al after activation (■), Zn-BEA 0.21 Zn/Al before activation (●), Zn-H-BEA 1 wt.% IWI (◆), and Zn-H-BEA 10 wt.% IWI (◆) as a function of Zn content.

Chapter 8 References

1. Energy Information Administration. International Energy Outlook. *Outlook* **0484**, 70–99 (2019).

2. Stern, D. I. Energy and economic growth in the USA. A multivariate approach. *Energy Economics* **15**, 137–150 (1993).

3. Stern, D. I. The role of energy in economic growth. *Annals of the New York Academy of Sciences* **1219**, 26–51 (2011).

4. U.S. Energy Information Agency. *October 2019 Monthly Energy Review*. vol. 0035 (2019).

5. Cox, P. M., Betts, R. A., Jones, C. D., Spall, S. A. & Totterdell, I. J. Acceleration of global warming due to carbon-cycle feedbacks in a coupled climate model. *Nature* **408**, 184–187 (2000).

6. U.S. Environmental Protection Agency (EPA). Fast Facts from the Inventory of U.S. Greenhouse Gas Emissions and Sinks: 1990–2014. 3 (2016).

7. Meinshausen, M. *et al*. Greenhouse-gas emission targets for limiting global warming to 2°C. *Nature* **458**, 1158–1162 (2009).

8. Material, S. O., York, N. & Nw, A. Change and Ocean Acidification. *Science (1979)* **1737**, 1737–1743 (2007).

9. Bonan, G. B. Forests and climate change: Forcings, feedbacks, and the climate benefits of forests. *Science (1979)* **320**, 1444–1449 (2008).

10. Davidson, E. A. & Janssens, I. A. Temperature sensitivity of soil carbon decomposition and feedbacks to climate change. *Nature* **440**, 165–173 (2006).

11. U.S. Energy Information Agency. Annual Energy Outlook 2019 with projections to 2050. *Annual Energy Outlook 2019 with projections to 2050* **44**, 1–64 (2019).

12. Vora, B. V. *et al.* Economic route for natural gas conversion to ethylene and propylene. in *Studies in Surface Science and Catalysis* (eds. de Pontes, M., Espinoza, R. L., Nicolaides, C. P., Scholtz, J. H. & Scurrell, M. S. B. T.-S. in S. S. and C.) vol. 107 87–98 (Elsevier, 1997).

13. Chen, J. Q., Bozzano, A., Glover, B., Fuglerud, T. & Kvisle, S. Recent advancements in ethylene and propylene production using the UOP/Hydro MTO process. *Catalysis Today* **106**, 103–107 (2005).

14. Huber, G. W., Iborra, S. & Corma, A. Synthesis of transportation fuels from biomass: Chemistry, catalysts, and engineering. *Chemical Reviews* **106**, 4044–4098 (2006).

15. Schwartz, T. J., Shanks, B. H. & Dumesic, J. A. Coupling chemical and biological catalysis: A flexible paradigm for producing biobased chemicals. *Current Opinion in Biotechnology* **38**, 54–62 (2016).

16. Chang, C. D. & Silvestri, A. J. The Conversion of Methanol and other O-compounds over Zeolite Catalysts. *Journal of Catalysis* **47**, 249–259 (1977).

17. Simonetti, D. A. & Dumesic, J. A. Catalytic strategies for changing the energy content and achieving C-C coupling in biomass-derived oxygenated hydrocarbons. *ChemSusChem* **1**, 725–733 (2008).

18. Bedard, J., Hong, D. Y. & Bhan, A. Co-processing CH4 and oxygenates on Mo/H-ZSM-5: 2. CH 4-CO2 and CH4-HCOOH mixtures. *Physical Chemistry Chemical Physics* **15**, 12173–12179 (2013).

19. Gao, J. *et al.* Identification of molybdenum oxide nanostructures on zeolites for natural gas conversion. *Science (1979)* **348**, 686–690 (2015).

20. Gorte, R. J. What do we know about the acidity of solid acids? *Catalysis Letters* **62**, 1–13 (1999).

21. Corma, A. & García, H. Organic reactions catalyzed over solid acids. *Catalysis Today* **38**, 257–308 (1997).

22. Corma, A. Inorganic Solid Acids and Their Use in Acid-Catalyzed Hydrocarbon Reactions. *Chemical Reviews* **95**, 559–614 (1995).

23. Corma, A. & Martínez, A. Chemistry, catalysts, and processes for isoparaffin-olefin alkylation: Actual situation and future trends. *Catalysis Reviews* **35**, 483–570 (1993).

24. Haw, J. F., Richardson, B. R., Oshiro, I. S., Lazo, N. D. & Speed, J. A. Reactions of Propene on Zeolite HY Catalyst Studied by in Situ Variable-Temperature Solid-State Nuclear Magnetic Resonance Spectroscopy. *J Am Chem Soc* **111**, 2052–2058 (1989).

25. Derouane, E. G., He, H., Hamid, S. B. D. A. & Ivanova, I. I. In situ MAS NMR investigations of molecular sieves and zeolite-catalyzed reactions. *Catalysis Letters* **58**, 1–19 (1999).

26. Janik, M. J., Davis, R. J. & Neurock, M. A quantum chemical study of tertiary carbenium ions in acid catalyzed hydrocarbon conversions over phosphotungstic acid. *Catalysis Today* **116**, 90–98 (2006).

27. Frash, M. V. & Van Santen, R. A. Quantum-chemical modeling of the hydrocarbon transformations in acid zeolite catalysts. *Topics in Catalysis* **9**, 191–205 (1999).

28. Rigby, A. M., Kramer, G. J. & Van Santen, R. A. Mechanisms of hydrocarbon conversion in zeolites: A quantum mechanical study. *Journal of Catalysis* **170**, 1–10 (1997).

29. Natal-Santiago, M. A., Alcalá, R. & Dumesic, J. A. DFT study of the isomerization of hexyl species involved in the acid-catalyzed conversion of 2-methyl-pentene-2. *Journal of Catalysis* **181**, 124–144 (1999).

30. Penzien, J. *et al.* Generation and Characterization of Well-Defined Zn^{2+} Lewis Acid Sites in Ion Exchanged Zeolite BEA. *The Journal of Physical Chemistry B* **108**, 4116–4126 (2004).

31. Buchanan, J. S., Santiesteban, J. G. & Haag, W. O. Mechanistic considerations in acid-catalyzed cracking of olefins. *Journal of Catalysis* **158**, 279–287 (1996).

32. Jentoft, F. & Gates, B. C. Solid-acid-catalyzed alkane cracking mechanisms: evidence from reactions of small probe molecules. **4**, 1–13 (1997).

33. Krannila, H., Haag, W. O. & Gates, B. C. Monomolecular and bimolecular mechanisms of paraffin cracking: n-butane cracking catalyzed by HZSM-5. *Journal of Catalysis* **135**, 115–124 (1992).

34. Lercher, J. A., van Santen, R. A. & Vinek, H. Carbonium ion formation in zeolite catalysis. *Catalysis Letters* **27**, 91–96 (1994).

35. Valdés, M. G., Pérez-Cordoves, A. I. & Díaz-García, M. E. Zeolites and zeolite-based materials in analytical chemistry. *TrAC - Trends in Analytical Chemistry* **25**, 24–30 (2006).

36. Lawton, J. A., Lawton, S. L., Leonowicz, M. E. & Rubin, M. K. The framework topology of zeolite MCM-22. *Studies in Surface Science and Catalysis* **98**, 250–251 (1995).

37. Armbruster, T. & Gunter, M. E. Crystal structures of natural zeolites. *Reviews in Mineralogy and Geochemistry* **45**, 1–67 (2001).

38. Rhodes, C. J. Properties and applications of zeolites. *Science Progress* **93**, 223–284 (2010).

39. Yilmaz, B. & Müller, U. Catalytic applications of zeolites in chemical industry. *Topics in Catalysis* **52**, 888–895 (2009).

40. Moshoeshoe, M., Nadiye-Tabbiruka, M. S. & Obuseng, V. A review of the Chemistry, Structure, Properties and Applications of Zeolites. *American journal of Materials Science* **7**, 191–221 (2017).

41. Denayer, J. F., Souverijns, W., Jacobs, P. A., Martens, J. A. & Baron, G. V. High-temperature low-pressure adsorption of branched C5-C8 alkanes on zeolite beta, ZSM-5, ZSM-22, zeolite Y, and mordenite. *Journal of Physical Chemistry B* **102**, 4588–4597 (1998).

42. Stückenschneider, K., Merz, J. & Schembecker, G. Molecular interactions of alcohols with zeolite BEA and MOR frameworks. *Journal of Molecular Modeling* **19**, 5611–5624 (2013).

43. Dyer, A. & Emms, T. I. Cation exchange in high silica zeolites. *Journal of Materials Chemistry* **15**, 5012–5021 (2005).

44. Walton, K. S., Abney, M. B. & LeVan, M. D. CO2 adsorption in y and X zeolites modified by alkali metal cation exchange. *Microporous and Mesoporous Materials* **91**, 78–84 (2006).

45. Ćurković, L., Cerjan-Stefanović, Š. & Filipan, T. Metal ion exchange by natural and modified zeolites. *Water Research* **31**, 1379–1382 (1997).

46. Liu, C., Li, G., Hensen, E. J. M. & Pidko, E. A. Nature and Catalytic Role of Extraframework Aluminum in Faujasite Zeolite: A Theoretical Perspective. *ACS Catalysis* **5**, 7024–7033 (2015).

47. Brodu, N., Manero, M. H., Andriantsiferana, C., Pic, J. S. & Valdés, H. Role of Lewis acid sites of ZSM-5 zeolite on gaseous ozone abatement. *Chemical Engineering Journal* **231**, 281–286 (2013).

48. Maier, S. M., Jentys, A. & Lercher, J. A. Steaming of zeolite BEA and its effect on acidity: A comparative NMR and IR spectroscopic study. *Journal of Physical Chemistry C* **115**, 8005–8013 (2011).

49. Kanazirev, V., Price, G. L. & Dooley, K. M. Enhancement in propane aromatization with Ga2O 3/HZSM-5 catalysts. *Journal of the Chemical Society, Chemical Communications* **3**, 712–713 (1990).

50. Kanazirev, V. I. & Price, G. L. Propane conversion on Cu-MFI zeolites. *Journal of Molecular Catalysis. A, Chemical* **96**, 145–154 (1995).

51. Kwak, B. S. & Sachtler, W. M. H. Effect of Ga/Proton Balance in Ga/HZSM-5 Catalysts on C3 Conversion to Aromatics. *Journal of Catalysis* vol. 145 456–463 (1994).

52. Ono, Y. & Baba, T. Unique properties of silver cations in solid-acid catalysis by zeolites and heteropolyacids. *Physical Chemistry Chemical Physics* **17**, 15637–15654 (2015).

53. Biscardi, J. A., Meitzner, G. D. & Iglesia, E. Structure and density of active Zn species in Zn/H-ZSM5 propane aromatization catalysts. *Journal of Catalysis* **179**, 192–202 (1998).

54. Yu, S. Y., Waku, T. & Iglesia, E. Catalytic desulfurization of thiophene on H-ZSM5 using alkanes as co-reactants. *Applied Catalysis A: General* **242**, 111–121 (2003).

55. Gounder, R. & Iglesia, E. Catalytic hydrogenation of alkenes on acidic zeolites: Mechanistic connections to monomolecular alkane dehydrogenation reactions. *Journal of Catalysis* **277**, 36–45 (2011).

56. Biscardi, J. A. & Iglesia, E. Structure and function of metal cations in light alkane reactions catalyzed by modified H-ZSM5. *Catalysis Today* **31**, 207–231 (1996).

57. Yu, S. Y., Li, W. & Iglesia, E. Desulfurization of thiophene using hydrogen from alkanes on cation-modified H-ZSM5. *Abstracts of Papers of the American Chemical Society* **219**, U249–U249 (2000).

58. Ono, Y. Transformation of Lower Alkanes into Aromatic Hydrocarbons over ZSM-5 Zeolites. *Catalysis Reviews* **34**, 179–226 (1992).

59. Meriaudeau, P. & Naccache, C. The role of Ga2O3 and proton acidity on the dehydrogenating activity of Ga2O3-HZSM-5 catalysts: evidence of a bifunctional mechanism. *Journal of Molecular Catalysis* **59**, (1990).

60. Ono, Y., Osako, K., Yamawaki, M. & Nakashiro, K. Mechanism of the Activation of Butanes and Pentanes over ZSM-5 Zeolites. in *Zeolites and Microporous Crystals* (eds. Hattori, T. & Yashima, T. B. T.-S. in S. S. and C.) vol. 83 303–312 (Elsevier, 1994).

61. R.A. Sietsma, J. *et al.* Highly active cobalt-on-silica catalysts for the fischer-tropsch synthesis obtained via a novel calcination procedure. *Studies in Surface Science and Catalysis* **167**, 55–60 (2007).

62. Munnik, P., De Jongh, P. E. & De Jong, K. P. Recent Developments in the Synthesis of Supported Catalysts. *Chemical Reviews* **115**, 6687–6718 (2015).

63. Simonetti, D. A., Ahn, J. H. & Iglesia, E. Mechanistic details of acid-catalyzed reactions and their role in the selective synthesis of triptane and isobutane from dimethyl ether. *Journal of Catalysis* **277**, 173–195 (2011).

64. Lin, F. & Chin, Y. H. Mechanism of intra- and inter-molecular CC bond formation of propanal on Brønsted acid sites contained within MFI zeolites. *Journal of Catalysis* **311**, 244–256 (2014).

65. Silva, E. R., Silva, J. M., Massiani, P., Ribeiro, F. R. & Ribeiro, M. F. Effect of Cs impregnation on the properties of platinum in Pt/Na-BEA and Pt/Cs-BEA catalysts. *Catalysis Today* **107–108**, 792–799 (2005).

66. De Groot, F. High-resolution X-ray emission and X-ray absorption spectroscopy. *Chemical Reviews* **101**, 1779–1808 (2001).

67. Cho, E. J. *et al.* Auger effect in high-resolution Ce (formula presented) resonant photoemission. *Physical Review B - Condensed Matter and Materials Physics* **67**, (2003).

68. Rehr, J. J. & Ankudinov, A. L. Progress in the theory and interpretation of XANES. *Coordination Chemistry Reviews* **249**, 131–140 (2005).

69. Beauchemin, S., Hesterberg, D. & Beauchemin, M. Principal Component Analysis Approach for Modeling Sulfur K-XANES Spectra of Humic Acids. *Soil Science Society of America Journal* **66**, 83–91 (2002).

70. Newville, M. *Fundamentals of XAFS*. (2004).

71. Rehr, J. J. Theory and calculations of X-ray spectra: XAS, XES, XRS, and NRIXS. *Radiation Physics and Chemistry* **75**, 1547–1558 (2006).

72. Ravel, B. & Newville, M. *ATHENA and ARTEMIS: Interactive Graphical Data Analysis using IFEFFIT*. *Physica Scripta* vol. 115 (2005).

73. Ravel, B. & Newville, M. ATHENA, ARTEMIS, HEPHAESTUS: Data analysis for X-ray absorption spectroscopy using IFEFFIT. *Journal of Synchrotron Radiation* **12**, 537–541 (2005).

74. Newville, M. EXAFS analysis using FEFF and FEFFIT. *urn:issn:0909-0495* **8**, 96–100 (2001).

75. Sing, K. The use of nitrogen adsorption for the characterisation of porous materials. *Colloids and Surfaces A: Physicochemical and Engineering Aspects* **187–188**, 3–9 (2001).

76. Langmuir, I. The adsorption of gases on plane surfaces of glass, mica and platinum. *J Am Chem Soc* **40**, 1361–1403 (1918).

77. Brunauer, S., Emmett, P. H. & Teller, E. Adsorption of Gases in Multimolecular Layers. *J Am Chem Soc* **60**, 309–319 (1938).

78. Bae, Y. S., Yazayd'n, A. Ö. & Snurr, R. Q. Evaluation of the BET method for determining surface areas of MOFs and zeolites that contain Ultra-Micropores. *Langmuir* **26**, 5475–5483 (2010).

79. Barrett, E. P., Joyner, L. G. & Halenda, P. P. The Determination of Pore Volume and Area Distributions in Porous Substances. I. Computations from Nitrogen Isotherms. *J Am Chem Soc* **73**, 373–380 (1951).

80. Matshitse, R. Brunauer-Emmett-Teller (BET) surface area analysis. *Rhodes University, National Research Foundation* (2010).

81. Abdelrahman, O. A. *et al.* Simple quantification of zeolite acid site density by reactive gas chromatography. *Catalysis Science* 3831–3841 (2017) doi:10.1039/c7cy01068k.

82. Parry, E. P. An infrared study of pyridine adsorbed on acidic solids. Characterization of surface acidity. *Journal of Catalysis* **2**, 371–379 (1963).

83. Hughes, T. R. & White, H. M. A study of the surface structure of decationized Y zeolite by quantitative infrared spectroscopy. *Physical Chemistry* **71**, 2192–2201 (1967).

84. Barzetti, T., Selli, E., Moscotti, D. & Forni, L. Pyridine and ammonia as probes for FTIR analysis of solid acid catalysts. *Journal of the Chemical Society - Faraday Transactions* **92**, 1401–1407 (1996).

85. Gorte, R. J. Temperature-programmed desorption for the characterization of oxide catalysts. *Catalysis Today* **28**, 405–414 (1996).

86. Fărcaşiu, D., Leu, R. & Corma, A. Evaluation of accessible acid sites on solids by 15N NMR spectroscopy with Di-tert-butylpyridine as base. *Journal of Physical Chemistry B* **106**, 928–932 (2002).

87. Gold, V. & Lee, R. A. Proton transfer between 2,6-di-t-butylpyridine and its conjugate acid in an aprotic solvent. *Journal of the Chemical Society, Chemical Communications* 1032–1034 (1984) doi:10.1039/C39840001032.

88. Madon, R. J. & Boudart, M. Experimental criterion for the absence of artifacts in the measurement of rates of heterogeneous catalytic reactions. *Industrial and Engineering Chemistry Fundamentals* **21**, 438–447 (1982).

89. Arzumanov, S. S. *et al.* Propane Transformation on Zn-Modified Zeolite. Effect of the Nature of Zn Species on Alkane Aromatization and Hydrogenolysis. *Journal of Physical Chemistry C* (2019) doi:10.1021/acs.jpcc.9b09718.

90. Heemsoth, J., Tegeler, E., Roessner, F. & Hagen, A. Generation of active sites for ethane aromatization in ZSM-5 zeolites by a solid-state reaction of zinc metal with brønsted acid sites of the zeolite. *Microporous and Mesoporous Materials* **46**, 185–190 (2001).

91. Pidko, E. A. & Van Santen, R. A. Activation of light alkanes over zinc species stabilized in ZSM-5 zeolite: A comprehensive DFT study. *Journal of Physical Chemistry C* **111**, 2643–2655 (2007).

92. Xu, B., Sievers, C., Hong, S. B., Prins, R. & van Bokhoven, J. A. Catalytic activity of Brønsted acid sites in zeolites: Intrinsic activity, rate-limiting step, and influence of the local structure of the acid sites. *Journal of Catalysis* **244**, 163–168 (2006).

93. Biscardi, J. A., Meitzner, G. D. & Iglesia, E. Structure and density of active Zn species in Zn/H-ZSM5 propane aromatization catalysts. *Journal of Catalysis* **179**, 192–202 (1998).

94. Penzien, J. *et al.* Generation and Characterization of Well-Defined Zn 2 + Lewis Acid Sites in Ion Exchanged Zeolite BEA. *J. Phys. Chem. B* **108**, 4116–4126 (2004).

95. Horton, M. K., Montoya, J. H., Liu, M. & Persson, K. A. High-throughput prediction of the ground-state collinear magnetic order of inorganic materials using Density Functional Theory. *npj Computational Materials* **5**, (2019).

96. Munro, J. M., Latimer, K., Horton, M. K., Dwaraknath, S. & Persson, K. A. An improved symmetry-based approach to reciprocal space path selection in band structure calculations. *npj Computational Materials* **6**, (2020).

97. Singh, A. K. *et al.* Electrochemical Stability of Metastable Materials. *Chemistry of Materials* **29**, 10159–10167 (2017).

98. Patel, A. M., Nørskov, J. K., Persson, K. A. & Montoya, J. H. Efficient Pourbaix diagrams of many-element compounds. *Physical Chemistry Chemical Physics* **21**, 25323–25327 (2019).

99. Persson, K. A., Waldwick, B., Lazic, P. & Ceder, G. Prediction of solid-aqueous equilibria: Scheme to combine first-principles calculations of solids with experimental aqueous states. *Physical Review B - Condensed Matter and Materials Physics* **85**, (2012).

100. Zheng, H. *et al.* Grain boundary properties of elemental metals. *Acta Materialia* **186**, 40–49 (2020).

101. de Jong, M. *et al.* Charting the complete elastic properties of inorganic crystalline compounds. *Scientific Data* **2**, (2015).

102. de Jong, M., Chen, W., Geerlings, H., Asta, M. & Persson, K. A. A database to enable discovery and design of piezoelectric materials. *Scientific Data* **2**, (2015).

103. Aykol, M., Dwaraknath, S. S., Sun, W. & Persson, K. A. Thermodynamic limit for synthesis of metastable inorganic materials. *Science Advances* **4**, (2018).

104. Jain, A. *et al.* Formation enthalpies by mixing GGA and GGA + U calculations. *Physical Review B - Condensed Matter and Materials Physics* **84**, (2011).

105. Latimer, K., Dwaraknath, S., Mathew, K., Winston, D. & Persson, K. A. Evaluation of thermodynamic equations of state across chemistry and structure in the materials project. *npj Computational Materials* **4**, (2018).

106. Tran, R. *et al.* Surface energies of elemental crystals. *Scientific Data* **3**, (2016).

107. Petousis, I. *et al.* High-throughput screening of inorganic compounds for the discovery of novel dielectric and optical materials. *Scientific Data* **4**, (2017).

108. Ding, H. *et al.* Computational Approach for Epitaxial Polymorph Stabilization through Substrate Selection. *ACS Applied Materials and Interfaces* **8**, 13086–13093 (2016).

109. Jain, A. *et al.* Commentary: The materials project: A materials genome approach to accelerating materials innovation. *APL Materials* **1**, (2013).

110. Zur, A. & McGill, T. C. Lattice match: An application to heteroepitaxy. *Journal of Applied Physics* **55**, 378–386 (1984).

111. Kelly, S. D. *et al.* Comparison of EXAFS foil spectra from around the world. *Journal of Physics: Conference Series* **190**, (2009).

112. Kelly, S. D. & Ravel, B. EXAFS energy shift and structural parameters. in *AIP Conference Proceedings* vol. 882 132–134 (2007).

113. Penzien, J. *et al.* Heterogeneous catalysts for hydroamination reactions: Structure-activity relationship. *Journal of Catalysis* **221**, 302–312 (2004).

114. Barbosa, L. A. M. M., Van Santen, R. A. & Hafner, J. Stability of Zn(II) cations in chabazite studied by periodical density functional theory. *J Am Chem Soc* **123**, 4530–4540 (2001).

115. Barbosa, L. A. M. M. & Van Santen, R. A. Theoretical study of the enhanced Brønsted acidity of Zn2+-exchanged zeolites. *Catalysis Letters* **63**, 97–106 (1999).

116. Seki, T., Nakajo, T. & Onaka, M. The Tishchenko reaction: A classic and practical tool for ester synthesis. *Chemistry Letters* **35**, 824–829 (2006).

117. Hwang, A., Prieto-Centurion, D. & Bhan, A. Isotopic tracer studies of methanol-to-olefins conversion over HSAPO-34: The role of the olefins-based catalytic cycle. *Journal of Catalysis* **337**, 52–56 (2016).